Analysis and optimization of compact superdirective arrays

Alexandre Debard

To cite this version:

Alexandre Debard. Analysis and optimization of compact superdirective arrays. Optics / Photonic. Université Grenoble Alpes [2020-..], 2020. English. NNT : 2020GRALT058 . tel-03163139

HAL Id: tel-03163139
https://theses.hal.science/tel-03163139v1
Submitted on 9 Mar 2021

THÈSE

Pour obtenir le grade de

DOCTEUR DE L'UNIVERSITE GRENOBLE ALPES

Specialité : **Optique et radiofréquences**

Arrêté ministériel : 25 mai 2016

Presentée par

Alexandre DEBARD

Thèse dirigée par **Christophe DELAVEAUD, Directeur de recherche, CEA Grenoble**, et
codirigée par **Antonio CLEMENTE, Ingénieur de recherche, CEA Grenoble**

preparée au sein du **Laboratoire CEA/LETI**
dans **l'École Doctorale d'Electronique, Electrotechnique, Automatique, Traitement de Signal (EEATS)**

Analyse et optimisation d'antennes réseaux compactes superdirectives

Thèse soutenue publiquement devant le jury composé de :

M, Ala, SHARAIHA
Professeur à l'IETR, Président, Rapporteur
Mme, Anja, SKRIVERVIK
Professeur à l'EPFL, Rapporteur
M, Robert, STARAJ
Directeur du LEAT, UNCA, Examinateur
M, Fabrice, LEMOULT
Professeur à l'ESPCI, Examinateur
M, Philippe, POULIGUEN
Ingénieur de recherche à la DGA, Examinateur
M, Patrick, POTIER
Ingénieur de recherche à la DGA, Examinateur
M, Christophe, DELAVEAUD
Directeur de recherche au CEA Grenoble, Directeur de thèse
M, Antonio, CLEMENTE
Ingénieur de recherche au CEA Grenoble, Encadrant

COMMUNAUTÉ UNIVERSITÉ GRENOBLE-ALPES

Abstract

Grenoble INP
Optics and Radio-frequencies

Doctor of Philosophy

Analysis and Optimization of Compact Superdirective Antenna Arrays

by Alexandre DEBARD

The purpose of this thesis is to study and seek improvement of the superdirective antenna array technology. This technology has been recently re-examined in the literature since it can bring some interesting functionalities in the future telecommunication applications. The examination of this type of antenna is thus conducted through the use of Spherical Wave Expansion which allows for the general study of directivity limits as well as gain limits, considering lossy antennas. The classical theory of end-fire array antennas is also reviewed, in the case of uniformly spaced tapered arrays, providing theoretical evaluation of efficiency and sensitivity to source feeding precision.

Infinitesimal dipoles and Huygens sources are considered in a proposed development that links array theory and Spherical Wave Expansion. This contribution provides a formal proof for the directivity limit of Huygens-source-based end-fire arrays as well as an upper bound for the directivity of dipole-based arrays, when the inter-element spacing tends to zero. Moreover, it is shown how classical array theory can also be used to derive excitation coefficients that maximize gain rather than directivity, when loss resistances are considered. An examination over antenna size is also made to demonstrate which conditions are most favorable for the use of such supergain or superdirective end-fire array optimization.

In a second part, practical implementations of superdirective antennas are surveyed, focusing on Huygens sources and compact end-fire array designs. The chosen implementation architecture of parasitic element arrays is then detailed and studied, in order to minimize the requirement for negative or positive resistive loads. This lead to the design and measurement of five prototypes that aim at achieving the maximum possible gain or directivity for a limited radiator size, with two-, three- and four-dipole end-fire arrays.

Contents

List of Figures

List of Tables

Introduction

Electrically Small Antennas, where small is meant in the sense of the antenna electrical size compared to the operation wavelength, have been the subject of many researches from the middle of the twentieth century. Typically, Electrically Small Antennas present low radiation resistance, low efficiency, narrow bandwidth, and omnidirectional radiation behaviors. The development of innovative small or compact antennas with high performance and advanced functionalities (e.g. frequency or pattern agility, spatial selectivity, etc.) is a topic of increasing interest for the international antenna community [1]. In fact, these antenna technologies are largely required in the development of the future compact and intelligent systems for the Internet of Things (IoT), wireless sensor networks, radiofrequency identification (RFID), remote control or power transfer, and small or pico cells for the future 5th Generation (5G) mobile networks. Furthermore, the use of small antennas is a fundamental requirement to guarantee the integration of the future wireless systems operating in the frequency bands below 6 GHz in the new generation connected objects.

Electrically Small Antennas have been defined by Wheeler in [2] as antennas whose largest dimension does not exceed the ’radianlength’, equal to $\frac{2\pi}{\lambda}$, λ being the wavelength at the working frequency (cf. Figure 1). Wheeler suggested that the sphere of radius equal to the ’radianlength’, the ’radiansphere’, was the minimum sphere of influence around a small antenna. Hence, a small antenna would have an equivalent size greater than its physical size.

In any case, designing small antennas requires the study of antenna performances relatively to their size. This study started at least with the well known work of Chu,

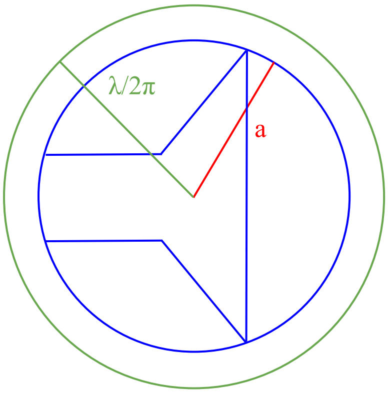

FIGURE 1: Small antenna definition according to Wheeler [2]

which showed quantitative analysis linking the size of an antenna to its quality factor. This factor is the ratio of the energy stored near the antenna to the energy which the antenna radiates. A high quality factor generally comes with a narrow working bandwidth. This analysis is based on the expression of the antenna radiation pattern as a sum of Spherical Waves. Moreover, it was also shown that the capacity of the antenna to focus its radiation beam in a certain direction was also limited by its size. Classically, a narrow beamwidth would then require a sufficiently large size antenna, as demonstrated by Harrington in [3], also using Spherical Wave Expansion theory. A 'superdirective' antenna would then refer to an antenna whose directivity would exceed the 'normal limit' presented in [3]. This limit would then be the maximum directivity that an antenna could 'normally' be able to reach for a given size. This limit is extracted from the study of the evolution of the power spherical waves over propagation distance and several other limits were proposed in the litterature as it is presented in Chapter 2. More generally, it is acknowledged that there is always some trade-off that needs to be made between directivity and quality factor for a given radiator size [4], [5]. The modification of one feature always has an impact on the others.

The design of small directive antenna can then be done with the use of these theoretical analysis. Indeed, the limits presented in the literature provide guidelines for the spherical modes that need to be excited for reaching a given directivity and the quality factor that can then be expected for a given antenna size, for example. The theory of small directive antennas can also be found in the array antenna theory. Hence, it was proven that linear array antennas of independently excited elements can have increasingly narrow beamwidth as the inter-element spacing tends to zero. According to [6], the problem was first considered by Shelkunoff [7] who found current distribution that would yield high directivities, but he did not provide the upper directivity limit. Then, the problem of finding the current distribution that generates a given beamwidth and sidelobe level was solved by Dolph using Tchebycheff polynomials [8]. Uzkov [9] was the first researcher which determined the excitation coefficients that maximize the theoretical directivity of a linear array of isotropic radiators, considering the case where the distance between array elements tends to zero. The maximum directivity was proven to be P^2 for an array of P isotropic radiators. This type of array was however considered impractical for a long time as it was shown in [10] that the precision requirements on the excitation coefficients were extremely high, for the example of an array of nine radiators spaced of $\frac{\lambda}{4}$. The continued study of the problem would then find the precision requirements on excitation coefficients as well as the resulting diminution of radiation efficiency, with the works of [11], [12], [6] and [13].

Several different prototypes of small superdirective arrays were presented in the recent literature, such as [14]–[25]. These prototypes use several different single element designs for up to four-element arrays and a maximum directivity of 12 dBi measured in [22] and maximum gain of 8 dBi measured in [23], both using end-fire arrays of four electrical dipoles. The possibility of a small supergain antenna was demonstrated in [15] with a two-small-dipole array that reach a gain of 7 dBi and a total size defined by $a = \frac{\lambda}{2\pi}$ (with a defined in Figure 1).

The feasibility of antennas that exceed this state of the art was however not determined yet. Furthermore, it was shown that using Huygens sources (or magneto-electric dipoles) as single element would theoretically increase the gain of the arrays [26], [27]. Although Huygens sources designs have been experimentally demonstrated in the literature, [28]–[30], their use in an array was considered impractical compared to the use of simple dipoles, since [31]. An attempt to provide more quantitative performance limits for small superdirective and supergain arrays is made in this work. Then, a design method is proposed, especially for the maximization of gain over directivity, which takes into account the antenna loss resistances.

This thesis is then organized in two parts. The first part is dedicated to the review of the theoretical background and divided into three chapters. The first chapter provides the definition of Spherical Wave Functions, introducing the tools and denotations that are used in the rest of the report. The second chapter is a survey of the fundamental literature studies of the directivity limits through the examination of the Spherical Wave Functions in the first section and through superdirective array theory in the second section. In the third chapter, a contribution to those studies is then proposed by establishing links between the two approaches. This study then provides an analytic proof of the maximum directivity that can be reached by dipole-based and Huygens-source-based end-fire arrays when the inter-element spacing tends to zero. Also, the gain limitations taking into account the loss resistances are also reviewed in this chapter, again comparing both theoretical approaches and adding original results achieved by full-wave electromagnetic simulations of dipole-based arrays.

The second part of this thesis deals with the practical realization of small directive antennas and is also divided into three chapters. The fourth chapter is a survey of the state of the art of superdirective and supergain antennas. It reviews linear end-fire arrays as well as practical designs of Huygens sources and Huygens-source based arrays. A more detailed introduction of parasitic element arrays is then made as it is the technology considered in this work. Ways to optimize the design of the unitary elements of supergain arrays are also presented. The fifth chapter is a contribution to the analysis of the calculation of parasitic loads for the design of superdirective or supergain arrays. This is done with the use of an analytic model for the mutual impedance of two parallel electric dipoles. Hence, the optimal load impedance can be theoretically computed as a function of inter-element spacing for dipole-based arrays. The purpose is to determine how to design the array in order to avoid the requirement of high or negative resistive loads. Finally, the last chapter demonstrates the proposed designs and the measurements of their performances. Several arrays of up to four dipoles were realized. Measurements are made with small bent dipoles and halfwave dipoles. Furthermore, the design of a two-Huygens-source array is proposed with the simulation of its performances. Finally, general conclusions are drawn leading to the discussions on future possible works on small directive antennas.

PART I: Theoretical Background and Analysis

Chapter 1

Spherical Wave Expansion and Basic Radiation Sources

In this chapter, Spherical Wave Expansion (SWE) theory is introduced as it is one of the main computational tools used for the studies made in this work. These functions form a base of solutions for the Helmholtz wave propagation equation, in a free-of-charge space. In particular, any electromagnetic field can be represented as a linear combination of Spherical Wave Functions. The definition of antenna directivity as well as radiated power is also given. Moreover, methods to expand a given radiation pattern in a sum of Spherical Wave are also presented leading to the introduction of the infinitesimal radiation sources, that are the electric and magnetic dipoles as well as the Huygens source which is a specific combination of both sources. The SWE is then applied to the field radiated by these sources. The most fundamental theory is taken from [32], but the works of [33] and [34] were largely used in this thesis. These more recent works were made mainly for the use of near field antenna measurement. Indeed, it is possible to derive the Spherical Waves radiated by an antenna from measurements of its near-field and to deduce the far-field radiation pattern of the antenna from it. In this work, the study of SWE will be used for the analysis of antenna design for directivity maximization.

1.1 Spherical Wave Function

In a free-of-charge region, the radiated electric field ($\vec{E}$) and magnetic field ($\vec{H}$) are bound by the Helmholtz equation which can be written as

$$\vec{\nabla} \times \vec{\nabla} \times \vec{C} - k^2\vec{C} = 0 \tag{1.1}$$

where $\vec{C}$ is the unknown vector field, $k = \frac{2\pi}{\lambda}$, and λ is the wavelength, considering the fields with a time dependence of $e^{-j\omega t}$ where $\omega = 2\pi f$, with f the frequency of the wave. $\vec{\nabla}$ designates the gradient function and $\times$ is the vector product. The corresponding scalar equation is

$$(\nabla^2 + k^2)\psi = 0 \tag{1.2}$$

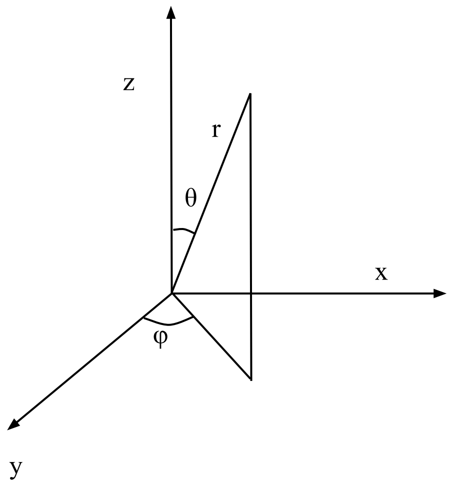

FIGURE 1.1: Spherical coordinate system.

Solutions to (1.1) can be calculated from (1.2) [34]:

$$\vec{l} = \vec{\nabla}\psi \tag{1.3}$$

$$\vec{m} = \vec{\nabla}\psi \times \vec{r} \tag{1.4}$$

$$\vec{n} = k^{-1}\vec{\nabla} \times \vec{m} \tag{1.5}$$

$\vec{m}$ and $\vec{n}$ always have a divergence equal to zero like the electric and magnetic field in a free-of-charge region. These vectors are then chosen for $\vec{E}$ and $\vec{H}$. Solutions to (1.2) in spherical coordinates (r, θ, ϕ) (cf. Figure 1.1) are proportional to [32]:

$$f_{mn}^{(c)} = \frac{1}{\sqrt{2\pi}} \frac{1}{\sqrt{n(n+1)}} \left(-\frac{m}{|m|}\right)^m z_n^{(c)}(kr) \overline{P}_n^{|1|} e^{jm\phi} \tag{1.6}$$

This form is taken from [34], providing normalized power to $\frac{1}{2}$ for each Spherical Waves as it will be seen in section 1.2. The radial dependant amplitude is a spherical Bessel or Hankel function $z_n^{(c)}(kr)$ characterized by the order n. The type of function to use is defined by the (c) exponent which can be 1, 2, 3 or 4 and depends on the specification of the considered space and the propagation direction of the wave, whether it is inward or outward the center of the coordinate system. They are defined as follows

$$z_n^{(1)}(kr) = j_n(kr) \tag{1.7}$$

$$z_n^{(2)}(kr) = n_n(kr) \tag{1.8}$$

$$z_n^{(3)}(kr) = h_n^{(1)}(kr) = j_n(kr) + jn_n(kr)) \tag{1.9}$$

$$z_n^{(4)}(kr) = h_n^{(2)}(kr) = j_n(kr) - jn_n(kr) \tag{1.10}$$

where $j_n(kr)$ and $n_n(kr)$ are the spherical Bessel and Neumann functions respectively, and $h_n^{(1)}(kr)$, $h_n^{(2)}(kr)$ are the spherical Hankel functions of the first and second kind, respectively. The cases $c = 1$ and $c = 2$ are used to describe standing waves and $c = 3$, $c = 4$ are for outward ($+\vec{r}$ direction), respectively inward travelling ($-\vec{r}$ direction) wave [34]. In the case where the work region is the one outside the sphere that encloses the sources and considering outgoing waves, the Hankel function of the first kind is used ($z_n^{(c=3)}(kr) = h_n^{(2)}(kr)$).

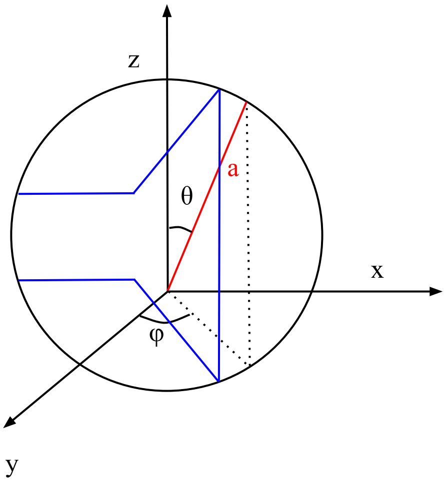

FIGURE 1.2: Minimum radius sphere circumscribing the radiating device and delimiting the work region outside from it.

The oscillations of the wave on the elevation (θ) angle are described by derivations of the associated Legendre function defined as

$$\overline{P}_n^m(cos\theta) = (sin\theta)^m \frac{d^m \overline{P}_n^{|m|}(cos\theta)}{d(cos\theta)^m} \tag{1.11}$$

where P_n is the Legendre polynomial of order n and denoting

$$\overline{P}_n = \sqrt{\frac{2n+1}{2}\frac{(n-m)!}{(n+m)!}} P_n. \tag{1.12}$$

Then, the index m only describes azimutal (ϕ) oscillation with the exponential term $e^{jm\phi}$. This relative integer is included in the interval $[-n, n]$.

Taking these f_{mn} functions as the ψ function in (1.3), the vector wave functions, from $\vec{m}$ and $\vec{n}$ can be expressed as [34]:

$$\vec{F}^{(c)}_{1mn} = \frac{1}{\sqrt{2\pi}}\frac{1}{\sqrt{n(n+1)}}e^{jm\phi}\{z^{(c)}_n(kr)\frac{jm\overline{P}^{|m|}_n(cos\theta)}{sin\theta}\vec{e}_\theta - z^{(c)}_n(kr)\frac{d\overline{P}^{|1|}_n(cos\theta)}{d\theta}\vec{e}_\phi\} \quad (1.13)$$

$$\vec{F}^{(c)}_{2mn} = \frac{1}{\sqrt{2\pi}}\frac{1}{\sqrt{n(n+1)}}e^{jm\phi}\{\frac{n(n+1)}{kr}z^{(c)}_n(kr)\overline{P}^{|m|}_n e^{jm\phi}\vec{e}_r +$$
$$\frac{1}{kr}\frac{d}{d(kr)}\{krz^{(c)}_n(kr)\}\frac{d\overline{P}^{|m|}_n(cos\theta)}{d\theta}\vec{e}_\theta + \frac{1}{kr}\frac{d}{d(kr)}\{krz^{(c)}_n(kr)\}\frac{jm\overline{P}^{|m|}_n(cos\theta)}{sin\theta}\vec{e}_\phi\} \quad (1.14)$$

The two forms provided with the indice $s = 1$ and $s = 2$ describe a Tranverse Electric (TE) wave and a Transverse Magnetic (TM) wave, respectively.

Thus, any radiated electrical field in a free-of-charge region can be expressed in spherical coordinates as [34]:

$$\vec{E}(r,\theta,\phi) = \sqrt{\eta}k\sum_{s=1}^{2}\sum_{n=1}^{N}\sum_{m=-n}^{n} T_{smn}\vec{F}^{(4)}_{smn}(r,\theta,\phi) \quad (1.15)$$
$$= \sqrt{\eta}k\sum_{smn} T_{smn}\vec{F}^{(4)}_{smn}(r,\theta,\phi) \quad (1.16)$$

and the magnetic field is

$$\vec{H}(r,\theta,\phi) = \frac{-jk}{\sqrt{\eta}}\sum_{smn} T_{smn}\vec{F}^{(4)}_{(s+1),m,n}(r,\theta,\phi) \quad (1.17)$$

where η is the specific impedance of the medium assumed complex, T_{smn} are the complex Spherical Wave Coefficients.

These wave functions can also be calculated using the far-field approximation, taking that the observation radius r tends to infinity. The far-field pattern function $\vec{K}_{smn}(\theta,\phi)$ is then defined in [34] by the equation:

$$\vec{K}_{smn}(\theta,\phi) = \lim_{kr\to\infty}[\sqrt{4\pi}\frac{kr}{e^{-ikr}}\vec{F}^{(4)}_{smn}(r,\theta,\phi)] \quad (1.18)$$

This gives

$$\vec{K}_{1mn} = \sqrt{\frac{2}{n(n+1)}}(-\frac{m}{|m|})^m(-j)^{n+1}e^{jm\phi}\{\frac{jm\overline{P}^{|1|}_n(cos\theta)}{sin\theta}\vec{e}_\theta - \frac{d\overline{P}^{|1|}_n(cos\theta)}{d\theta}\vec{e}_\phi\} \quad (1.19)$$

$$\vec{K}_{2mn} = \sqrt{\frac{2}{n(n+1)}}(-\frac{m}{|m|})^m(-j)^{n}e^{jm\phi}\{\frac{d\overline{P}^{|1|}_n(cos\theta)}{d\theta}\vec{e}_\theta + \frac{jm\overline{P}^{|1|}_n(cos\theta)}{sin\theta}\vec{e}_\phi\} \quad (1.20)$$

The electrical far-field then becomes

$$\vec{E}(r,\theta,\phi) = \frac{\sqrt{\eta}k}{\sqrt{4\pi}}\frac{e^{jkr}}{kr}\sum_{smn} T_{smn}\vec{K}_{smn}(\theta,\phi) \tag{1.21}$$

The Spherical Wave Expansion is then the calculation of the T_{smn} coefficients from a simulated or measured radiated field. The method used in the analysis of this work is detailed in section 1.3.

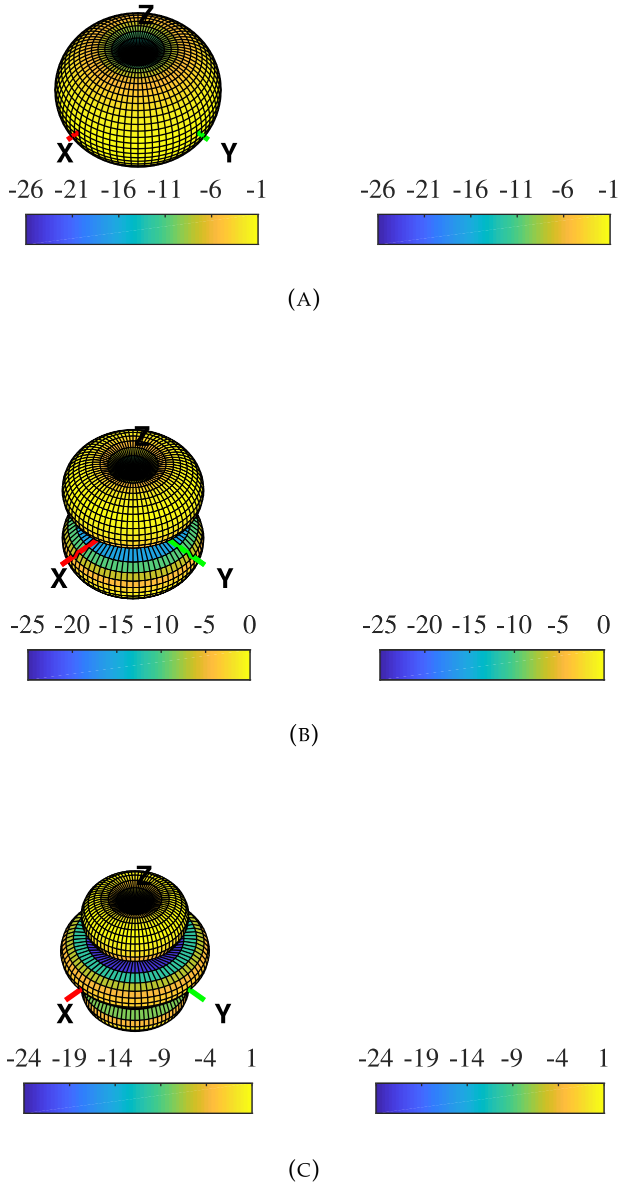

FIGURE 1.3: 3D plot of the power of far-field pattern functions, $|\vec{K}_{20n} \cdot \vec{e}_\theta|^2$ on the left side and $|\vec{K}_{20n} \cdot \vec{e}_\phi|^2$ on the right side. The wave orders considered are $n = 1$ (A), $n = 2$ (B) and $n = 3$ (C).

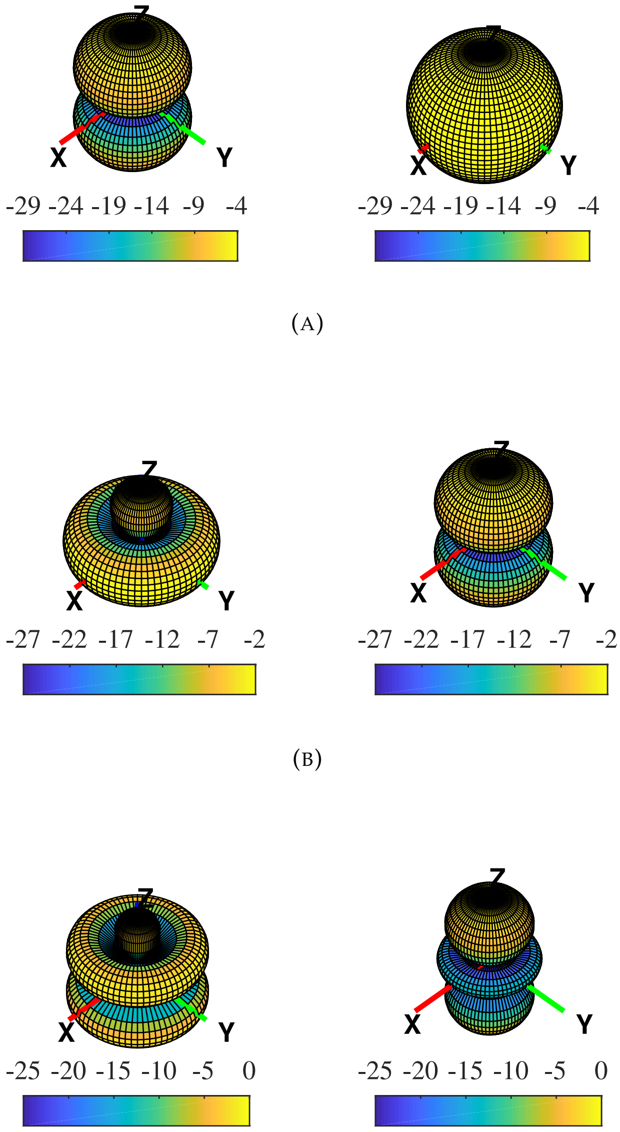

(A)

(B)

(C)

FIGURE 1.4: 3D plot of the power of far-field pattern functions, $|\vec{K}_{21n} \cdot \vec{e}_\theta|^2$ on the left side and $|\vec{K}_{21n} \cdot \vec{e}_\phi|^2$ on the right side. The wave orders considered are $n = 1$ (A), $n = 2$ (B) and $n = 3$ (C).

To illustrate the SWE, some far-field pattern functions were plotted in 3D in Figure 1.3, for $m = 0$ and Figure 1.4 for $m = 1$, for the orders $n = 1$, $n = 2$ and $n = 3$. Only functions with $s = 2$ are displayed, as the $s = 1$ pattern is simply derived by swapping $\vec{e}_\theta$ and $\vec{e}_\phi$ components. Also, patterns for $m = -1$ are identical to the ones for $m = 1$ as only the phase is changed.

1.2 Radiated power and directivity

The directivity $D(\theta,\phi)$ is defined for the far-field of an antenna as the ratio between the power radiated per solid angle in the direction (θ,ϕ) and the power radiated per unit solid angle if the antenna radiated isotropically [34]. This can be written

$$D(\theta,\phi) = \frac{4\pi r^2 Re(\langle \vec{E} \times \vec{H}^* \rangle . \vec{e}_r)}{P_{rad}} \tag{1.22}$$

where $\langle \vec{E} \times \vec{H}^* \rangle$ is the time-averaged Poynting vector. In the far-field case where the radiated waves are plane, it simplifies as

$$D(\theta,\phi) = \frac{4\pi r^2 |\vec{E}(\theta,\phi)|^2}{2\eta P_{rad}} \tag{1.23}$$

From (1.21), the radiation intensity in the (θ,ϕ) direction is

$$\frac{r^2|\vec{E}(\theta,\phi)|^2}{2\eta} = \frac{1}{2}\frac{1}{4\pi}|\sum_{smn} T_{smn}\vec{K}_{smn}(\theta,\phi)|^2 \tag{1.24}$$

The radiated power is calculated by integrating the radiation intensity over a sphere of radius r and centered in the coordinate system. This radiated power is equal to

$$\begin{aligned} P_{rad} &= \int_0^{2\pi}\int_0^{\pi} \frac{r^2|\vec{E}(\theta,\phi)|^2}{2\eta} sin\theta d\theta d\phi \\ &= \frac{1}{2}\frac{1}{4\pi}\int_0^{2\pi}\int_0^{\pi} |\sum_{smn} T_{smn}\vec{K}_{smn}(\theta,\phi)|^2 sin\theta d\theta d\phi \\ P_{rad} &= \frac{1}{2}\sum_{smn}|T_{smn}|^2 \end{aligned} \tag{1.25}$$

as the $\vec{K}_{smn}$ form an orthonormal set of functions [34].

The directivity can then be calculated from the radiated modes as

$$D(\theta,\phi) = \frac{|\sum_{smn} T_{smn}\vec{K}_{smn}(\theta,\phi)|^2}{\sum_{smn}|T_{smn}|^2} \tag{1.26}$$

1.3 Spherical Wave Expansion

Deriving the T_{smn} coefficients defining the SWE of a given radiated field can be made through several methods [33], [34]. The main purposes of the methods presented in [33] are to calculate the SWE of a field from near field measurements, in order to derive the far-field pattern. The method selected in [33] is a matrix method. This method detailed in [33] is based on solving a matrix system of the form $\mathbf{KT} = \mathbf{E}$, where $\mathbf{K}$ is the matrix containing the $\vec{K}_{smn}$ functions, $\mathbf{T}$ is the column vector of T_{smn}

coefficients to find and E is a vector filled with measurements of the radiated electric field. Other methods are based on the orhogonality of the Spherical Wave Functions and thus require the integration of the field on the surface of a sphere. The advantages of using this matrix method are that the measurement points do not have to be placed on the same sphere (which is not a problem for the far-field case considered in this work anyway) and that the quality of the SWE can be predicted through the calculation of the conditioning of matrix $\mathbf{K}$ [33]. In order to determine the Spherical Wave Coefficients necessary to match a given radiated field, this field must be known for several angular points and for the two orthogonal polarizations to generate enough equations like (1.21). This allows to create an over-determined system to optimize with a least mean square method, [33], [34]. The system if in the form $\mathbf{KT} = \mathbf{E}$, with :

$$\mathbf{K} = \begin{bmatrix} K^{\theta}_{1,-1,1}(\theta_1,\phi_1) & K^{\theta}_{2,-1,1}(\theta_1,\phi_1) & K^{\theta}_{1,0,1}(\theta_1,\phi_1) & \cdots \\ K^{\phi}_{1,-1,1}(\theta_1,\phi_1) & K^{\phi}_{2,-1,1}(\theta_1,\phi_1) & K^{\phi}_{1,0,1}(\theta_1,\phi_1) & \cdots \\ K^{\theta}_{1,-1,1}(\theta_2,\phi_2) & K^{\theta}_{2,-1,1}(\theta_2,\phi_2) & K^{\theta}_{1,0,1}(\theta_2,\phi_2) & \cdots \\ K^{\phi}_{1,-1,1}(\theta_2,\phi_2) & K^{\phi}_{2,-1,1}(\theta_2,\phi_2) & K^{\phi}_{1,0,1}(\theta_2,\phi_2) & \cdots \\ \cdots & \cdots & \cdots & \cdots \end{bmatrix}, \tag{1.27}$$

$$\mathbf{T} = \begin{bmatrix} T_{1,-1,1} \\ T_{2,-1,1} \\ T_{1,0,1} \\ \vdots \end{bmatrix} \tag{1.28}$$

and

$$\mathbf{E} = \begin{bmatrix} E^{\theta}(\theta_2,\phi_2) \\ E^{\theta}(\theta_2,\phi_2) \\ E^{\phi}(\theta_2,\phi_2) \\ E^{\phi}(\theta_2,\phi_2) \\ \vdots \end{bmatrix} \tag{1.29}$$

where $K^{\theta}(\theta,\phi)$, $K^{\phi}(\theta,\phi)$, respectively $E^{\theta}(\theta,\phi)$, $E^{\phi}(\theta,\phi)$ are the projections of the vector $\vec{K}$, respectively $\vec{E}$, are the projections of the vector $\vec{V}$ on the $\vec{e}_{\theta}$ and $\vec{e}_{\phi}$ component, respectively. The $\mathbf{K}$ matrix was constructed in [33] so that all row are linearly independent from the other, using the orthogonality of the Spherical Wave Functions. The T_{smn} coefficients are then given by the optimal solution

$$\mathbf{T} = \mathbf{K}^{\dagger}\mathbf{E} \tag{1.30}$$

where $\mathbf{K}^{\dagger}$ is the pseudo-inverse of $\mathbf{K}$. The length of the $\mathbf{T}$ vector is equal to the number of modes which is calculated as $N_{modes} = \sum_{s=1}^{2}\sum_{n=1}^{N}\sum_{m=-m}^{n} 1 = 2N(N+2)$. The proper maximum order N then has to be determined as the sufficient number that recreate more than 99% of the power of the given radiated field [34]. In our case, the comparison of power is made between the one calculated from (1.25) and the measured or simulated power. The truncation number N can be calculated from the variation study of the radial dependant part $z_n(kr)$ of the Spherical Wave Functions defined in (1.13) and (1.14). As it is developed in Chapter 2, this number is linked to the radius r of the minimum sphere circumscribing the antenna, denoted a in the rest of the report, as $N = ka + n_1$ where n_1 is an offset integer that is variable according to the required precision of the expansion, [33], [34]. An illustration of the SWE is made in section 1.4 as the radiation patterns of infinitesimal dipoles are analyzed.

1.4 Infinitesimal radiation sources

Infinitesimal raditors are presented in this section through the Spherical Wave they radiate. The SWE of an electric and magnetic dipole are demonstrated as well as the SWE of a Huygens source. The effect of antenna translation and rotation in the coordinate system is also shown as it will be used in the study of antenna arrays in the latter chapters.

1.4.1 Electrical and magnetic dipole

The most basic radiation source is the electric or magnetic dipole. It can be defined as an infinitesimal linear electric or magnetic current. The radiated electric field, in the far-field region, of an electric dipole of length l along the z axis is written [35]

$$\vec{E}(r,\theta) = j\eta \frac{kI_0 l sin\theta}{4\pi r} e^{-jkr} \vec{e}_\theta \tag{1.31}$$

where I_0 is the electric current running through it. Let its far-field pattern be then defined as

$$\vec{f}_{de}(\theta,\phi) = sin\theta \vec{e}_\theta \tag{1.32}$$

This can be expanded in a single TM spherical mode

$$\vec{f}_{de}^{z} = \frac{1}{\sqrt{3}} \vec{K}_{201} \tag{1.33}$$

(A) (B)

FIGURE 1.5: Diagram representation of infinitesimal electric (A) and magnetic (B) dipoles oriented on the z axis.

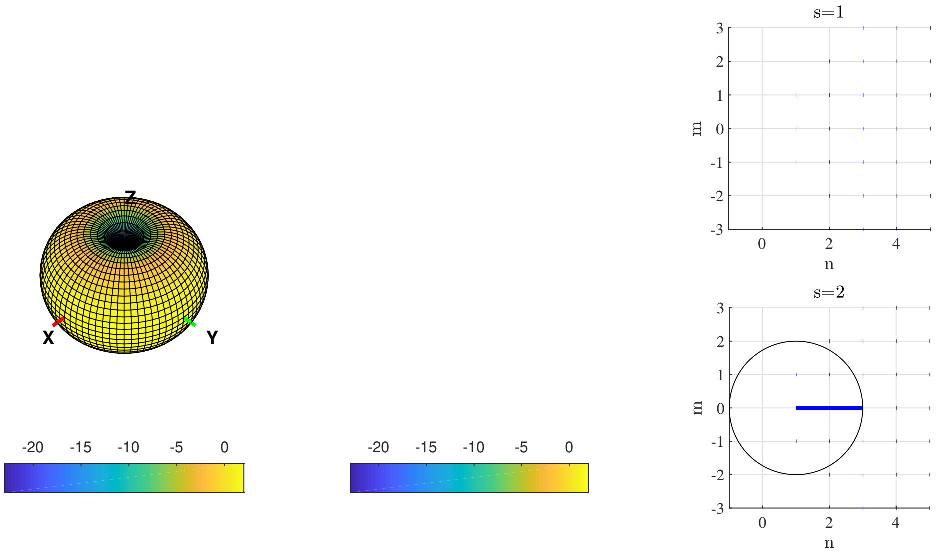

(A) (B)

FIGURE 1.6: Radiation pattern (A) and SWE (B) of a z oriented dipole. The scale of the radiation pattern diagram is in decibels, the right diagram is the θ component and the left diagram is the ϕ component. In the SWE diagram (B), the value of the radius of the circles is proportional to the square of the magnitude of the corresponding coefficient and the orientation of the displayed radius represents their phases.

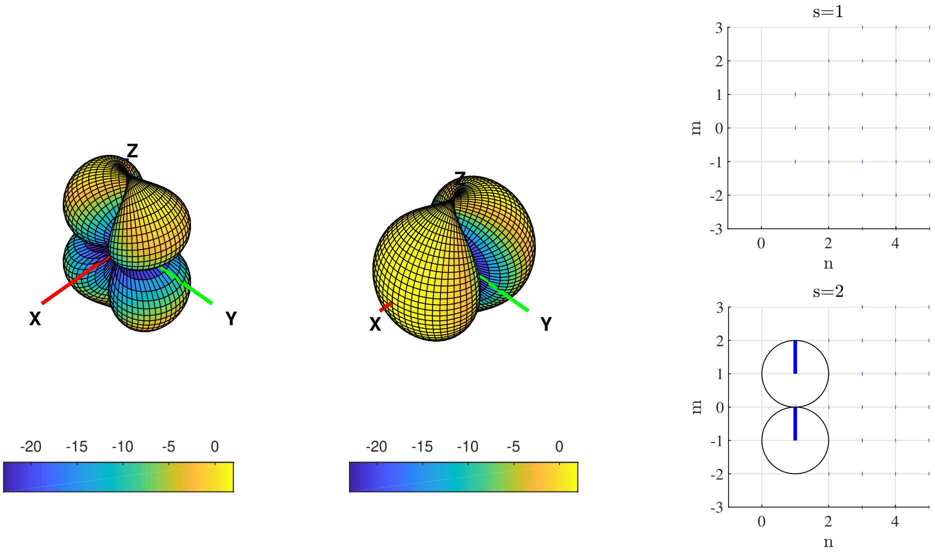

(A) (B)

FIGURE 1.7: Radiation pattern (A) and SWE (B) of a y oriented dipole. The scale of the radiation pattern diagram is in decibels, the right diagram is the θ component and the left diagram is the ϕ component.

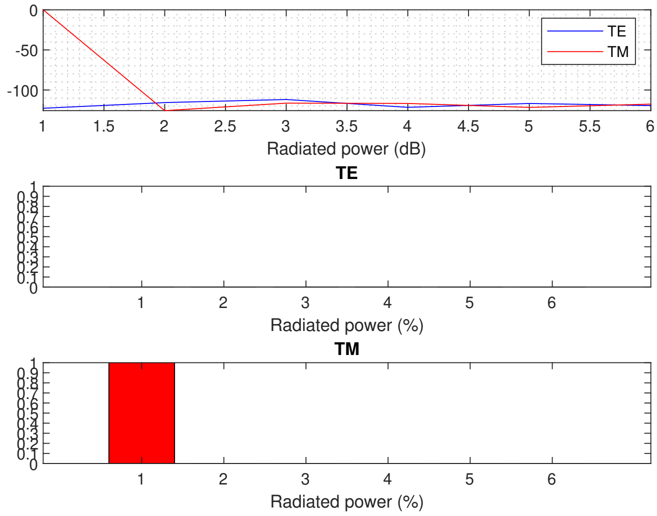

FIGURE 1.8: Power distribution on TE and TM modes of an electric dipole centered in the coordinate system.

The magnetic dipole is the dual source of the electric one, hence, its far-field pattern can be derived from the pattern of the electric dipole with the formulas

$$\vec{f}_{dm} \cdot \vec{e}_\theta = \vec{f}_{de} \cdot \vec{e}_\phi \tag{1.34}$$
$$\vec{f}_{dm} \cdot \vec{e}_\phi = -\vec{f}_{de} \cdot \vec{e}_\theta$$

Also, its SWE is found by taking the SWE of the electric dipole and swapping the $s = 1$ and $s = 2$ indices. The far-field pattern and Spherical Wave Expansion of a magnetic dipole oriented on the z axis is then

$$\vec{f}^z_{dm} = sin\theta\vec{e}_\phi \tag{1.35}$$
$$= \frac{1}{\sqrt{3}}\vec{K}_{101} \tag{1.36}$$

The SWE of an electric and magnetic dipole are then given by $T_{201} = \beta$ and $T_{101} = \beta$, respectively, all other coefficients being zero and β is a complex number that can be chosen for power normalization. However, due to the use of spherical coordinates, this SWE is particular to the z axis orientation of the dipoles. Indeed, the far-field pattern of an electric dipole oriented on the y axis is

$$\vec{f}^y_{ed} = cos\theta sin\phi\vec{e}_\theta + cos\phi\vec{e}_\phi \tag{1.37}$$

which can then be expanded to

$$\vec{f}^y_{ed} = \frac{1}{\sqrt{3}}(\vec{K}_{2-11} + \vec{K}_{211}) \tag{1.38}$$

The SWE is then made of two modes, $T_{2,-1,1} = \beta$ and $T_{211} = \beta$. Moreover, performing a translation of the dipole from the center of the coordinate system also influences its SWE. The SWE of the dipoles is displayed in Figures 1.6 and 1.7 for the orientations on the z and y axis, respectively. The power distribution on TE and TM modes is shown in Figure 1.8 and is independent to dipole orientation. The total power radiated is normalized to $P_{rad} = 2$ in the SWE representation of the diagrams of Figures 1.6 and 1.7 (B). This value is chosen for a clearer visibility in all diagrams. The radiation pattern display the values of directivity. The maximum directivity of a dipole is 1.5. Note that in any case of positioning, the SWE of a magnetic dipole is obtained by taking the one of an electric dipole in the same position and swapping TE($s = 1$) and TM($s = 2$) modes.

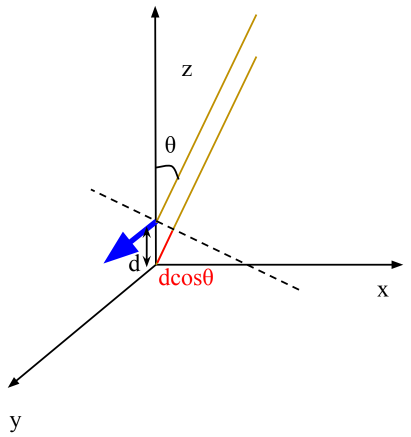

FIGURE 1.9: Path difference of rays arriving on two aligned positions along the z axis.

Indeed, according to the translation theorem ([13]), in the far-field approximation, translating a source along a vector $\vec{v}$ multiplies its radiated field by $e^{jk\vec{e}_r\cdot\vec{v}}$. This term creates a phase shift that is dependent on the observation direction $\vec{e}_r$. A diagram representing the case of a translation along the z axis is in Figure 1.9. This phase shift is seen in the SWE with the addition of an infinite series of modes, even though the radiation pattern's shape remains unchanged. This series comes from the series development of the exponential $e^{jk\vec{e}_r\cdot\vec{v}} = \sum_{n=0}^{\infty} \frac{[k\vec{e}_r\cdot\vec{v}]^n}{n!}$. The effect of translation on the SWE of an electric dipole oriented on the z axis is shown in Figure 1.10 .

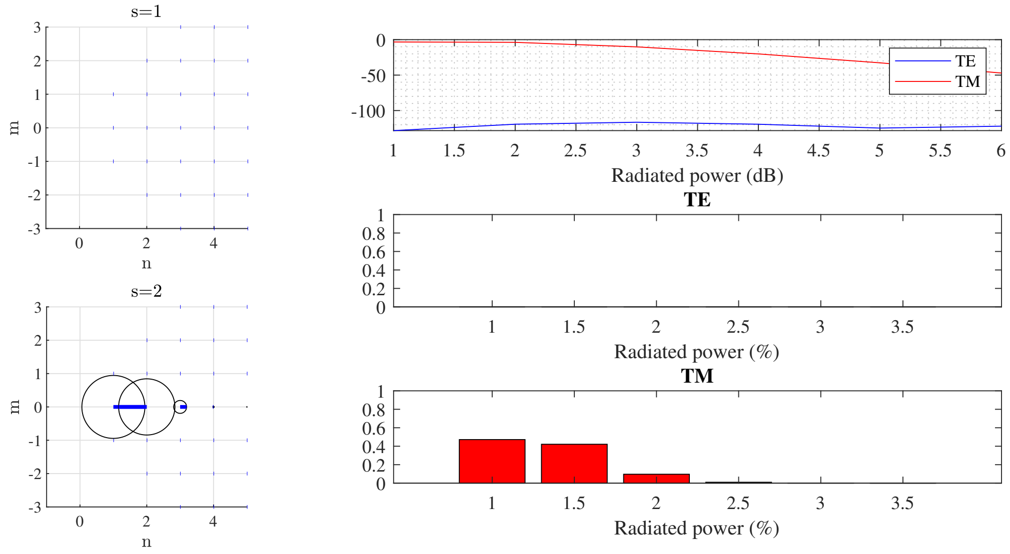

(A) (B)

FIGURE 1.10: SWE (A) and power distribution on TE and TM modes of an electric dipole polarized along the z axis and translated of 0.3λ along the z axis.

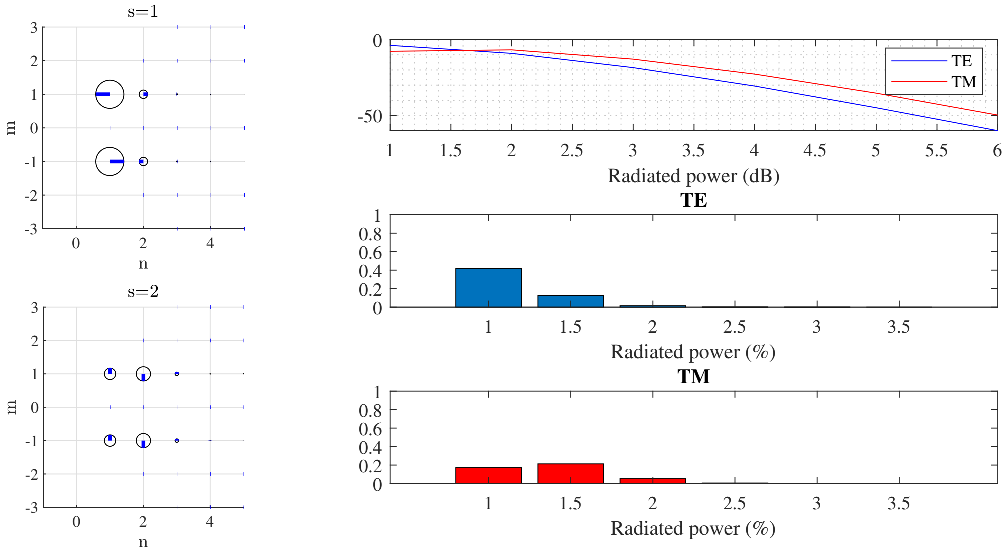

(A) (B)

FIGURE 1.11: SWE (A) and power distribution on TE and TM modes of an electric dipole polarized along the y axis and translated of 0.3λ along the z axis.

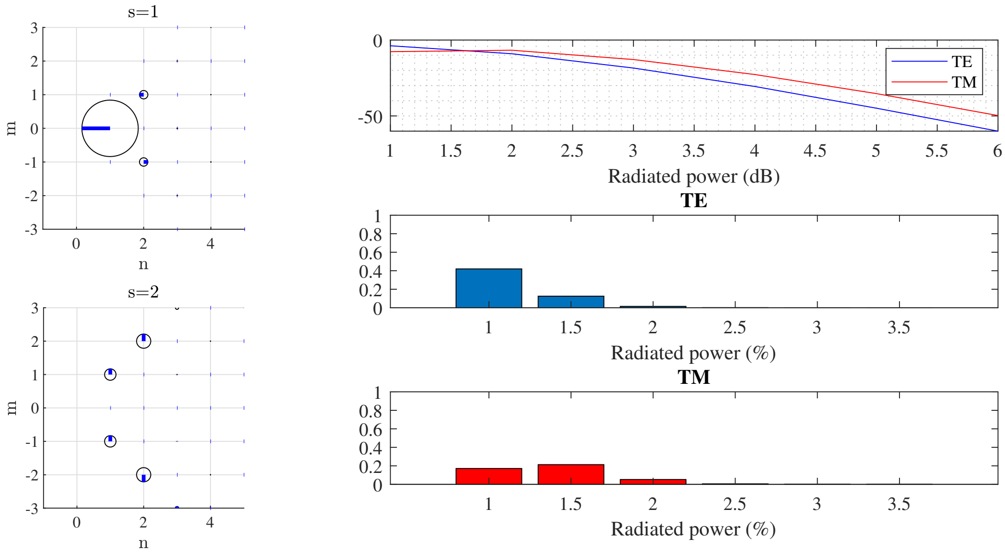

(A) (B)

FIGURE 1.12: SWE of an electric dipole polarized along the y axis and translated of 0.3λ along x axis.

Attention is drawn to the fact that when the translation is along the z axis, only modes of same index m and higher order n are created. This is due to the fact that $\vec{e}_r \cdot \vec{v} = \vec{e}_r \cdot dcos\theta\vec{e}_z$ so that the phase shifting never depends on the ϕ coordinate, which is governed by the index m. A translation in any other direction creates a phase shift that depend on the ϕ angle and then generates modes of different index m. The power distribution on the TE and TM modes is shown on Figure 1.10 for a z oriented electric dipole translated on the z axis and Figure 1.12 for a y oriented electric dipole translated on the x axis. In the case of an orientation on the y or x axis, the translation of an electric or magnetic dipole generates both TE and TM modes, as the dipole far-field pattern is splitted on both the $\vec{e}_\theta$ and $\vec{e}_\phi$ components. Hence, the choice of a proper coordinate system is required to perform a radiation analysis with SWE.

Any kind of other source can then be described as a combination of dipoles properly distributed in space. One simple and canonical combination is the Huygens source, detailed in the next subsection.

1.4.2 Huygens source

A Huygens source is made of an electric and magnetic dipole with orthogonal orientation and identical center positioning and excitation coefficients. As seen with the dipoles, its SWE depends on orientation and position in the coordinate system. Its polarization is given by the orientation of its electric dipole. The example of a Huygens source polarized on the y axis and radiating in the $+\vec{z}$ direction is represented on Figure 1.13. Considering that the $\vec{J}$ vector represents the electric current running through the electric dipole and $\vec{M}$ is the magnetic current of the magnetic dipole, the right balance between the two sources is

$$\eta|\vec{J}| = -|\vec{M}| \tag{1.39}$$

This sign difference makes the maximum radiation in the $\theta_0 = 0$ direction instead of $\theta_0 = pi$.

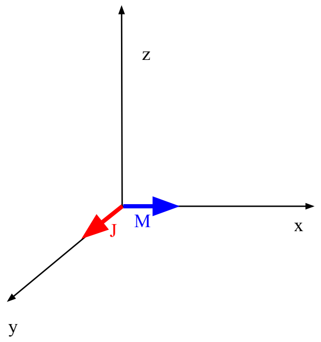

FIGURE 1.13: Huygens source representation diagram. The $\vec{J}$ vector represents the electric current running through the electric dipole and $\vec{M}$ is the magnetic current of the magnetic dipole.

The radiation pattern of this source is displayed in Figure 1.14 for the z polarization and Figure 1.15 for the y polarization.

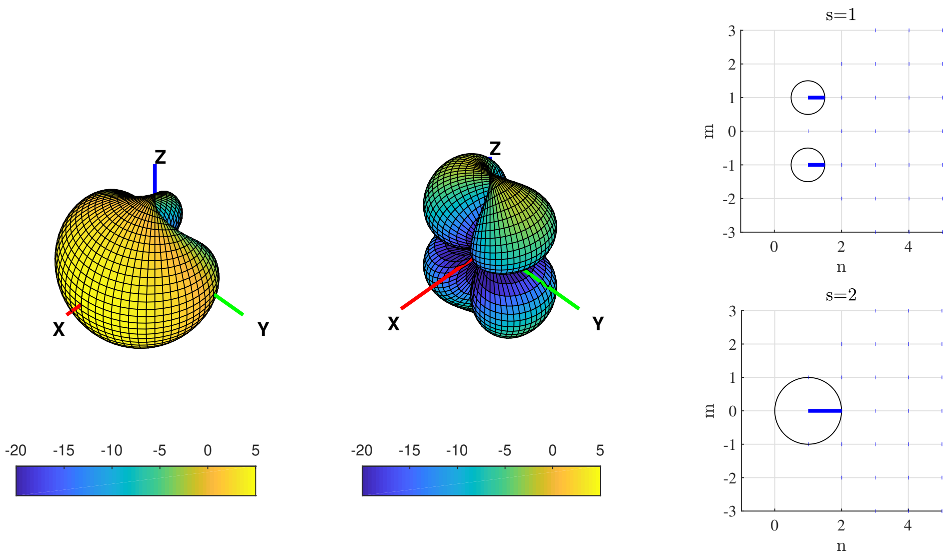

(A) (B)

FIGURE 1.14: Radiation pattern (A) and SWE (B) of a Huygens source polarized along the z axis. The scale of the radiation pattern is in decibels, the right diagram is the θ component and the left diagram is the ϕ component.

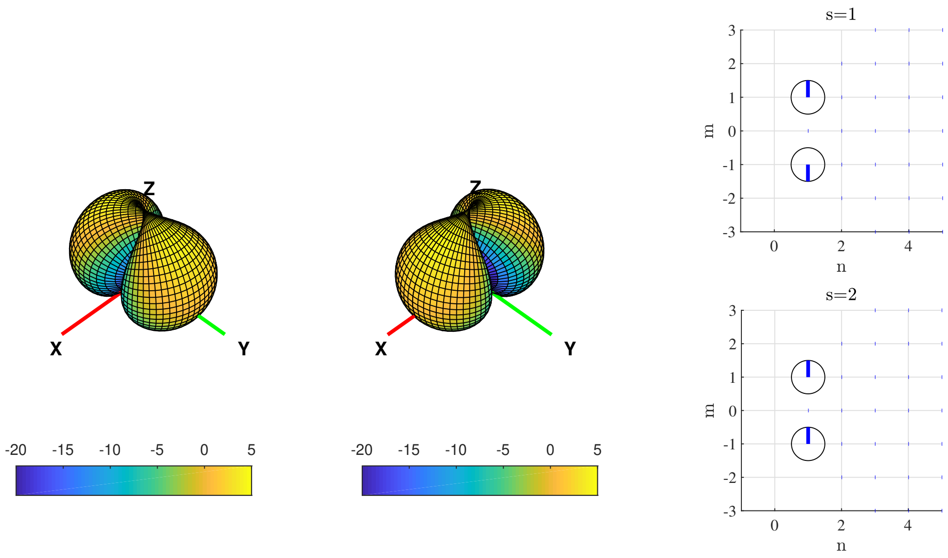

(A) (B)

FIGURE 1.15: Radiation pattern (A) and SWE (B) of a Huygens source polarized along the y axis.

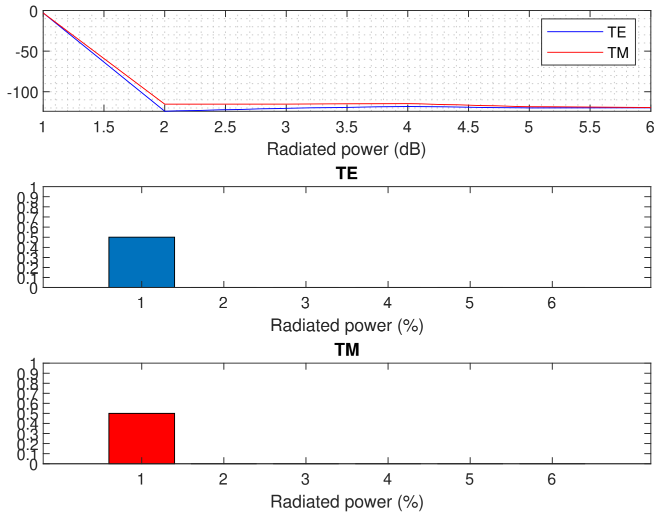

FIGURE 1.16: Power distribution on TE and TM modes of a Huygens source centered in the coordinate system.

For convenience in the following calculations where the maximum directivity of the antenna must be in the $\theta = 0$ direction, let the electric dipole be oriented on the y axis, transforming its far-field pattern to

$$\vec{f}_{ed}^{y} = cos\theta sin\phi \vec{e}_\theta + cos\phi \vec{e}_\phi \tag{1.40}$$

which can then be expanded to

$$\vec{f}_{ed}^{y} = \frac{1}{\sqrt{3}}(\vec{K}_{2-11} + \vec{K}_{211}) \tag{1.41}$$

Then, the magnetic dipole is oriented on the x axis and its far-field pattern is

$$\vec{f}_{md}^{x} = sin\phi \vec{e}_\theta + cos\theta cos\phi \vec{e}_\phi \tag{1.42}$$

$$= \frac{1}{\sqrt{3}}(\vec{K}_{1-11} - \vec{K}_{111}) \tag{1.43}$$

The far-field pattern of the Huygens source is thus the sum

$$\vec{f}_H = (1 + cos\theta)(sin\phi \vec{e}_\theta + cos\phi \vec{e}_\phi) \tag{1.44}$$

$$= \frac{1}{\sqrt{3}}(\vec{K}_{2-11} + \vec{K}_{211} + \vec{K}_{1-11} - \vec{K}_{111}) \tag{1.45}$$

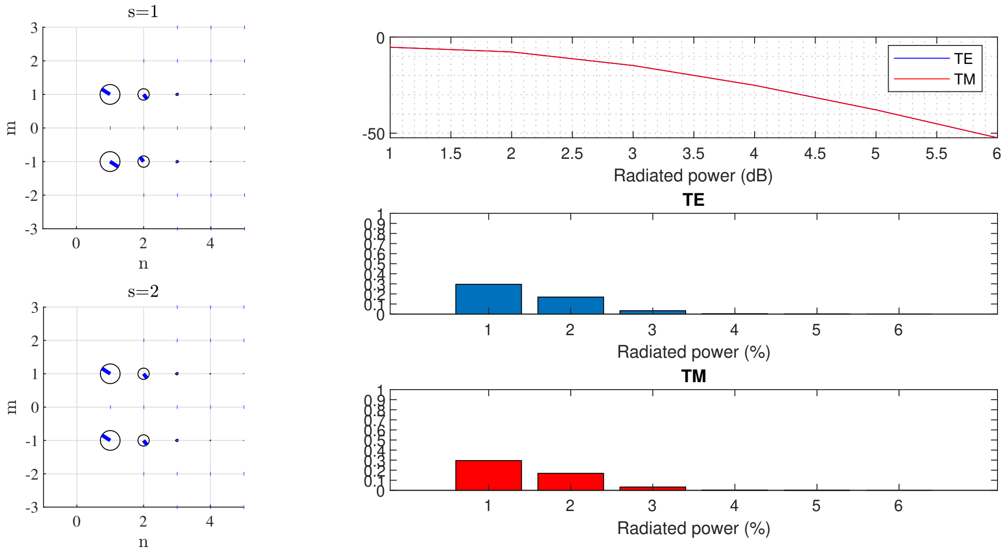

(A) (B)

FIGURE 1.17: SWE (A) and Power distribution on TE and TM modes (B) of a Huygens source polarized along the y axis and translated along the z axis.

Its maximum directivity is 3, in the $+z$ direction in this orientation setting. The SWE of the Huygens source polarized along the y axis is shown in Figure 1.15, showing the effect of translation along the z axis on 1.17. The power distribution of a Huygens source centered in the coordinate system, for any orientation, is shown in Figure 1.16.

Attention is drawn to the effects of this displacements relative to the coordinate system as it will be used in Chapter 3 to show the Spherical Wave that can be radiated by linear array antennas.

1.5 Conclusions

This concludes the introduction of the SWE that is the main analytic tool of this first part. The denotations presented here will be used in the rest of the report as well as the graphical representation of SWE that was shown. Also, dipoles and Huygens sources will be the radiation sources used in the study of linear end-fire arrays in the next Chapters and the SWE of their radiation pattern is detailed further in Chapter 3 in order to demonstrate how the directivity of these type of arrays can be maximized.

Chapter 2 will present some studies from the literature on fundamental physical limitations on antennas. These studies are based on the SWE and the property of each Spherical Wave, relatively to the radiation power they can convey as well as the energy they store in the near field. The set of Spherical Wave that maximize directivity is also demonstrated in the next Chapter, leading to Harrington's definition of ’normal directivity’ and thus superdirectivity, [3]. A survey of linear array theory is then made, presenting design method for superdirective antennas.

Chapter 2

Directivity Limits and Superdirectivity

The analysis of small antennas limitations are generally based on SWE theory that was introduced in Chapter 1. The studied limitations include quality factor, directivity and radiation efficiency when considering lossy materials.

The most fundamental work that uses the SWE approach is the one of Chu [36] that was mainly focused on quality factor analysis. This chapter is based on that publication and several other works following it, such as Collin and Rotschild [37] and Fante [38].

The work of Wheeler [2] is known for being a basis of small antenna studies as it defined this type of radiator by a size smaller than a sphere of radius $\frac{\lambda}{2\pi}$. This length determined the minimum sphere of influence of a radiator and was called 'radiansphere' by Wheeler. This work presented an analysis of particular antenna design such as electric dipoles, monopoles or loop antennas.

Chu [36] used a more general approach, taking as only known antenna parameter the radius of the sphere that can enclose it, allowing to perform the SWE outside of this sphere, in the free-of-charge region. The radius of this sphere, denoted 'a' will then defines the size of the analyzed antenna. SWE theory was also used to study the directivity limitations according to antenna size, in [3], [4] and [5]. The 'normal' directivity defined in [3] will hence be explained. This will lead to the definition of superdirectivity.

Moreover, as mentioned in the general introduction, theoretical approaches of superdirective antennas can be made from the study of Spherical Wave Functions but also from the study of array antennas. The fact that linear arrays of closely spaced elements with independent current feeding can reach directivities close to the square of their number of elements was demonstrated in the early work of Uzkov [9], which is also detailed in [12] and [13]. Moreover, the examination of dipole-based and Huygens-source-based arrays, from [26] are added to the isotropic-radiator-based arrays of [12] and [13].

This chapter is divided in two main sections, the first is dedicated to the analysis of the directivity limitations of on antenna through the use of SWE. The fact that the directivity can be limited as respect to various assumptions on the radiator is presented, introducing thus the notion of superdirectivity.

The second section then presents how superdirective antennas can theoretically be designed through compact end-fire arrays. This includes classical array theory as first demonstrated by Uzkov [9], but also a more recent design technique based on SWE, as presented in [21].

2.1 Directivity limits

In this section, the directivity limitations of a radiation pattern is reviewed through the study of the spherical waves required to reach a given value.

2.1.1 Directivity as a function of mode order

According to (1.22), (1.24) and (1.25) defined in Chapter 1, the antenna directivity can be calculated as

$$D(\theta,\phi) = \frac{|\sum_{smn} T_{smn}\vec{K}_{smn}(\theta,\phi)|^2}{\sum_{smn}|T_{smn}|^2} \tag{2.1}$$

Then, from Cauchy-Schwarz's inequality:

$$D(\theta,\phi) \leq \frac{\sum_{smn}|T_{smn}|^2 \sum_{smn}|\vec{K}_{smn}(\theta,\phi)|^2}{\sum_{smn}|T_{smn}|^2} \tag{2.2}$$

So the maximum directivity in the (θ,ϕ) direction is

$$D_{max}(\theta,\phi) = \sum_{smn} |\vec{K}_{smn}(\theta,\phi).\vec{i}^*_{co}|^2 \tag{2.3}$$

where $\vec{i}_{co}$ is the unit vector in the polarization direction. The condition of equality of (2.3)

$$T_{smn} = cte \cdot (\vec{K}_{smn}(\theta,\phi).\vec{i}^*_{co})^* \tag{2.4}$$

with cte an arbitrary real constant. The polarization does not affect the value of maximum directivity [34]. Also, Hansen [34] showed that the maximum directivity was independent to the desired polarization and could be expressed as:

$$D_{max}(\theta,\phi) = \sum_{mn} |\vec{K}_{1mn}(\theta,\phi)|^2 \tag{2.5}$$

Choosing the direction $\theta = 0$ then simplifies the calculation as only modes of order $m = 1$ or $m = -1$ are not equal to zero in that direction. This maximum directivity is of course independent of the chosen direction, as the reference system can always be rotated. Hence the maximum directivity is

$$D_{max}(0,\phi) = \sum_{n=1}^{N} \left\{ |\vec{K}_{11n}(0,\phi)|^2 + |\vec{K}_{1-1n}(0,\phi)|^2 \right\} \tag{2.6}$$

Taking arbitrarily $\phi = 0$. The calculation of $\vec{K}_{11n}(0,0)$ and $\vec{K}_{1-1n}(0,0)$ finally provides

$$D_{max}(0,0) = \sum_{n=1}^{N} (2n+1) = N^2 + 2N \tag{2.7}$$

There is no explicit limit for the maximum order N. Next section will however deal with the fact that the radiated power of spherical waves of higher orders tends ti decay faster the smaller the radiator is.

2.1.2 Directivity as a function of size

A directivity limit was previously defined in relation to the maximum order of radiated spherical waves. In this section, the analysis of the influence of radiator size to this maximum order of spherical wave is reviewed. This can be noticed by studying the radial dependance of the spherical waves described in (1.13) and (1.14). Considering outgoing waves in the space exterior to a sphere enclosing the radiation sources, these radial dependance are expressed by the functions

$$R_{1n}(kr) = h_n^{(1)}(kr) \tag{2.8}$$

and

$$R_{2n}(kr) = \frac{1}{kr} \frac{d}{d(kr)} \{krh_n^{(1)}(kr)\} \tag{2.9}$$

Plotting these functions for various order n over r shows a monotonous decay which can be splitted into two distinct sections, as shown in Figure 2.1.

The difference between the two sections is the slope that is sensibly higher in the first one. The radius where the slope shifts rapidly is called a 'cut off' point [3]. This radius R_c can be calculated as

$$kR_c = n \tag{2.10}$$

It was then proposed in [3] that this 'cut off' point could define the minimum space that a radiator must occupy in order to generate that particular order of spherical mode in a manner that its radiated power does not vanish quickly in free space. In other words, if the antenna covers a radius superior to that 'cut off' radius, the radiated wave will not go through that rapid amplitude decrease as it is not yet in free space. Furthermore, the minimum radius of the sphere that encloses the antenna is not large enough, some radiated waves will go through that important

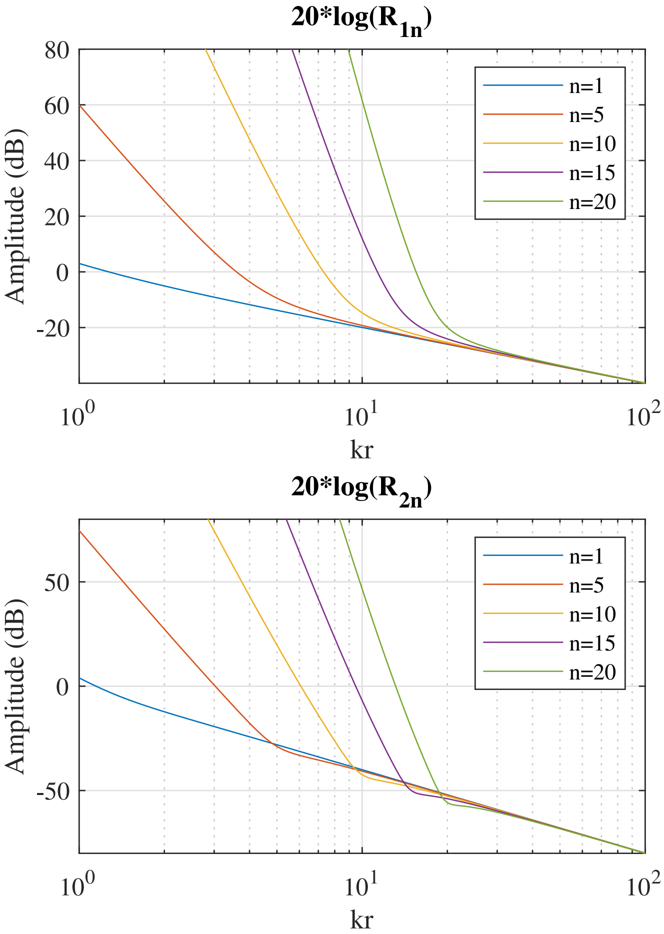

FIGURE 2.1: Evolution of the amplitude of the spherical waves as a function of radial distance r and mode order n.

power decrease zone which could only be compensated by providing a higher output power. This would be achieved by a larger current running through the antenna which would then increase the ohmic losses and decrease the radiation efficiency.

[3] then defines the 'normal directivity' limit by limiting the maximum order of radiated spherical waves to $N = ka$ where a is the minimum radius of a sphere that encloses the antenna. a will be referred to as the antenna radius in the following for brevity. This limit is then equal to

$$D_{max}^{H} = (ka)^2 + 2ka \tag{2.11}$$

This expression shows that when a tends to infinity, the limits tends to the well-known limit of directivity of an uniformly illuminited aperture. This limit is defined as [35]

$$D_{aper} = \frac{4\pi S}{\lambda^2} \tag{2.12}$$

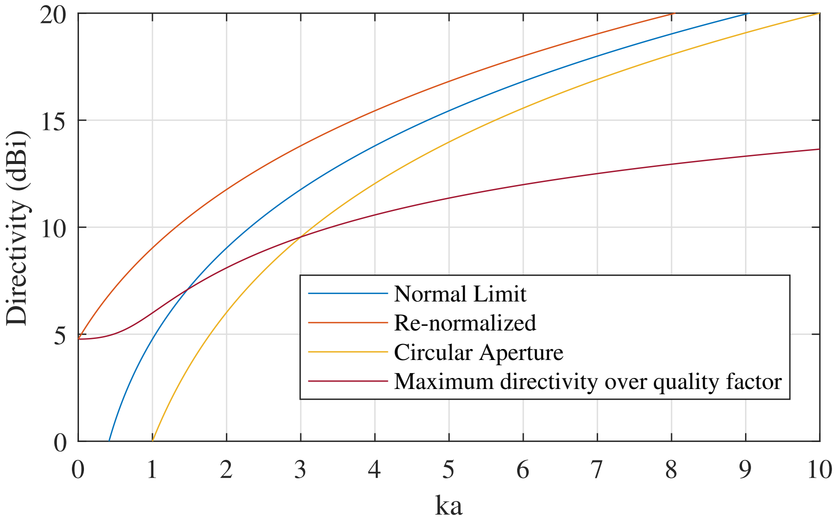

FIGURE 2.2: Limits of directivity as a function of antenna size (ka).

where S is the surface area of the aperture. If it is circular of radius a, $S = \pi a^2$ and the formula becomes

$$D_{aper} = (ka)^2 \tag{2.13}$$

The 'normal'directivity limits then offers a relevant description of classical directive antennas such as aperture antennas and broadside array antenna. Both these limit are however irrelevant when a is small and their values become inferior to one. For this case, the expression $D^H_{max} = (ka)^2 + 2ka + 1$ was proposed in [3]. Another re-normalization of this limit was proposed in [39] where the mode order N would be at least equal to one, providing a minimum directivity of $1^2 + 2(1) = 3$ which is the directivity of the theoretical Huygens source that will be introduced in section 3.1. This re-normalized limit would then be equal to

$$\begin{aligned} D^{re-norm}_{max} &= (ka)^2 + 2ka + 3 \\ D^{re-norm}_{max} &= (k(a+\frac{1}{k}))^2 + 2k(a+\frac{1}{k}) \end{aligned} \tag{2.14}$$

It can be noticed that this can be interpreted as the addition of a minimum radius of $\frac{1}{k} = \frac{\lambda}{2\pi}$ which is also the radius of the minimum sphere of influence, the radiansphere, defined by Wheeler in [2] as mentionned in the introduction.

The corresponding curves are displayed in Figure 2.2, as a directivity limit that take into account the quality factor of the antenna. The maximum directivity over quality factor curve is the maximum directivity reached when maximizing the ratio directivity over quality factor. It was computed from [5], which is explained further in section 3.2.

2.1.3 Directivity limit in relation to quality factor

As mentioned in the introduction, optimizing an antenna's directivity comes with another trade-off which is its quality factor. The quality factor of an electrical network can be defined as [37]

$$Q = \frac{\omega W}{P} \tag{2.15}$$

where $\omega = 2\pi f$, W is the time-averaged energy stored in the network and P is the power dissipated in the network. The energy stocked in the network is the sum of the electric (W^e) and magnetic (W^m) energy. The quality factor of the antenna is calculated in the resonant case where $W^e = W_m$ and can then also be written in the form

$$Q = \frac{2\omega W^m}{P} = \frac{2\omega W^e}{P} \tag{2.16}$$

The interest of studying this quantity comes from the fact that it can be related to the antenna's possible working bandwidth. It is shown in [40] for instance, that the fractional bandwidth of the antenna is inversely proportional to its quality factor, when this factor is large compared to one. A theoretical minimum quality factor can be calculated for the case of an antenna considering an equivalent waveguide model for each wave allowing to derive an equivalent characteristic impedance, as demonstrated by the early work of Chu [36].

The equivalent circuit model was previously proposed in [36], deriving equivalent voltages and currents from the power calculated for each spherical wave, at the radius a that delimits the physical boundaries of the radiator. The far-field approximation is not relevant here, as the calculations are made next to the radiator, so the general expression of $F^{(3)}_{smn}$ is used, as well the general Poynting vector expression of (1.22). It is demonstrated in [33] that

$$\int_0^{2\pi}\int_0^{\pi}[F^{(3)}_{smn}(a,\theta,\phi) \times F^{(3)}_{\sigma\mu\nu}(a,\theta,\phi)].\vec{e}_r sin\theta d\theta d\phi = -\delta_{-m,\mu}\delta_{n,\nu}R_{1n}(ka)iR_{2n}(ka) \tag{2.17}$$

where $\delta_{n,\nu}$ is the Kronecker index defined as

$$\begin{aligned} \delta_{n,n} &= 1, \\ \delta_{n,\nu} &= 0, n \neq \nu \end{aligned} \tag{2.18}$$

Hence, the total complex power at radius a is

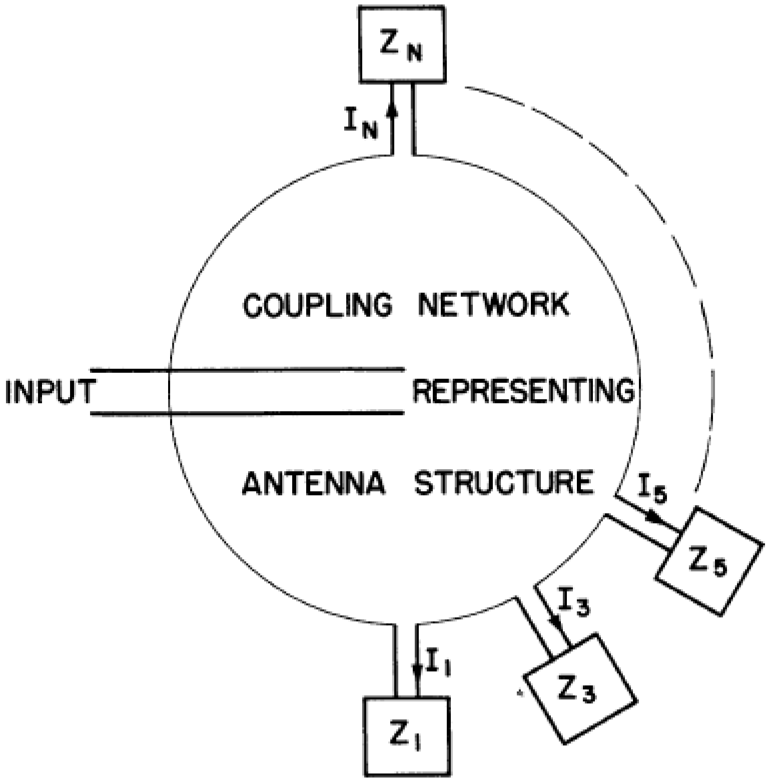

FIGURE 2.3: Waveguide model of the SWE [36].

$$P_{tot}(ka) = 4\pi \int_0^{2\pi}\int_0^{\pi} r^2\langle\vec{E}\times\vec{H}^*\rangle.\vec{e}_r sin\theta d\theta d\phi$$
$$P_{tot}(ka) = \frac{1}{2}\sum_{smn}|T_{smn}|^2|R_{1n}(ka)iR_{2n}(ka) \tag{2.19}$$

This can be written as the product of equivalent voltages and currents for each spherical wave with [3]

$$V_{1mn} = \sum_{smn} T_{1mn}R_{1n}(ka) \tag{2.20}$$

$$I_{1mn} = \sum_{smn} T_{1mn}iR_{2n}(ka) \tag{2.21}$$

for TE waves and

$$V_{2mn} = \sum_{smn} T_{2mn}iR_{2n}(ka) \tag{2.22}$$

$$I_{2mn} = \sum_{smn} T_{2mn}R_{1n}(ka) \tag{2.23}$$

for TM waves. Their characteristic impedance are then deduced from the ratio of voltage over current, [36], [41]

$$Z_{1n}(ka) = \frac{R_{1n}(ka)}{iR_{2n}(ka)} \tag{2.24}$$

for TE wave and

$$Z_{2n}(ka) = \frac{iR_{2n}(ka)}{R_{1n}(ka)} \tag{2.25}$$

The quality factor can be calculated for each wave as a function of mode order n [3]:

$$Q_n = \frac{2\omega W_n^m}{Re(P_n)} = \frac{2\omega W_n^e}{Re(P_n)} \tag{2.26}$$

The stocked energy was first calculated in [36] with an approximated equivalent RLC network for each wave. This was later improved in [37] where it was calculated directly from the electric and magnetic field by substracting the energy of the propagating radiated field to the energy of the total calculated field outside the sphere of radius a. Hence, from [38],

$$W^e + W^m \approx \int_a^{\infty} [\int_0^{2\pi} d\phi \int_0^{\pi} \{\frac{\epsilon_0}{4}|\vec{E}|^2 + \frac{\mu_0}{4}|\vec{H}|^2\} sin\theta d\theta r^2 - \frac{P_r ad}{v}] \tag{2.27}$$

where $v = (\epsilon_0 \mu_0)^{-\frac{1}{2}}$ is the velocity of the wave. Calculation of W^e or W^m specifically is then made by adding the complex Poynting theorem which gives [38]

$$W^m - W^e = \frac{1}{4\omega} Im[\int_0^{2\pi} d\phi \int_0^{\pi} (\vec{E} \times \vec{H}^*) \cdot \vec{e}_r sin\theta d\theta a^2] \tag{2.28}$$

A general expression for any directional antenna was thus given in [38], differentiating two types of modal quality factor, Q_n and Q'_n, with

$$\frac{2\omega W^e}{P_{rad}} = \frac{\sum_{n=1}^{\infty}(a_n^2 Q_n + b_n^2 Q'_n)}{\sum_{n=1}^{\infty}(a_n^2 + b_n^2)} \tag{2.29}$$

$$\frac{2\omega W^m}{P_{rad}} = \frac{\sum_{n=1}^{\infty}(a_n^2 Q'_n + b_n^2 Q_n)}{\sum_{n=1}^{\infty}(a_n^2 + b_n^2)} \tag{2.30}$$

The quality factor Q being equal to the largest of the above quantities, with

$$a_n^2 = \sum_{m=-n}^{n} |Q_{2mn}| \tag{2.31}$$

$$b_n^2 = \sum_{m=-n}^{n} |Q_{1mn}| \tag{2.32}$$

Q_n is then the quality factor associated with the electric stocked energy W^e, respectively the magnetic stocked energy W^m, associated with a TM spherical wave, respectively TE spherical wave. Inversely, Q'_n is the factor associated with the magnetic stocked energy W^m, respectively the electric stocked energy W^e, associated with a TM spherical wave, respectively TE spherical wave. These factors are given by the formulas [38]

$$Q_n = ka - |h_n^{(2)}(ka)|^2[\frac{(ka)^3}{2} + ka(n+1)] - \frac{(ka)^3}{2}|h_{n+1}^{(2)}(ka)|^2 \tag{2.33}$$

$$+(ka)^2(\frac{2n+3}{2})[j_n(ka)j_{n+1}(ka) + y_n(ka)y_{n+1}(ka)] \tag{2.34}$$

$$Q'_n = ka - \frac{(ka)^3}{2}[|h_n^{(2)}(ka)|^2 - j_{n-1}(ka)j_{n+1}(ka) - y_{n-1}(ka)y_{n+1}(ka)] \tag{2.35}$$

It is to be noted that this theoretical expression of Q does not take into account the energy stored in the sphere of radius a enclosing the antenna as the calculations are made from the spherical wave radiated in the free-of-charge space outside of it. It is then a theoretical lower bound for Q. The maximum directivity with the constraint of minimizing this Q factor was then calculated, most recently in [5], proving that equal excitation between TE and TM modes was the best case. This provided the formulas

$$max(\frac{D}{Q}) = 2\sum_{n=1}^{\infty} \frac{(2n+1)}{Q_n^{TM} + Q_n^{TM}} \tag{2.36}$$

with

$$Q_{dir}^{min} = \frac{\sum_{n=1}^{\infty} \frac{(2n+1)}{(Q_n^{TM}+Q_n^{TM})}}{2\sum_{n=1}^{\infty} \frac{(2n+1)}{(Q_n^{TM}+Q_n^{TM})^2}} \tag{2.37}$$

and

$$D_{dir}^{max} = \frac{[\sum_{n=1}^{\infty} \frac{(2n+1)}{(Q_n^{TM}+Q_n^{TM})}]^2}{\sum_{n=1}^{\infty} \frac{(2n+1)}{(Q_n^{TM}+Q_n^{TM})^2}} \tag{2.38}$$

Figure 2.2 displays D_{dir}^{max} along with the other directivity limits. With a directivity of 3 and an infinitesimal size, the Huygens source is then the smallest theoretical radiator that reaches that limit. The consideration of quality factor will not be explored further in this thesis, as the bandwidth optimization is out of its scope. The equivalent waveguide mode for spherical waves will however be used for the study of efficiency through the dissipation factor defined in [41]. This is developed in Chapter 3.

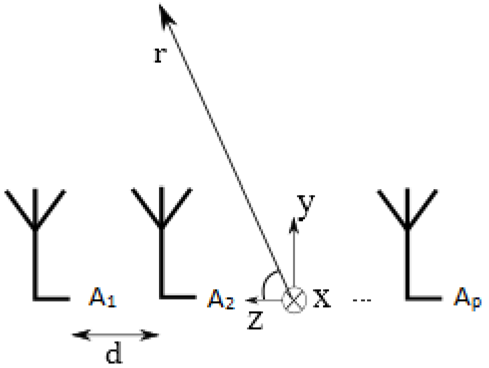

FIGURE 2.4: Linear array of independently excited elements.

2.2 Superdirectivity

Having defined directivity limits in section 2.1, an antenna can be considered superdirective when its directivity is greater that one of these limits. Methods from the literature to design superdirective antennas are detailed in this section.

2.2.1 Array theory optimization method

The possibility of designing superdirective antennas was theoretically demonstrated in [9], with array antennas of closely spaced radiating elements. Also, each source has to be properly excited in amplitude and phase. In this section, the theory of end-fire arrays will then be introduced to show how to maximize their directivity with proper excitation coefficients. These type of arrays are well suited for superdirectivity as the spacing between elements can be reduced, increasing even more their maximum directivity as it will be shown. The denotations and hypothesis will be presented in the first section. The next sections deal with the effect on efficiency, sensitivity and directivity, of independently tapering the currents on the elements of the arrays. Methods to maximize directivity or gain for lossy antennas are then explained in the last section.

Note that this sections uses the denotation $e^{j\omega t}$ for the time dependence of the fields, as it is the one used by most of the works taken as references here.

The far-field approximation is always be considered in this section, such that the distance between the elements of the arrays can be neglected next to the observation distance r defined in Chapter 1. Also, the far-field pattern function will be used which is here defined as the part of the electric field that depends on the θ and ϕ angles. The far-field pattern of an array of P radiating elements can then be expressed by:

$$\vec{F}(\theta,\phi) = \sum_{p=1}^{P} A_p \vec{f}_p(\theta,\phi) e^{jk\vec{e}_r \cdot \vec{r}_p} \tag{2.39}$$

The A_p are the complex excitation coefficients and are proportional to the currents running through the array elements. $\vec{e}_r$ is the unit vector in the far-field direction (θ, ϕ). The terms $\vec{f}_p(\theta, \phi)$ are the element far-field patterns, phase referenced to their position defined by $\vec{r}_p$. Here, we assume that the terms $\vec{f}_p(\theta, \phi)$ in their environment do not change with the excitation coefficients. From (2.39), as the far-field pattern is proportional to the radiated electric field, the directivity of the array in the (θ_0, ϕ_0) direction can also be expressed in the form:

$$D = \frac{|\sum_{p=1}^{P} A_p \vec{f}_p(\theta_0, \phi_0) e^{jk\vec{e}_{r0}\cdot\vec{r}_p}|^2}{\frac{1}{4\pi}\int_0^{2\pi}\int_0^{\pi} |\sum_{p=1}^{P} A_p \vec{f}_p(\theta, \phi) e^{jk\vec{e}_r\cdot\vec{r}_p}|^2 sin\theta d\theta d\phi} \tag{2.40}$$

where $\vec{e}_{r0}$ is the unit vector in the far-field direction (θ_0, ϕ_0). Let us find the A_p coefficients that maximize this directivity. In order to find the A_p that maximize 2.40, more convenient denotations can be used. According to [14], [42], (2.40) can be written in the form:

$$D = \frac{\sum_{m=1}^{P}\sum_{p=1}^{P} A_p A_m^* \vec{f}_p(\theta_0, \phi_0) \vec{f}_m^*(\theta_0, \phi_0) e^{jk\vec{e}_{r0}\cdot\vec{r}_p} e^{-jk\vec{e}_r\cdot\vec{r}_m}}{\sum_{m=1}^{P}\sum_{p=1}^{P} A_p A_m^* H_{mp}} \tag{2.41}$$

with

$$H_{mp} = \frac{1}{4\pi}\int_0^{2\pi}\int_0^{\pi} \vec{f}_p(\theta, \phi) \vec{f}_m^*(\theta, \phi) e^{jk\vec{e}_r\cdot(\vec{r}_p - \vec{r}_m)} sin\theta d\theta d\phi \tag{2.42}$$

or

$$D = \frac{\sum_{m=1}^{P}\sum_{p=1}^{P} a_p a_m^* e^{jk\vec{e}_{r0}\cdot\vec{r}_p} e^{-jk\vec{e}_r\cdot\vec{r}_m}}{\sum_{m=1}^{P}\sum_{p=1}^{P} a_p a_m^* h_{mp}} \tag{2.43}$$

with

$$a_p = A_p |\vec{f}_p(\theta_0, \phi_0)| \tag{2.44}$$

and

$$h_{mp} = \frac{H_{mp}}{\vec{f}_p(\theta_0, \phi_0) \cdot \vec{f}_m^*(\theta_0, \phi_0)} \tag{2.45}$$

The directivity can then be expressed in the matricial form

$$D = \frac{\mathbf{a}^*.\mathbf{C}.\mathbf{a}}{\mathbf{a}^*.\mathbf{H}.\mathbf{a}} \tag{2.46}$$

with **a** the column vector of the a_p coefficients, $\mathbf{a}^*$ its conjugate transpose, **C** and **H** the matrices defined by $(\mathbf{C}_{mp}) = e^{jk\vec{e}_r\cdot(\vec{r}_p - \vec{r}_m)}$ and $(\mathbf{H}_{mp}) = h_{mp}$, respectively. The directivity is then the ratio of two hermitian quadratic form which is maximized according to a theorem from linear algebra when the denominator is positive definite [13]. This theorem stipulates that the maximum value of D is equal to the largest eigenvalue $\lambda = \lambda_0$ of the eigenvalue problem

$$\mathbf{C}.\mathbf{a} = \lambda \mathbf{H}.\mathbf{a} \tag{2.47}$$

It can be shown that only one of the eigenvalues of that problem is not zero [13]. This is shown in Appendix B. (2.47) simultaneously defines the $\mathbf{a}_0$ vector that maximize the directivity. This can also be expressed as

$$\sum_{p=1}^{P} e^{jk\vec{e}_r\cdot(\vec{r}_p-\vec{r}_m)} a_{0p} = \lambda_0 \sum_{p=1}^{P} h_{mp} a_{0p}, m = 1, 2, ..., P \tag{2.48}$$

The term $\sum_{p=1}^{P} e^{jk\vec{e}_r\cdot\vec{r}_p} a_{0p}$ does not depend on m and can then be a constant factor of the first term of (2.48). Hence, the excitation coefficients A_{0p} maximizing the directivity expression in (2.40) are given by

$$\sum_{p=1}^{P} h_{mp} A_{0p} \vec{f}_p(\theta_0, \phi_0) = ce^{-jk\vec{r}_0\cdot\vec{r}_m}, m = 1, 2, ..., P \tag{2.49}$$

with c an arbitrary constant. In the case of uniformly spaced end-fire arrays aligned on the z axis, the phases of the element of $\mathbf{C}$ become

$$\vec{e}_r \cdot \vec{r}_p = (p-1) d cos\theta \tag{2.50}$$

with d the distance between elements. Considering simple cases of element patterns $\vec{f}(\theta, \phi)$, identical for every elements of the array, the maximum directivity can be computed as a function of d.

In the case where elements are isotropic radiators, $\vec{f}(\theta, \phi) = 1$. Thus, (2.45) becomes

$$\begin{aligned} h_{mp} &= \frac{1}{4\pi} \int_0^{2\pi} \int_0^{\pi} e^{jk\vec{e}_r\cdot(\vec{r}_p-\vec{r}_m)} sin\theta d\theta d\phi \\ &= \frac{sinkd(m_p)}{kd(m-p)}, m \neq p \end{aligned} \tag{2.51}$$

and

$$h_{mm} = 1 \tag{2.52}$$

In the case of electric or magnetic dipole, $\vec{f}(\theta, \phi) = cos\theta sin\phi \vec{e}\theta + cos\phi \vec{e}_\phi$, so

$$|\vec{f}(\theta, \phi)|^2 = cos^2\theta cos^2\phi + sin^2\phi \tag{2.53}$$

and

$$h_{mp} = \frac{1}{4\pi}\int_0^{2\pi}\int_0^{\pi}(cos^2\theta cos^2\phi + sin^2\phi)e^{jk\vec{e}_r\cdot(\vec{r}_p-\vec{r}_m)}sin\theta d\theta d\phi$$
$$= \frac{sinkd(m_p)}{kd(m-p)}(1-\frac{1}{[kd(m-p)]^2}) + \frac{coskd(m_p)}{[kd(m-p)]^2}, m \neq p \qquad (2.54)$$

and

$$h_{mm} = \frac{2}{3} \qquad (2.55)$$

In the case of a Huygens source, $\vec{f}(\theta,\phi) = (1+cos\theta)(sin\phi\vec{e}\theta + cos\phi\vec{e}_\phi)$, so

$$|\vec{f}(\theta,\phi)|^2 = (1+cos^2\theta) \qquad (2.56)$$

and

$$h_{mp} = \frac{1}{4\pi}\int_0^{2\pi}\int_0^{\pi}(1+cos^2\theta)e^{jk\vec{e}_r\cdot(\vec{r}_p-\vec{r}_m)}sin\theta d\theta d\phi$$
$$= 2H^d_{mp}p + 2jkd(m-p)(H^d_{mp}p - H_{mp}), m \neq p \qquad (2.57)$$

and

$$h_{mm} = \frac{1}{3} \qquad (2.58)$$

Maximum directivities as a function of inter-element spacing are shown for dipole-based and Huygens-source-based arrays in Figure 2.6. This shows that the directivity tends to a maximum when the inter-element spacing tends to zero. It was demonstrated in [9] that the directivity of a P-isotropic-source based arrays tends to P^2 when the inter-element spacing tends to zero. This maximum seems to be equal to $P^2 + 2P$ for Huygens-source-based arrays, as it was noticed in [26]. This last assessment will be investigated in Chapter 3. The maximum directivity of dipole-based arrays is 5.25 for a two-element array and is about 10.72 and 18.41 for three- and four-dipole arrays.

2.2.2 SWE-based optimization method

Knowing the spherical waves required to maximize the directivity of a radiation pattern, the direct problem of designing antennas that radiates the proper modes was investigated. In [21], a method to optimize the spherical waves radiated by a compact end-fire arrays is presented. This alternative method uses the SWE to compute the excitation coefficients to apply to each array element to maximize directivity. This method uses the computed radiated field of the elements of the array to derive their SWE and then calculate the coefficients that will provide the spherical mode combination that is the closest to the known optimal modes defined by (2.4). The algorithm of the design method is schematized in Figure 2.5, along with the array-theory-based method. The first step is thus the calculation or measurement of the radiated field. The second step is the SWE that uses the method presented in 1.3. The third step is then the derivation of the optimal excitation coefficients. They can be derived knowing that the total electric field radiated by the array antenna is the sum of the fields radiated by each element, as expressed by the array factor in (2.39):

$$\vec{E} = \sum_{p=1}^{P} \alpha_p \vec{E}_p \tag{2.59}$$

Moreover, the SWE for each element gives, from (1.21),

$$\vec{E}_p = \frac{\sqrt{\eta}k}{\sqrt{4\pi}} \frac{e^{jkr}}{kr} \sum_{smn} T_{smn,p} \vec{K}_{smn} \tag{2.60}$$

$T_{smn,p}$ is the Spherical Wave Coefficient computed from the SWE of the p-th element when no other element is feeded. Thus

$$\vec{E} = \frac{\sqrt{\eta}k}{\sqrt{4\pi}} \frac{e^{jkr}}{kr} \sum_{p=1}^{P} \sum_{smn} \alpha_p T_{smn,p} \vec{K}_{smn} \tag{2.61}$$

which can be rearranged as

$$\vec{E} = \frac{\sqrt{\eta}k}{\sqrt{4\pi}} \frac{e^{jkr}}{kr} \sum_{smn} \vec{K}_{smn} \sum_{p=1}^{P} \alpha_p T_{smn,p} \tag{2.62}$$

The goal is to reach the spherical wave distribution defined by

$$\vec{E}^{opti} = \frac{\sqrt{\eta}k}{\sqrt{4\pi}} \frac{e^{jkr}}{kr} \sum_{smn} T^{max}_{smn} \vec{K}_{smn} \tag{2.63}$$

where T^{max}_{smn} is the optimal Spherical Wave Coefficient defined in (2.4).
This is then done by optimizing the system

$$T^{max}_{smn} = \sum_{p=1}^{P} \alpha_p T_{smn,p}, p = 1, 2..., P \tag{2.64}$$

As previously seen in section 1.4, even if the array elements are identical, the difference of position only creates different radiated modes. Moreover, when the SWE is made from a field calculated through a full-wave simulation, the near-field coupling between the elements is also taken into account. The maximum order of the SWE can be adjusted according to the precision required. This precision can be checked through the difference of power calculated from the given radiated field and from the Spherical Waves derived, as mentioned in section 1.3. Hence the system described in (2.64) is in general over-determined and is then optimized through a Least Mean Square matricial method.

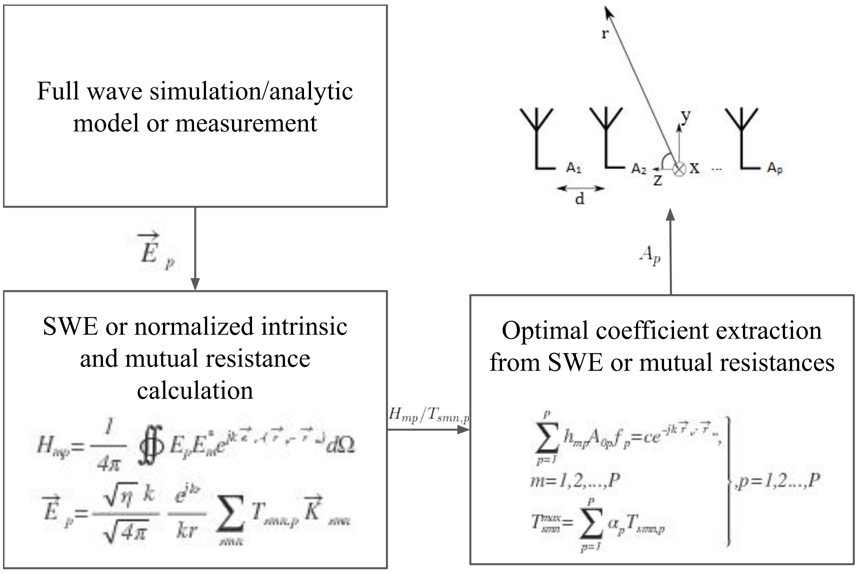

FIGURE 2.5: Optimization procedures with equations from both array-theory-based and SWE-based methods.

This method is equivalent to the one presented in section 2.2.1 as it provides similar results as shown in Figure 2.6 for dipole-based and Huygens-source-based arrays. The method introduced in 2.2.1 is indicated as 'classical method'.

This demonstrates that the optimization of radiated spherical wave and the direct optimization of the directivity of array antennas are equivalent. Both approach to superdirectivity were now presented. Displays of excitation coefficients which are similar for both methods are presented in Appendix C.

2.2.3 Survey of other optimization methods

As mentioned in the general introduction, several different techniques for optimizing antenna arrays' directivity have been developped. Both previously presented methods however already reach the theoretical maximum directivity, as shown in section 2.2.1.

Hence, the other methods have different purpose, such as Dolph's method [8] which aims at reaching specific opening angles and secondary lobes levels. More recently, methods based on the Characteristic Modes theory were also developped. This theory published by Harrington and Mautz [43], [44] is a way to analyze the currents running through a radiator or scatterer through a modal expansion of these currents. This can be used in the study or design of antenna with specific radiation pattern, directivity, efficiency, quality factor or impedance properties [45].

Hence, recent works based on Characteristic Modes were made to find the current distributions that would minimize quality factor [46] or provide a tradeoff between efficiency and quality factor [47]. Moreover, these analysis were also applied

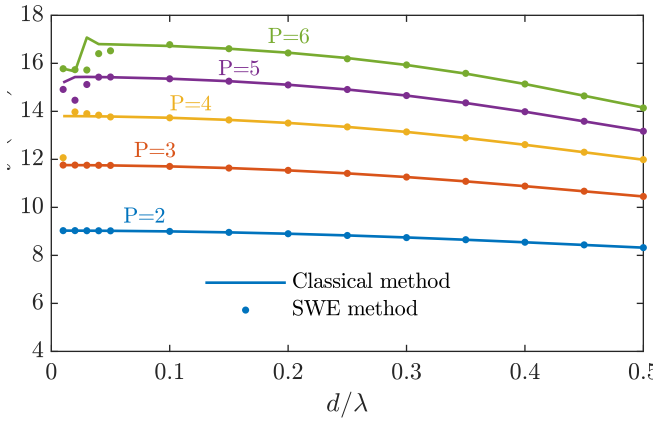

(A) Huygens source based array.

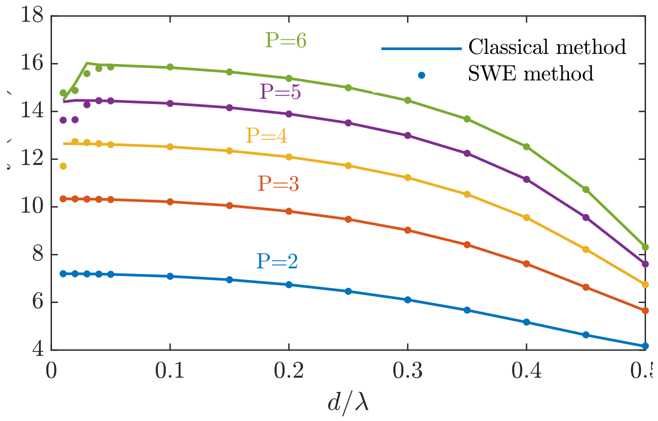

(B) Dipole based array.

FIGURE 2.6: Directivity of P-element arrays as a function of inter-element spacing (d).

for superdirective antenna design as it would allow for the optimization of bandwidth and impedance matching as well as antenna directivity [48]–[51].

The present thesis's primary focus is to determine theoretical boundaries for directivity and gain of superdirective arrays, in which case the use of array factor and SWE theory is sufficient. Characteristic Modes theory is thus not used or detailed in this report and further information on the matter can be found in the previously cited publication.

Also, another method based on Infinitesimal Dipole Model and Cross-Correlation Theory with Green Functions is presented in [52]. This method was made in a more general purpose to reach different goals that would be required by MIMO systems, even if it is applied for superdirective array optimization in that paper. The directivity reach is however below the theoretical maximum.

2.3 Conclusions

In this Chapter, the literature on the fundamental limitations of antennas relatively to their size was surveyed, focusing on the analysis of maximum directivity. This lead to the introduction of directivity limits which would then define superdirectivity as a directivity beyond one of these limits. In particular, the 'normal directivity' defined in [3] will be used in the rest of the report to determine superdirectivity or supergain.

The theory of superdirective compact end-fire arrays was also introduced in this Chapter from several sources of the literature. Hence, methods to calculate the excitation coefficients and the maximum directivities of isotropic-sources-based, dipole-based or Huygens-source-based arrays were shown. This was demonstrated through classical array factor theory and with a SWE-based method.

The classical method for deriving superdirective arrays excitation coefficients is the most straigth forward and simple to implement. It also allows for gain maximization with the mere addition of the loss resistance parameter in the equation to solve, as it is detailed in Chapter 3. The SWE-based method is more complex to implement but is designed to make the array match any given spherical wave distribution so this method can be modified to reach different requirements. One possible application would be to optimize the ratio directivity over quality factor as derived in [5], or to minimize the quality factor.

In the following, the relation between fundamental antenna limitations and array theory will be investigated further. First, the link between general directivity limits and maximum linear array directivity is analyzed in an original contribution. Then, the constraints that appear on the antenna radiation efficiency as well as the precision requirements on excitation coefficients are examined in Chapter 3, also proposing further development to the optimization of supergain arrays through the specific maximization of gain when considering lossy antennas.

Chapter 3

Superdirectivity and Supergain Analysis

The study of superdirectivity can be made from two different approaches that were presented in the first two Chapters. One approach involves the examination of the spherical waves radiated by the antenna and the implications that are made regarding antenna size, when aiming to reach a certain directivity. This is detailed in section 2.2.2. The second method, presented in section 2.2.1, is based upon the study of array antennas. It is indeed demonstrated that directivities as high as desired can theoretically be obtained with array antennas as small as desired, with the right excitation coefficient applied to each array element. In this Chapter, the relations between both approaches are investigated. The proposed analysis also provides a proof of the directivity upper limits of Huygens-source- and dipole-based linear arrays.

In the second section, studies of gain limitations from the literature are reviewed. These studies aim at linking the radiation efficiency to the antenna size, considering the radiated Spherical Wave Functions. These analysis are similar to the ones made on the quality factor but also require some knowledge of the antenna geometry and material, to determine its conduction losses.

Then, the literature studies of array antenna limitations are also surveyed [12], [13]. The gain limitations according to single element loss resistance is demonstrated. Moreover, the sensitivity of the array directivity to the errors made on excitation coefficients is also quantitatively analyzed. Starting from the considerations proposed in [13], it is also shown that the gain of the array can be maximized instead of its directivity when considering loss resistances. A modification of the optimization procedure to synthesize the array excitation coefficients in the case of gain maximization is proposed. The use of this optimization is demonstrated in this chapter through full electromagnetic simulations of halfwave-dipole-based arrays. Finally, the general gain limits derived in [41] and [53] are compared to the supergain array limits, leading to a discussion on the interests of such arrays.

3.1 End-fire arrays directivity limits

In section 2.2, the computation of the maximum directivity as a function of inter-element spacing of an end-fire array of P Huygens sources showed that this directivity tends to $P^2 + 2P$ when the spacing tends to zero. An analysis based on the SWE is conducted in this section to provide the proof and physical interpretation of that result.

3.1.1 Huygens-source-based arrays

The far-field pattern of an array of P radiating elements can be expressed by (2.39). In the following as in section 2.2.1, the far-field patterns of the P antennas will be considered to be the same, denoting $\vec{f}_p(\theta,\phi) = \vec{f}(\theta,\phi)$. Aligning the elements on the z axis to maximize directivity in the $\theta = 0$ direction, the path differences becomes

$$\vec{e}_r \cdot \vec{r}_p = (p-1)cos\theta \tag{3.1}$$

For a polarization $\vec{i}_{co} = \vec{y}$ ($\phi = 90$), the mode combination that maximizes directivity in the ($\theta = 0$) direction is, from (2.4):

$$T_{11n} = -T_{1,-1,n} = T_{21n} = T_{2,-1,n} = cte \cdot (\frac{-i^n}{2}\sqrt{2n+1}) \tag{3.2}$$

where cte is an arbitrary constant. As both SWE theory and array theory formulas are used in this section, the denotation chosen here is $e^{-i\omega t}$ for the time dependence. This implies that array theory equations that previously used the $e^{j\omega t}$ standard will be modified by writing $i = -j$.

The other coefficients are equal to 0 for $m \neq \pm 1$. Putting the Huygens sources in a linear array along the z axis, the global far-field pattern is given by (2.39) and (1.44). As shown in section 1.4, the multiplication by $e^{-ik(p-1)dcos\theta}$ cannot change the number of azimutal oscillations m (term $e^{im\phi}$ in the wave functions) and therefore cannot generate modes of order $m \neq \pm 1$. Only modes of superior order n and of azimuthal index $m = \pm 1$ shall appear, as it is shown in Chapter 1, section 1.4.

What's more, when the spacing between elements approaches zero, developing the exponential in a power series one could rewrite that far field pattern as

$$\vec{F}(\theta,\phi) = \vec{f}(\theta,\phi) \sum_{p=1}^{P} \alpha_p \sum_{j=0}^{P-1} \frac{(-ik(p-1)dcos\theta)^j}{j!} + o(d^{P-1}) \tag{3.3}$$

where $o(d^{P-1})$ means a value that is negligible next to d^{P-1} when d tends to zero. This can also be expressed as:

$$\vec{F}(\theta,\phi) \sim \vec{f}(\theta,\phi) \sum_{j=1}^{P} B_i cos^{j-1}\theta \tag{3.4}$$

with

$$B_j = \frac{(-ikd)^i}{j!} \sum_{p=1}^{P} (p-1)^j \alpha_p \tag{3.5}$$

Let us prove that there is a set of α_p coefficients such that, when the inter-element spacing d is in the vicinity of zero, the SWE of the array is the one defined by (3.2).

Using (1.19) and (1.20) gives,

$$\begin{aligned} \vec{K}_{11n} - \vec{K}_{1,-1,n} + \vec{K}_{21n} + \vec{K}_{2,-1,n} = \sqrt{\frac{2}{n(n+1)}} (-i)^{n+1} \cdot \\ 2\left(\frac{d\overline{P}_n^1(cos\theta)}{d\theta} + \frac{\overline{P}_n^1(cos\theta)}{sin\theta}\right)[sin\phi\vec{e}_\theta + cos\phi\vec{e}_\phi] \end{aligned} \tag{3.6}$$

Now, it can be shown (cf. Appendix A.1) that:

$$\begin{aligned} \exists \{c_{k,n}\}_{k\in[|0,n|]} \in \mathbf{R}^{n+1}, \frac{d\overline{P}_n^1(cos\theta)}{d\theta} + \frac{\overline{P}_n^1(cos\theta)}{sin\theta} \\ = (1+cos\theta) \sum_{k=1}^{n} c_{k,n} cos^{k-1}\theta \end{aligned} \tag{3.7}$$

Thus, from (3.6) and (3.7):

$$\vec{K}_{11n} - \vec{K}_{1,-1,n} + \vec{K}_{21n} + \vec{K}_{2,-1,n} = \vec{f}(\theta,\phi) \sum_{k=1}^{n} c'_{k,n} cos^{k-1}\theta \tag{3.8}$$

with

$$\begin{aligned} c'_{k,n} = 2(-i)^{n+1} \sqrt{\frac{2n+1}{2} \frac{(n-1)!}{(n+1)!} \times \frac{2}{n(n+1)}} c_{k,n} \\ = A(n) c_{k,n} \end{aligned} \tag{3.9}$$

using (1.19) and (1.20). And it can be immediately deduced that

$$\begin{aligned} \sum_{n=1}^{P} c\left(\frac{-i^n}{2}\sqrt{2n+1}\right)(\vec{K}_{11n} - \vec{K}_{1,-1,n} + \vec{K}_{21n} + \vec{K}_{2,-1,n}) \\ = \vec{f}(\theta,\phi) \sum_{n=1}^{P} C_{n,P} cos^{n-1}\theta \end{aligned} \tag{3.10}$$

Denoting

$$C_{n,P} = \sum_{k=n}^{P} \left(\frac{-i^k}{2}\sqrt{2k+1}\right) c'_{n,k} \tag{3.11}$$

These optimal $C_{j,P}$ coefficients can then be matched with the B_j of (3.5), adjusting the excitation coefficients α_p by solving a simple linear system of P equations with P unknowns. This system can be written in the matricial form $\mathbf{AX} = \mathbf{B}$, with

$$\mathbf{A} = \begin{bmatrix} 1 & 1 & \cdots & 1 \\ 0 & -ikd & \cdots & -(P-1)ikd \\ \vdots & \vdots & \ddots & \vdots \\ 0 & \frac{(-ikd)^{P-1}}{(P-1)!} & \cdots & \frac{(-(P-1)ikd)^{P-1}}{(P-1)!} \end{bmatrix}, \tag{3.12}$$

$$\mathbf{X} = \begin{bmatrix} \alpha_1 \\ \vdots \\ \alpha_P \end{bmatrix} \tag{3.13}$$

and

$$\mathbf{B} = \begin{bmatrix} C_{1,P} \\ \vdots \\ C_{P,P} \end{bmatrix} \tag{3.14}$$

General expression for the $c_{k,n}$ are derived in Appendix A.1.

Hence, there is a set of α_p coefficients such that the SWE of the array is the one that maximizes the directivity in the ($\theta = 0, \phi = 0$) direction, when the inter-element spacing d tends to zero.

(A)

(B)

FIGURE 3.1: SWE of a Huygens source polarized on the y axis (a) and a two-Huygens-source optimized array aligned along the z axis (b).The value of the radius of the circles is proportional to the square of the magnitude of the corresponding coefficient and the orientation of the displayed radius represents their phases.

TABLE 3.1: Approximated excitation coefficients of two and three-Huygens-source arrays.

P	$\alpha_{1,P}$	$\alpha_{2,P}$	$\alpha_{3,P}$
2	$-5i - kd$	$5i$	
3	$-14 + 6ikd - 2(kd)^2$	$14 + 4ikd$	$-7 + ikd$

Performing this analysis allowed the computation of analytic excitation coefficients for any given number of elements, as a function of inter-element spacing, as displayed in table 3.1 for up to four elements. These values were however computed in the hypothesis that the inter-element spacing d tends to zero. They are thus irrelevant when d is too large and the methods presented in 2.2 are to be used in general cases.

The same kind of study can be applied to a dipole array, to determine its SWE when its directivity is maximized.

3.1.2 Dipole-based arrays

The radiated far field pattern of an electric dipole oriented on the y axis is

$$\vec{f}_d(\theta,\phi) = cos\theta sin\phi\vec{e}_\theta + cos\phi\vec{e}_\phi \tag{3.15}$$

The array factor when the inter-element spacing d is in the vicinity of zero can still be expressed by (3.3). However, because of the $cos\theta$ on the $\vec{e}_\theta$ component, an asymmetry appears between the two components of the far field pattern:

$$\vec{F}(\theta,\phi) \sim \sum_{k=1}^{P} B_k cos^{k-1}[cos\theta sin\phi\vec{e}_\theta + cos\phi\vec{e}_\phi] \tag{3.16}$$

with B_k defined in (3.5).

For an array of P dipoles, the modal distribution would then be at best of the form (cf. Appendix A.2):

$$\vec{f}_d(\theta,\phi)\sum_{k=1}^{P} B_k cos^{k-1} = \sum_{n=1}^{P-1} T_n^{TE}(\vec{K}_{11n} - \vec{K}_{1,-1,n}) + \sum_{n=1}^{P} T_n^{TM}(\vec{K}_{21n} + \vec{K}_{2,-1,n}) \tag{3.17}$$

The maximum directivity of this distribution can also be given by Cauchy-Schwarz's inequality (cf. equations (2.2) and (2.5)):

$$
\begin{aligned}
D_{max}(\theta,\phi) &= \sum_{smn} |\vec{K}_{smn}(\theta,\phi).\vec{y}^{*}|^2 \\
D_{max}(0,0) &= \sum_{n=1}^{P-1} \left\{ |\vec{K}_{11n}(0,0)|^2 + |\vec{K}_{1-1n}(0,0)|^2 \right\} + |\vec{K}_{21P}(0,0).\vec{y}^{*}|^2 + |\vec{K}_{2,-1,P}(0,0).\vec{y}^{*}|^2
\end{aligned}
\tag{3.18}
$$

$$
\begin{aligned}
D_{max}(0,0) &= \sum_{n=1}^{P-1} (2n+1) + \frac{2P+1}{2} \\
D_{max}(0,0) &= P^2 + P - \frac{1}{2}
\end{aligned}
\tag{3.19}
$$

Taking $T_n^{TM} = T_n^{TE} = \frac{-j^{n+1}}{2}\sqrt{2n+1}$. Note that this directivity cannot exactly be reached by a P-dipole array as there are $2P-1$ independent mode coefficients to match correctly for only P excitation coefficients. This is then an optimization problem to solve. It is however to be noted that an array of P electric and $P-1$ magnetic dipoles (or inversely) does show a directivity that tends to $P^2 + P - \frac{1}{2}$, when properly feeding the $2P-1$ ports. The directivities as a function of spacing of such arrays are displayed in Figure 3.2. This type of arrays then seem to show little interest compared to P-dipole arrays as the increase in directivity is low.

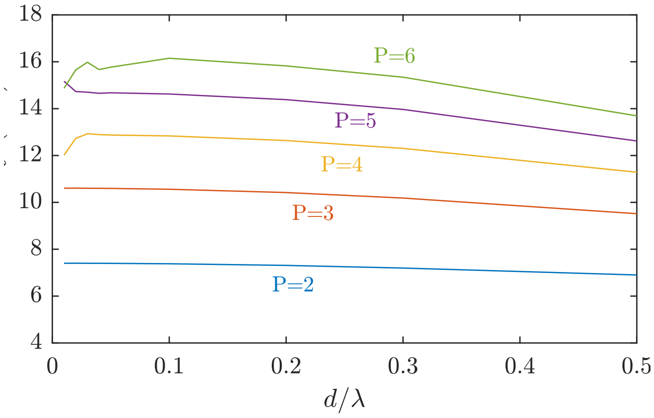

FIGURE 3.2: Directivity as a function of spacing of arrays of P electric and $P-1$ magnetic dipoles.

The example of the modes radiated by a two-dipole optimized array is displayed in Fig. 3.3. The modes of a magnetic dipole are obtained by swapping the TE and TM modes of the ones of an electrical dipole, so this result can be applied to arrays of both kind. The exact solution for this directivity optimization of a dipole-based arrays is demonstrated for the case of two elements in section 3.1.3.

(A)

(B)

FIGURE 3.3: SWE of an electric dipole oriented on the y axis (a) and a two-dipole optimized array aligned along the z axis (b).

3.1.3 Exact SWE of a two-dipole end-fire array optimized for directivity

Let us introduce the denotations

$$\vec{K}_{1n} = \vec{K}_{11n} - \vec{K}_{1,-1,n} \tag{3.20}$$

and

$$\vec{K}_{2n} = \vec{K}_{21n} + \vec{K}_{2,-1,n} \tag{3.21}$$

Then, from (1.19) and (1.20),

$$\vec{K}_{11} = -\sqrt{3}(sin\phi\vec{e}_\theta + cos\theta cos\phi\vec{e}_\phi) \tag{3.22}$$

$$\vec{K}_{21} = -\sqrt{3}(cos\theta sin\phi\vec{e}_\theta + cos\phi\vec{e}_\phi) \tag{3.23}$$

and

$$\vec{K}_{22} = j\sqrt{5}((2cos^2\theta - 1)sin\phi\vec{e}_\theta + cos\theta cos\phi\vec{e}_\phi) \tag{3.24}$$

Thus,

$$cos\theta\vec{K}_{21} = \frac{-i\sqrt{3}}{2\sqrt{5}}\vec{K}_{22} + \frac{\vec{K}_{11}}{2} \tag{3.25}$$

Then, taking (3.3) for $P = 2$ dipoles,

$$\begin{aligned}\lim_{d\to 0}\vec{F}(\theta,\phi) &= \vec{K}_{21}(\alpha_1+\alpha_2-ikd\alpha_2 cos\theta)\\ &= (\alpha_1+\alpha_2)\vec{K}_{21}-\frac{kd\alpha_2\sqrt{3}}{2\sqrt{5}}\vec{K}_{22}-\frac{ikd\alpha_2}{2}\vec{K}_{11}\end{aligned} \tag{3.26}$$

According to (3.17), the spherical wave distribution that would maximize directivity with these modes would be

$$\lim_{d\to 0}\vec{F}(\theta,\phi) = T_1(\vec{K}_{11}+\vec{K}_{21})+T_2 \tag{3.27}$$

with $T_n = -\frac{(-i)^n}{2}\sqrt{2n+1}$. The system to optimize is then $\mathbf{AX}\approx\mathbf{B}$ with

$$\mathbf{A} = \begin{bmatrix} 1 & 1 \\ 0 & -\frac{ikd}{2} \\ 0 & \frac{-\sqrt{3}kd}{2\sqrt{5}} \end{bmatrix} \tag{3.28}$$

$$\mathbf{X} = \begin{bmatrix} \alpha_1 \\ \alpha_2 \end{bmatrix} \tag{3.29}$$

and

$$\mathbf{B} = \begin{bmatrix} \frac{i\sqrt{3}}{2} \\ \frac{i\sqrt{3}}{2} \\ \frac{\sqrt{5}}{2} \end{bmatrix} \tag{3.30}$$

The optimization of this system gives

$$\alpha_1 = \frac{1}{2}-\frac{5i}{4kd} \tag{3.31}$$

$$\alpha_2 = \frac{5i}{4kd} \tag{3.32}$$

The exact optimized spherical wave distribution when d tends to zero is then

$$\lim_{d\to 0}\vec{F}(\theta,\phi) = T_1(\frac{5}{4}\vec{K}_{11}+\vec{K}_{21})+\frac{3}{4}T_2 \tag{3.33}$$

which provides the exact directivity of $D = 5.25$ or $7.2dBi$, from (2.1), which is inferior to $2^2+2-\frac{1}{2} = 5.5 = 7,4dBi$. A more general analysis of the two-dipole-end-fire array optimized for directivity was presented in [54], demonstrating similar results when d tends to zero.

The presented analysis showed how end-fire arrays with independent excitation coefficients could radiate spherical waves that optimize directivity, when the inter-element spacing tends to zero. This kind of array is then well suited for the design of superdirective antennas, meaning that they exceed the 'normal' limit [55]. These methods rely however on the approximation that d is close enough to zero so that the power of Spherical Waves of order greater than P can be neglected. The directivity limits having determined, the problem of gain limitations for lossy antennas is reviewed in the next sections.

3.2 Gain limitations

The notion of superdirectivity having been defined as well as theoretical methods to design superdirective arrays, the information of gain, taking into account radiation losses remains to be addressed. This section thus deals with the physical requirements on an antenna design to reach a given gain. In section 2.1.2, qualitative comments based on Harrington's definition of 'normal' directivity were made stating that decreasing a radiator's size without decreasing its directivity requires the use of higher excitation currents to be applied on the antenna. A more quantitative development of that statement was also made by the same author in [41]. It introduced the dissipation factor which is the ratio of dissipated power through heat losses (P_{diss}) to radiated power (P_{rad}), for each spherical wave. It is denoted

$$Df = \frac{P_{diss}}{P_{rad}} \tag{3.34}$$

This can be calculated considering the equivalent waveguide model for each spherical wave introduced in section 2.1.3. This model provides each spherical wave with an equivalent characteristic impedance.

As these impedances describe the radiated waves, their real part are equivalent to the radiation resistance of the wave. They only depend on the order n and on the antenna radius a. The power dissipated can then be considered as the ohmic losses generated by the current which is required for the antenna to radiate the specified spherical wave. This would be represented by an equivalent loss resistance. According to Harrington, the equivalent loss resistance is given by the real part of the equivalent impedance calculated within the minimum sphere that encloses the antenna. This impedance is denoted $Z_{sn}^{-} = Z_{sn}(kr)$ with $r < a$ and $Z_{sn}(ka)$ defined in section 2.1.3 by (2.24) and (2.25). As shown, in section 2.1.3, these values do not depend on the m index. The dissipation factor of a spherical wave then depend on its order n and differ if the wave is TE ($s = 1$) or TM ($s = 2$), as

$$Df_{sn}(ka) = \frac{Re(Z_{sn}^{-})}{Re(Z_{sn}^{+})} \tag{3.35}$$

where $Z_{sn}^{+} = Z_{sn}(kr)$ with $r > a$. This impedance is equal to

$$Z_{sn}^{+} = Z_{sn}(ka) \tag{3.36}$$

To provide a simple ideal loss resistance, Harrington chose the model of a radiating metallic sphere. It is suggested that this model gives a maximum possible gain as it is an antenna that utilizes the maximum possible space in the sphere of radius a. Hence, Z^{-}_{sn} can be calculated as

$$\begin{aligned} Z^{-}_{sn}(kr) &= \frac{\eta_c}{\eta} Z_{sn}(kr),\ r < a \\ Z^{-}_{sn}(kr) &\approx \frac{\eta_c}{\eta} \end{aligned} \tag{3.37}$$

where $\eta_c \approx (1+i)(\sqrt{\frac{\omega\mu}{2\sigma}})$ is the intrinsic impedance of the metal, with μ the permeability of vacuum. The ratio $\frac{\eta_c}{\eta}$ as the regions inside and outside the sphere are differentiated by their respective characteristic impedance (η_c inside the sphere and η outside), in this equivalent waveguide model. Note that this equivalent loss resistance is dimensionless and that it is equal to the real part of the intrinsic impedance of the metallic conductor relatively to the wave impedance. This equivalent resistance is denoted r_{loss} in the following, as

$$r_{loss} = Re(Z^{-}_{sn}) \tag{3.38}$$

Note that a more recent work on the maximum gain was also proposed in [53] where the effective permittivity of the antenna is taken into account as well as conductivity, for a more general case.

For a given antenna size defined by its radius a, the dissipation factor of a radiated spherical mode is then

$$Df_{sn}(ka) = \frac{r_{loss}}{Re(Z_{sn}(ka))} \tag{3.39}$$

The antenna gain can be defined as the directivity multiplied by its radiation efficiency

$$eff_{rad} = \frac{P_{rad}}{P_{rad} + P_{diss}} \tag{3.40}$$

Knowing that the global dissipaiton factor can be derived from the radiated power (P^{rad}_{smn}) and dissipation factor (Df_{sn}) of each Spherical Waves, as

$$\begin{aligned} P_{diss} &= \sum_{smn} P^{rad}_{smn} Df_{sn} \\ P_{diss} &= \frac{1}{2} \sum_{smn} Df_{sn} |T_{smn}|^2 \end{aligned} \tag{3.41}$$

Note that $\sum_{smn}$ refers to the summation on all modes of order up to N, as described in equation (1.15). However, in this analysis, no assumption is made on the order of the waves radiated and N is then replaced by ∞. The radiation efficiency of a Spherical Wave can also be defined from its dissipation factor Df_{sn} as

$$eff_{sn} = \frac{1}{1 + Df_{sn}} \tag{3.42}$$

Then, from (1.26), the gain can be expressed as

$$G(\theta,\phi) = \frac{|\sum_{smn} T_{smn} \vec{K}_{smn}(\theta,\phi)|^2}{\sum_{smn}(1 + Df_{sn}(ka))|T_{smn}|^2} \tag{3.43}$$

Let us introduce the denotation $T'_{smn} = \sqrt{1 + Df_{sn}} T_{smn}$. Then the gain becomes

$$G(\theta,\phi) = \frac{|\sum_{smn} T'_{smn} \frac{\vec{K}_{smn}(\theta,\phi)}{\sqrt{1+Df_{sn}}}|^2}{\sum_{smn}|T'_{smn}|^2} \tag{3.44}$$

The Cauchy-Schwarz's inequality can be used again, as seen in (2.5), to find the maximum gain

$$G_{max}(\theta,\phi) = \sum_{smn} \frac{|\vec{K}_{smn}(\theta,\phi).\vec{i}^*_{co}|^2}{1 + Df_{sn}(ka)} \tag{3.45}$$

$$G_{max}(\theta,\phi) = \sum_{mn} |\vec{K}_{1mn}(\theta,\phi)|^2 \frac{eff_{1n} + eff_{2n}}{2} \tag{3.46}$$

The condition of equality being

$$T'_{smn} = cte \cdot \frac{\vec{K}_{smn}(\theta,\phi).\vec{i}^*_{co}}{\sqrt{1 + Df_{sn}(ka)}}^* \tag{3.47}$$

so

$$T_{smn} = cte \cdot \frac{\vec{K}_{smn}(\theta,\phi).\vec{i}^*_{co}}{1 + Df_{sn}(ka)}^* \tag{3.48}$$

with *cte* an arbitrary real constant. According to [53] and [41], the modes excitation have to be balanced in TE and TM waves, as in section 2.1.1. This gives [53]

$$G_{max} = \sum_{n=1}^{\infty} (2n+1) \frac{eff_{1n} + eff_{2n}}{2} \tag{3.49}$$

As the eff_{sn} depend on ka, the maximum gain now also depends on it even without limiting the mode order n. This can be shown by plotting the radiation efficiency associated to each wave as a function of ka and n, cf. Figure 3.4. This curves show that, as qualitatively predicted in [3] with the normal limit, when the ka of an antenna is lower than a certain 'cut-off' value, the radiation efficiency of the spherical waves drops drastically. This 'cut-off' value depends on the wave order n but also on the loss resistance as if the loss resistance is null the efficiencies are always equal to one. According to Figure 3.4, the efficiencies began to drop for a ka close to $ka = n$, with a normalized loss resistance value of $r_{loss} = 0.02$.

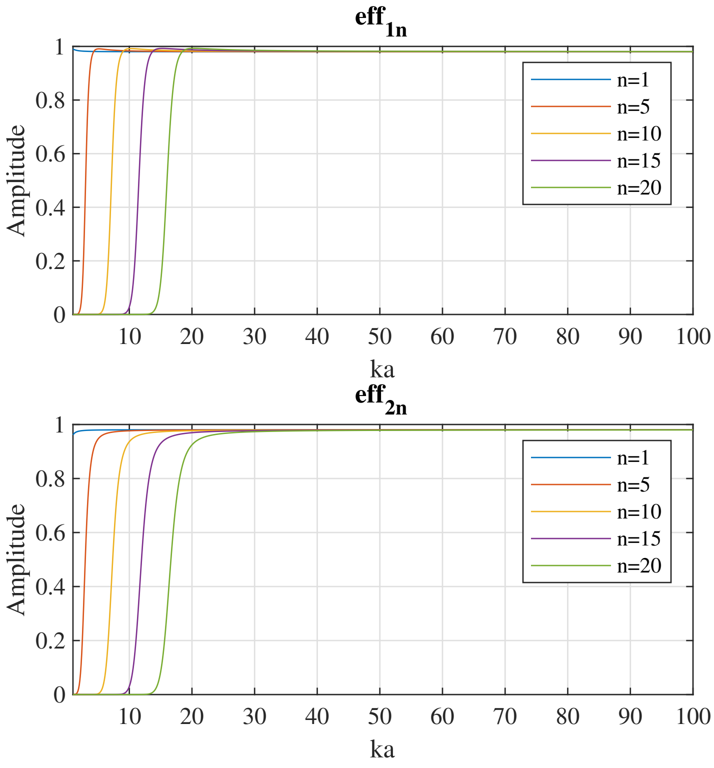

FIGURE 3.4: Radiation efficiency eff_{sn} associated to TE ($s = 1$) and TM($s = 2$) spherical waves of order n, for $r_{loss} = 0.02$.

For a given loss resistance, the maximum gain can then be calculated as a function of ka. Figure 3.5 displays this gain for various loss resistances and compared to the normal limit. This shows a similar asymptotic behavior with an offset that varies according to the loss resistance. Also, the gain loss is even quicker than the normal limit when ka tends to zero, for any value of loss resistance. As it was described in section 2.1, the normal limit considers a maximum number order of spherical mode that can be used for a given radius a which is not the case for these newly calculated gain limits. Here it can be seen that the normal limit can be exceeded when the ohmic losses of the antenna are sufficiently low.

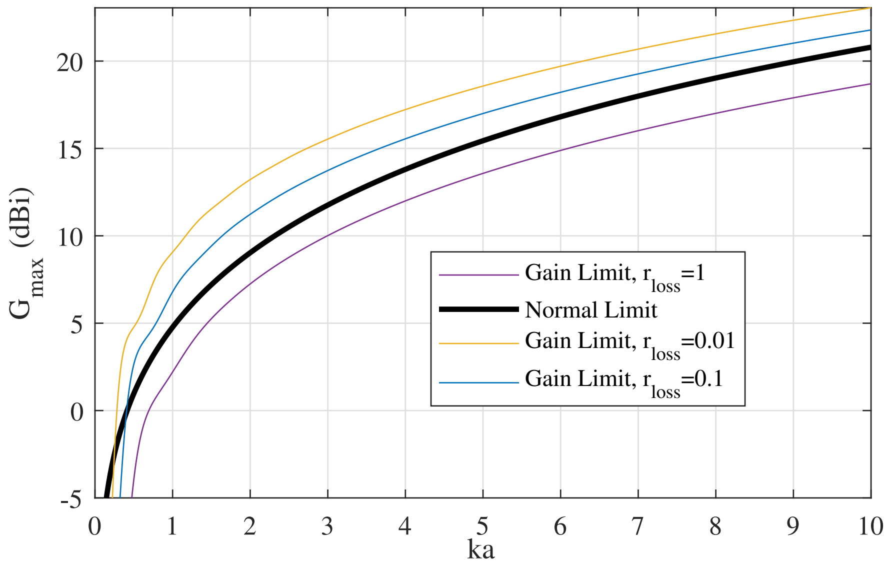

FIGURE 3.5: Limits of gain for various relative loss resistances.

The next section then deals with the gain limitations of superdirective arrays through classical array theory.

3.3 Efficiency index

Increasing directivity without changing the radiator size leads to a decrease of radiation efficiency for a lossy antenna. This effect can also be quantified by array theory, according to [13]. The gain of a lossy array antenna can be expressed as

$$G = \frac{r^2|\vec{E}(\theta,\phi)|^2}{2\eta(P_{rad}+P_{loss})} \tag{3.50}$$

For the case of an array antenna, the heat losses can be considered to be only due to the loss resistances of each element [13]. In a case of arrays of identical elements, all antennas have equal loss resistances R_{loss}, and the heat losses are then

$$P_{loss} = \frac{1}{2}R_{loss}\sum_{p=1}^{P}|I_p|^2 \tag{3.51}$$

where I_p is the maximum value of the current running through the p-th element. The $\frac{1}{2}$ factor comes from time-averaging the sinusoidal currents.

Furthermore, the radiated power of a P-element array antenna can also be expressed as ([13])

$$P_{rad} = \frac{1}{2}\sum_{m=1}^{P}\sum_{p=1}^{P}I_m I_p^* R_{mp} \tag{3.52}$$

where R_{mp} is the mutual resistance between the elements m and p if $m \neq p$ and R_{mm} is the intrinsic radiation resistance of the m^{th} element. Attention is drawn to the fact that the excitation coefficients A_p are proportional to the I_p currents. Thus, as the far-field pattern f is proportional to the electric radiated field E, the radiated power is proportional to the denominator of 2.43. More explicitly

$$\sum_{m=1}^{P} \sum_{p=1}^{P} I_p I_m^* R_{mp} = \gamma \sum_{m=1}^{P} \sum_{p=1}^{P} a_p a_m^* h_{mp} \tag{3.53}$$

This is true for any values for the a_p coefficients, so that

$$R_{mp} = \gamma' h_{mp} \tag{3.54}$$

with γ and γ' real constants. The h_{mp} can then be considered as normalized resistances. Let the normalized loss resistance of element p be $r_{loss,p} = \frac{R_{loss,p}}{R_{pp}}$, then let $h_{loss} = \frac{R_{loss,p}}{\gamma'} = r_{loss,p} h_{pp}$. Then

$$\begin{aligned} G &= \frac{|F^2|}{\sum_{m=1}^{P} \sum_{p=1}^{P} a_p a_m^* h_{mp} + \sum_{p=1}^{P} |a_p|^2 h_{loss,p}} \\ &= \frac{|F^2|}{\sum_{m=1}^{P} \sum_{p=1}^{P} a_p a_m^* h_{mp} (1 + \delta_{mp} r_{loss,p})} \end{aligned} \tag{3.55}$$

where δ_{mp} is the Kronecker number.

The gain can also be calculated from the directivity, as:

$$\frac{1}{G} = \frac{1}{D} + \frac{\sum_{p=1}^{P} h_{pp} r_{loss,p}}{|F|^2} \tag{3.56}$$

Taking that the array elements are identical, $r_{loss,p} = r_{loss}$ and $h_{pp} = h_{11}$, so that:

$$\frac{1}{G} = \frac{1}{D} + \frac{h_{11} r_{loss}}{J} \tag{3.57}$$

where J is the efficiency index as defined in [13]. Hence,

$$J = \frac{|\vec{F}|^2}{\sum_{p=1}^{P} |a_p|^2} \tag{3.58}$$

Note that the r_{loss} defined here is a particular case of the one defined in section 3.2 as it is equal to the ratio of ohmic loss to radiated power. The notation is then the same in the following, to allow the comparison between array gain limit and the general gain limit taken from the ideal model of the metallic sphere from [41] detailed in section 3.2.

One can notice from (2.45) that h_{pp} is also equal to the inverse of the directivity of the unitary element p, so 1 for an isotropic source, $\frac{2}{3}$ for a dipole and 3 for a Huygens source. The gain obtained when maximizing directivity, taking into account the resistance losses are displayed t in Figures 3.7, 3.8, 3.9 and 3.10.

3.4 Sensitivity factor

This section deals with the impact of random errors that occur during the realization of superdirective arrays. These random variations can appear both in the excitation coefficients and the inter-element spacing. It has been shown in [12] that when random variations are introduced in the excitation coefficients and the inter-element spacing, the mean expected value of the directivity could be calculated as

$$\langle D \rangle = \frac{|\vec{F}|^2 + \Delta^2 h_{11} \sum_{p=1}^{P} |a_p|^2}{p_{rad} + \Delta^2 h_{11} \sum_{p=1}^{P} |a_p|^2} \tag{3.59}$$

for array of identical elements. $p_{rad} = \sum_{m=1}^{P} \sum_{p=1}^{P} a_p a_m^* h_{mp}$ is a normalized radiated power. Δ^2 is the aggregated variance of the random errors added on excitation coefficients and element placement. More precisely, $\Delta^2 = \epsilon^2 + \delta^2$ with ϵ is standard deviation made on each excitation coefficient, and δ is linked to the error made on inter-element spacing. Hence the error on the excitation coefficient a_p is denoted α_p such as $a_p = a_{0p} + \alpha_p$ with a_{0p} the optimal coefficient. Moreover

$$\langle |\alpha_p|^2 \rangle = \epsilon^2 |a_p|^2, p = 1, 2, ..., P. \tag{3.60}$$

The definition of δ made by [12] is not explicited here as it will not be used in the following.

Now (3.59) can be rearranged as

$$\langle D \rangle = \frac{1 + \frac{\Delta^2 \sum_{p=1}^{P} |a_p|^2}{|\vec{F}|^2}}{\frac{p_{rad}}{|\vec{F}|^2} + \frac{\Delta^2 \sum_{p=1}^{P} |a_p|^2}{|\vec{F}|^2}} \tag{3.61}$$

The sensitivity factor K was defined in [12] as

$$K = \frac{\sum_{p=1}^{P} |a_p|^2}{|\vec{F}|^2} \tag{3.62}$$

$$K = \frac{1}{J} \tag{3.63}$$

so that

$$\langle D \rangle = \frac{1 + \Delta^2 K}{\frac{1}{D} + \Delta^2 K}. \tag{3.64}$$

In the case of $\Delta^2 K << 1$, (3.64) can be approximated as

$$\begin{aligned} \frac{1}{\langle D \rangle} &= \frac{1}{D} + \Delta^2 h_{11} K \\ \frac{1}{\langle D \rangle} &= \frac{1}{D} + \frac{\Delta^2 h_{11}}{J} \end{aligned} \tag{3.65}$$

which is the same equation as (3.58) replacing G with $\langle D \rangle$ and r_{loss} with Δ^2. This means that the sensitivity and efficiency of this kind of array have a similar behavior.

In the case of superdirective arrays, excitation coefficients a_p and maximum directivity D can be calculated analytically with the formulas presented in [13] and [42] for example. It is then possible to know precisely the theoretical expected directivity when introducing random variations in these arrays.

3.5 Gain maximization

In Section 2.2.1, it has been shown that the directivity (2.40) is maximized solving the linear equation system in (2.48). The same formulation can be used to maximize the gain (3.50), by multiplying in (2.48) the diagonal terms h_{pp} (intrinsic normalized resistances) by $(1 + r_{loss,p})$ [13]. This simple modification of the optimization procedure is shown in Figure 3.6.

The gain that can be reached with this optimization is also shown in Figures 3.7, 3.8, 3.9 and 3.10 as a function of spacing. As it was shown in section 3.4 that sensitivity and efficiency of superdirective arrays have a similar behavior, meaning that considering the standard deviation on excitation coefficient instead of the normalized loss resistance of the unitary elements, the calculated gain becomes the expected directivity. Hence, maximizing the gain also maximizes the expected directivity, considering a variance on excitation coefficients of $\Delta^2 = r_{loss}$. Displays of the excitation coefficients provided for gain optimization are shown in Appendix C.

To confirm the effectiveness of those calculations, full-wave simulation of half-wave dipole arrays were also conducted. The excitation coefficients of those arrays was optimized alternatively for maximum directivity and gain. The results presented in Figures 3.12 and 3.11 are compared to the theoretical curves. The resistance losses of the half-wave dipoles was calculated using the radiation efficiency computed by the simulation software for each feeding port. The formula used is

$$r_{loss,p} = \frac{1 - eff_p}{eff_p} \tag{3.66}$$

This formula takes into account the differences of radiation efficiency between elements, as they suffer different near-field coupling with the array. However, the theoretical loss resistances used in the analytic model were calculated from [35]:

$$R_{loss} = \frac{l}{4\pi r}\sqrt{\frac{2}{\omega\mu_0\sigma}} \tag{3.67}$$

with μ_0 the permeability of vacuum, and

$$R_{rad} \approx R_{in} \approx 24.7(kl/2)^{2.5} \tag{3.68}$$

Hence, knowing the conductivity of the copper $\sigma = 5.8.10^7 S.m^{-1}$, the length, $l = 0.47\lambda$, and radius $r = 0.002\lambda$, of the dipoles, it is found $R_{loss} \approx 0.11\Omega$ and $R_{rad} \approx 59\Omega$ Thus, $r_{loss} = \frac{R_{loss}}{R_{rad}} = 0.2\%$ and the corresponding radiation efficiency is

$$\eta = \frac{R_{rad}}{R_{rad} + R_{loss}} \approx 99.8\%. \tag{3.69}$$

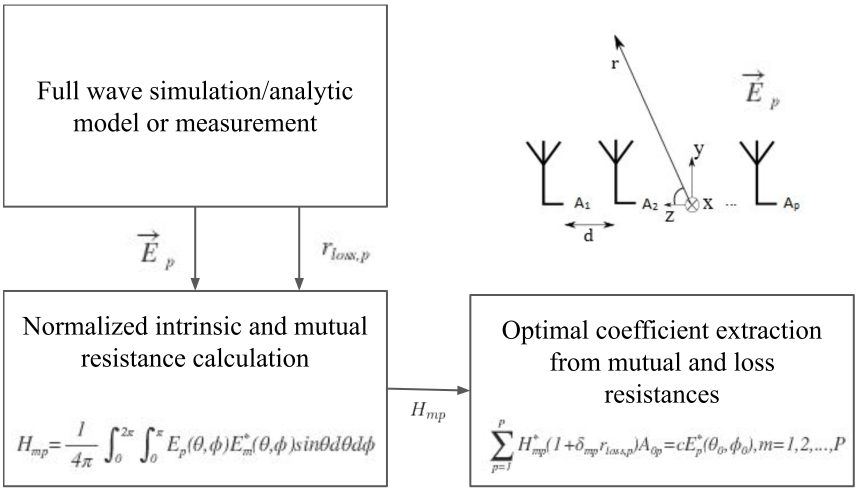

FIGURE 3.6: Optimization procedure for gain maximization.

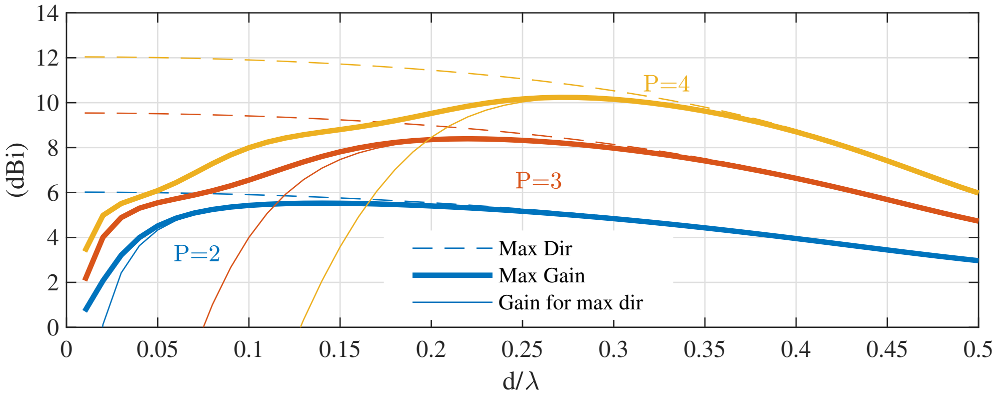

FIGURE 3.7: Theoretical directivity and gain as a function of the inter-element spacing d, for arrays of P isotropic sources. The loss resistance considered is $r_{loss} = 0.01$.

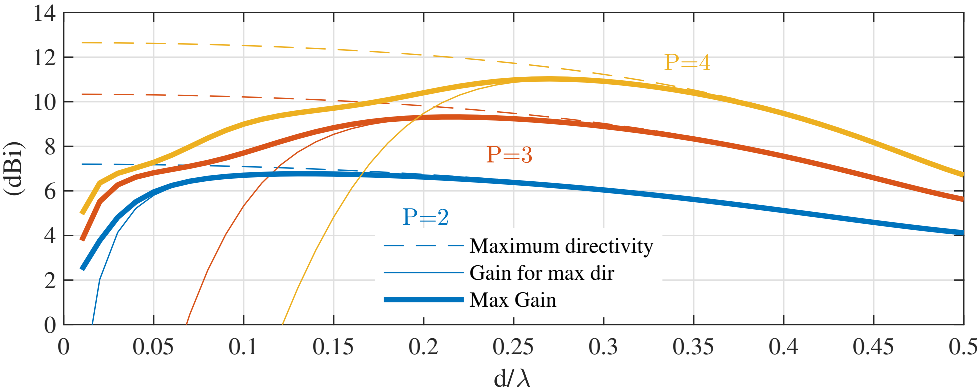

FIGURE 3.8: Theoretical directivity and gain as a function of the inter-element spacing d, for P infinitesimal-dipole arrays. The loss resistance considered is $r_{loss} = 0.01$.

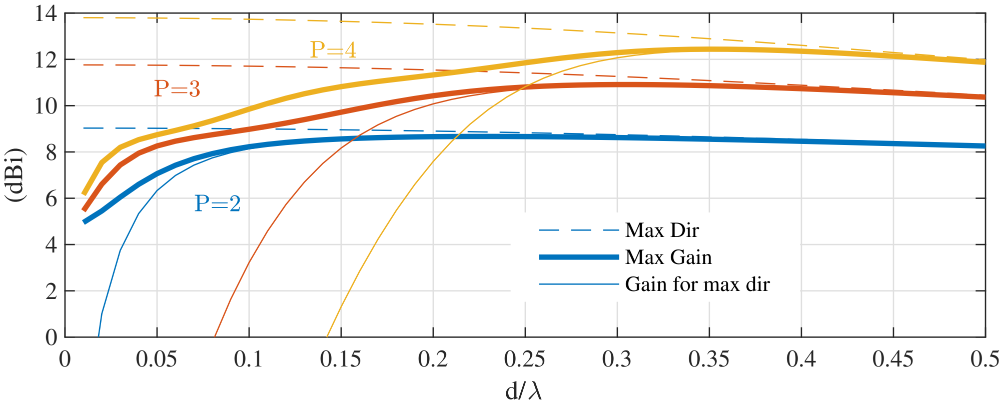

FIGURE 3.9: Theoretical directivity and gain as a function of the inter-element spacing d, for P-Huygens-source arrays. The loss resistance considered is $r_{loss} = 0.01$.

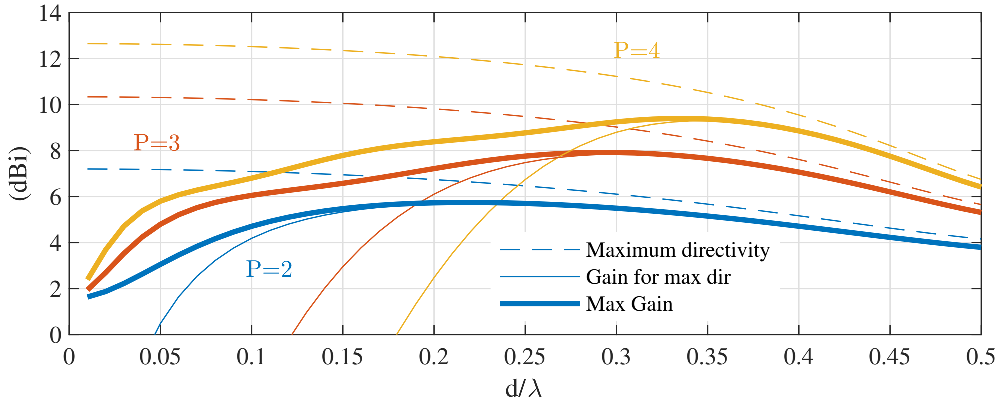

FIGURE 3.10: Theoretical directivity and gain as a function of the inter-element spacing d, for arrays of P infinitesimal dipoles. The loss resistance considered is $r_{loss} = 0.1$.

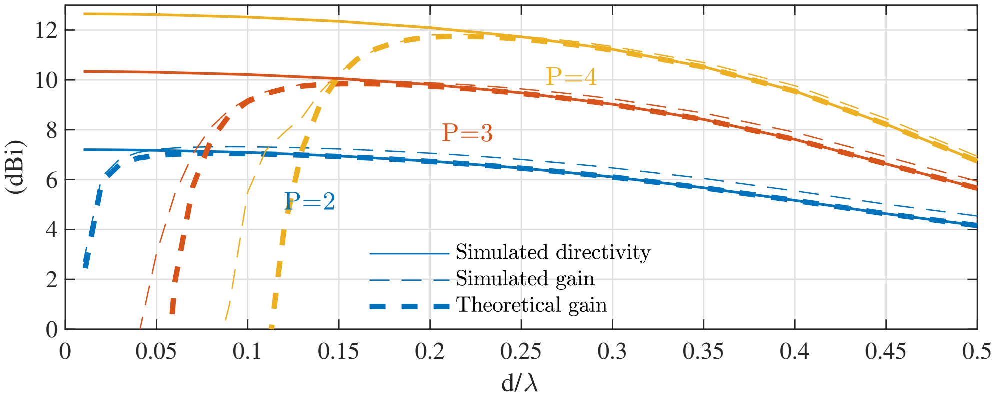

FIGURE 3.11: Simulated directivity and gain as a function of the inter-element spacing d, for arrays of P half-wave dipoles optimized for directivity.

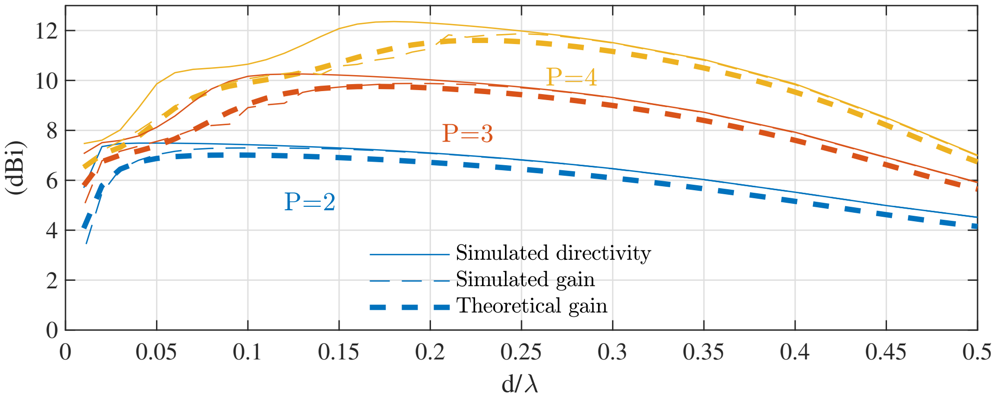

FIGURE 3.12: Simulated directivity and gain as a function of the inter-element spacing d, for arrays of P half-wave dipoles optimized for maximum gain.

Hence, the results of Figures 3.12 and 3.11 show a good agreement between simulation and full analytic calculations. The interest of maximizing gain over directivity also seems clearly visible for arrays of three dipoles or more.

For the example of dipole-based arrays with an inter-element spacing of 0.1λ, the maximum directivity and gain results are displayed in table 3.2. This highlighs the gain differences considering unitary radiation efficiencies of 98 % or 90 %, mostly when the directivity is maximized.

Moreover, this curves can be compared to the limit of gain for lossy antennas calculated in section 3.2. The size of the unitary elements must then be considered to derive the ka for antenna arrays. In case of a P-dipole array, neglecting the dipoles' radius, the antenna radius a is then

$$a = \frac{\sqrt{l^2 + [(P-1)d]^2}}{2} \tag{3.70}$$

TABLE 3.2: Simulated maximum directivities and gain of infinitesimal-dipole-based- (Inf dip.) and Halfwave-dipole-based-arrays (H-W dip.), for an inter-element spacing of 0.1λ. The gain are calculated for infinitesimal dipoles of radiation efficiencies of 98 % and 90 %. 'Max gain' indicates the maximization of gain and gain for dir. opt. is for the case of directivity maximization.

	Max directivity		Max gain .		Gain for dir. opt	
P	Inf. dip.	H-W dip.	$eff = 98\%$	$eff = 90\%$	$eff = 98\%$	$eff = 90\%$
2	7.20	7.43	6.70	4.71	6.70	4.19
3	10.34	10.54	7.70	6.05	5.33	-3.12
4	12.67	12.87	9.00	6.8	-4.83	-14.72

where l is the dipole's length (cf. Figure 5.5). Also, considering Huygens-source-based arrays, the same calculation can be used to find a, considering that the magnetic loops are small enough. Furthermore, the resistance loss to take for the dissipation factor is the loss resistance of the element of the arrays normalized by the radiation resistance of the mode of order $n = 1$ for a ka equal to the one of a single element of the array. Indeed, the dipole's radiation can be modeled by spherical waves of order $n = 1$, so its radiation resistance is equal to the equivalent radiation resistance of this mode order. Figures 3.13, 3.14 and 3.15 thus show results of theoretical directivities and gain as a function of ka, compared with the normal limit and gain limit for defined in section 3.2. Note that the gain limit is calculated for a maximum order $N = 4$ as only results for arrays of up to four elements are presented. The results are shown for loss resistances of $r_{loss} = 0.1$ and $r_{loss} = 0.01$ and dipole length of $l = 0.47\lambda$ and $l = 0.1\lambda$.

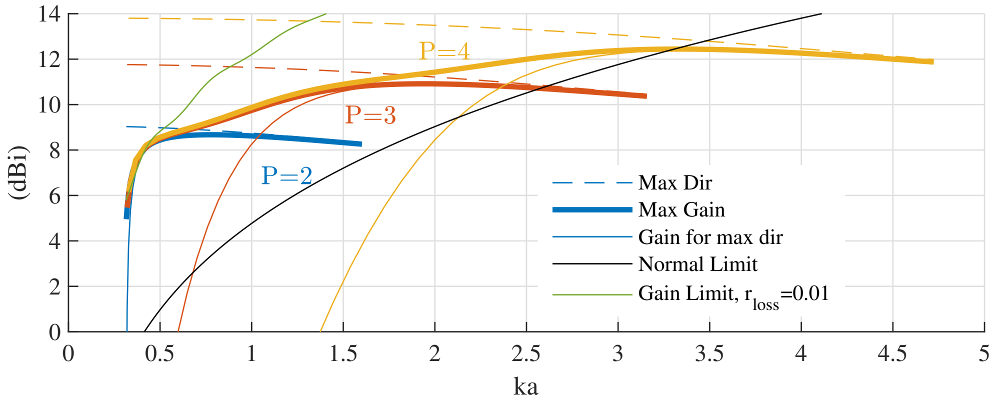

FIGURE 3.13: Directivity and gain as a function of ka, for arrays of P Huygens sources, with dipole length $l = 0.1\lambda$, for a normalized loss resistance $r_{loss} = 0.01$.

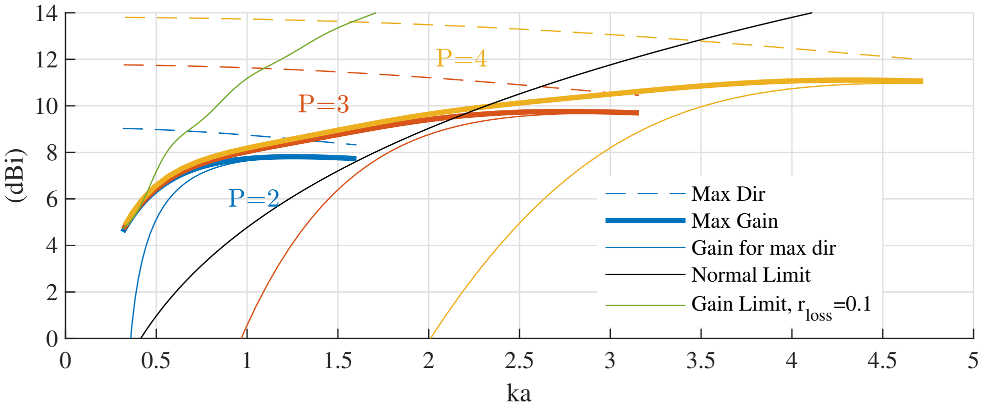

FIGURE 3.14: Directivity and gain as a function of ka, for arrays of P Huygens sources, with dipole length $l = 0.1\lambda$, for a normalized loss resistance $r_{loss} = 0.1$.

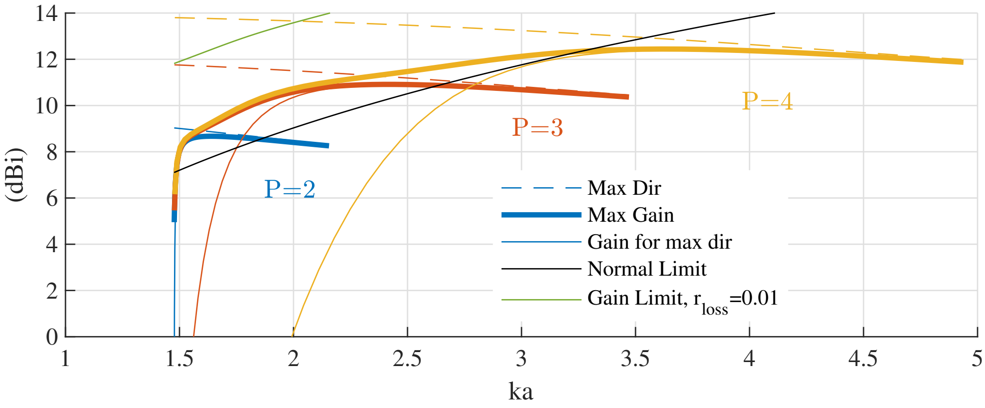

FIGURE 3.15: Directivity and gain as a function of ka, for arrays of P Huygens sources, with dipole length $l = 0.47\lambda$, for a normalized loss resistance $r_{loss} = 0.01$.

These curves show a gain limit that is close to the array gain when it is maximized and the inter-element spacing is very close to zero. The arrays' gain is far below when the inter-element spacing increases, as the ka increases rapidly. Moreover, it can be seen that the normal limit can be exceeded in term of gain but more easily with two- or three-Huygens-source arrays. Indeed, increasing the number of element increases the ka of the antenna without increasing maximum gain enough to follow the curve of the normal limit. This shows that end-fire compact arrays have their most interesting performances for a limited number of element. Other techniques for increasing gain are then to be considered when increasing the antenna size, such as aperture or broadside array antennas which tends to the normal directivity limit, as stated in [3]. Generally, a combination of broadside and end-fire arrays seem to be the architecture that would get the closest to the maximum gain limit.

3.6 Conclusions

The theoretical performance limitations of small directive antennas have been examined through the fundamental study of Spherical Wave Functions and with the more precise case of linear array antennas. It has indeed been shown in section 3.1 that linear end-fire arrays are naturally well suited for the design of superdirective antennas. However, the works on gain limitations first made from the Spherical Wave Function theory and then from array theory show that superdirective arrays coincide with the general theoretical limit for gain only for very close spacing and small total size. This case is thus limited to gain below the value of 10 dBi, for reasonable single element radiation efficiency such as 99% and small single dipole elements of length $l = 0.1\lambda$. The gain to expect remains however greater than the normal gain limit for up to four-element arrays and gain of about 12 dBi. The normal gain then is higher for larger antennas. The performances that would be reached with Huygens-source-based arrays are of course higher and the examination of the design of such antennas will be discussed in the next part of the thesis.

As this work is focused on the design of small superdirective antennas, the following is about the case of compact end-fire arrays, with the number limited to four, as the aim is to exceed the normal gain limit. The qualification 'small' does not then refers any of the electrically small antenna definitions. The design of the single elements of the arrays can however fall under these definitions. The next part will then be dedicated on the design of such antennas.

Chapter 4 is then a survey of the state of the art in term of superdirective antennas. This mostly deals with linear array antennas or antennas that can be considered as such. The design are also mainly based on dipoles or monopoles, but the design of Huygens sources is also investigated in the literature. The design method of parasitic element array is then detailed further, as it is chosen in this work. Chapter 5 is then a deeper analysis proposed for parasitic element arrays. The purpose is to look for ways to optimize the design regarding the requirement on parasitic loads. The need for resistive loads is indeed a problem that appears in the design of those arrays, even more problematic as their required value is negative. Design method that influence these values are thus examined. Finally, Chapter 6 presents the proposed design of some small superdirective arrays. Hence, small-dipole and halfwave-dipole-based arrays of up to four elements are designed and measured. Moreover, the design of Huygens-source-based arrays is also discussed and demonstrated through full-electromagnetic simulations. These particular design are however not measured as the expected performances are lower than the simpler dipole cases.

PART II: Practical Implementation of Superdirective and Supergain Arrays

Chapter 4

State of the Art of Superdirective Antennas

In this chapter, the state of the art of superdirective antenna practical design is reviewed.

According to the normal directivity limit described in section 2.1.2, any small dipole is a superdirective antenna as its directivity is greater to this limit. Note that a small antenna is here considered to be an antenna with dimensions such that its ka is inferior to one, according to the definition of [2]. This section will however consider antennas with greater directivities than the one of a single infinitesimal dipole and will mostly focus on the design of antenna arrays or combination of sources such as Huygens source designs.

These designs aim at performing the characteristics described in chapter 2 and 3 as they can mostly be modeled as equivalent dipole-based arrays or Huygens sources. The next sections review the different design methods presented in the literature. These designs are separated into three main groups, Huygens sources, loaded antennas and end-fire arrays. Note that the referencing work [56] that was noticeably used here also contains several other small antenna designs that were not considered as they have lesser directivities.

The section about end-fire arrays is then further detailed into various practical technologies proposed in the state of the art. These technologies include single element design and implementation methods to properly feed each element. The single element design is studied for radiation efficiency and impedance matching optimization. The different feeding techniques include direct feeding with power dividers, Yagi-like or parasitic-element arrays which use near-field coupling between element to adjust the excitation currents in each of them.

The designs of the state of the art that show the best performances as respect to directivity or gain for a given size, according to the ka parameter defined in Chapter 2 are summarized in the concluding part.

4.1 Huygens sources

The most directive theoretical single infinitesimal source is the Huygens source which has a directivity of 3 and is infinitesimal, as seen in section 3.1. The design of a cross electric and magnetic dipole with equal excitation in amplitude and phase is however a challenge. Several design methods were presented in the literature. In [57], a Huygens source is made by designing simultaneously an electric dipole and a magnetic loop which are both excited through near-field coupling with a feeding dipole. In other words, the current running through the radiating electric and magnetic dipoles is induced through the near-field generated by a small dipole antenna correctly placed between the two sources. This can be seen in Figure 4.3 (A) from the work of [28]. A well adjusted design creates an equi-phase and equi-amplitude excitation (considering electric and magnetic currents, cf. section 1.4.2) and therefore the cardioid-like radiation pattern. This type of design has also proven good radiation efficiency and possible 50Ω impedance matching [28]. Similar sources have been measured with this method in [58],

Another type of design is the one using two omega particles, as presented in [59] which are excited by two independent feeding lines.

Moreover, the authors of [30] use a radiating slot as a magnetic dipole and a properly placed excitation probe that feeds both the magnetic dipole and an electric dipole placed over the slot and perpendicular to its orientation. This kind of design offers a wide bandwidth and also a greater gain as it uses reflection over a large ground plane. The directivity reach is then close to 9 dBi which is the maximum directivity of a two-Huygens-source array. However, this antenna is radiating in the broadside direction (perpendicular to the ground plane) and thus cannot be used in a larger end-fire array configuration because of the required ground plane.

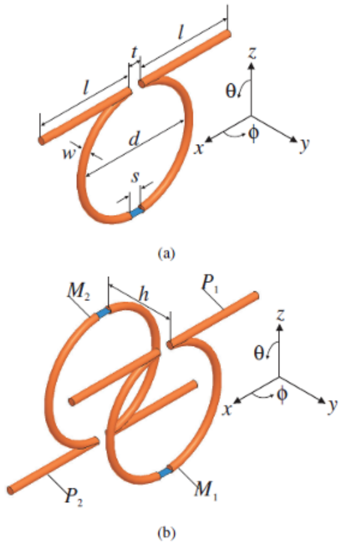

FIGURE 4.1: Huygens source design with two Omega particles as presented in [29]

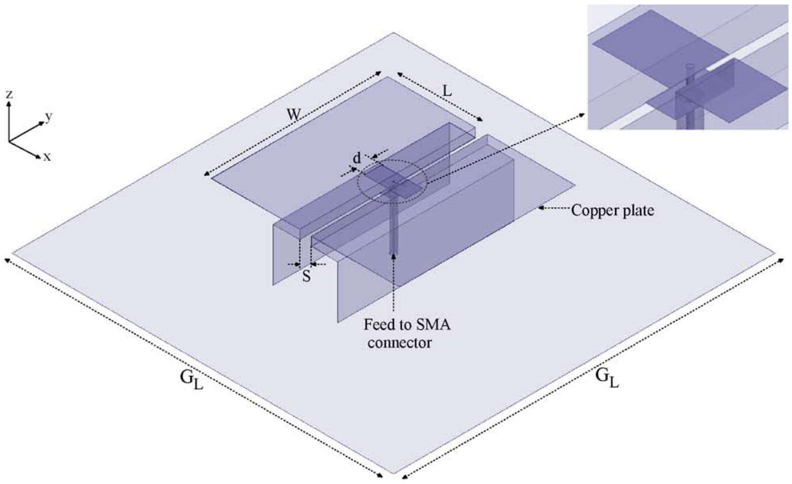

FIGURE 4.2: Huygens source design presented in [30]

One of the problems that occur when designing Huygens-source-based end-fire arrays is the size of the loops that constraint the inter-element spacing. Indeed, as the dipoles' orientation must be perpendicular to the array alignment, the plane that contains the loop must be aligned with the array elements. The space between sources thus cannot be below the length of the loops'radius. This difficulty was overcome in [60] with the design of a broadside radiating Huygens source. This was done with the use of a very narrow rectangular loop, as shown in Figure 4.3 (B). The maximum directivity is then in the $\vec{z}$ direction.

The fact that broadside radiating Huygens source could theoretically help create superdirective arrays was described in [27]. The realization of Huygens-source based arrays still remains a challenge that has not been met, according to [31]. The reasons given in [31] are high quality factor and poor impedance properties when attempting to design such arrays. More importantly, better performances seem to be achieved by electric- or magnetic-dipole-based arrays, which design is far simpler.

The feasibility of a Huygens-source-based superdirective array is explored further in Chapter 6.

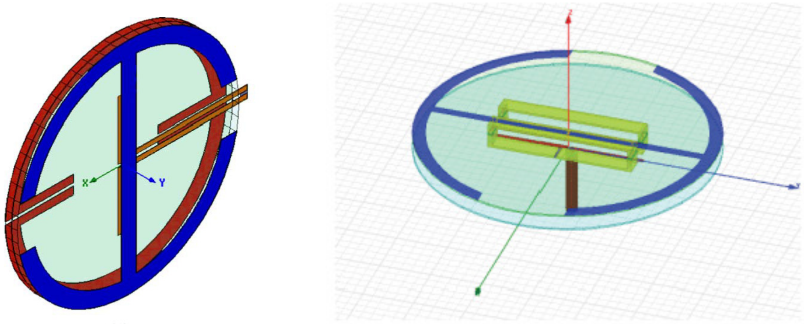

(A) (B)

FIGURE 4.3: End-fire (A) and broadside radiating (B) Huygens source design presented in [28] and [60], respectively

4.2 Loaded antennas

Loaded antennas are antennas that use impedance loads connected to them to modify their radiation pattern. It was shown in [61] that a cardioid like pattern could be obtained with a loop antenna loaded by a resistance placed symmetrically compared to the feeding point, cf. Figure 4.4. This pattern is similar to the one of a Huygens source, and this antenna can then also be seen as a type of Huygens source design. Moreover, other designs with several load impedances were also presented in [62], achieving equivalent 'multipoles' (cf. Figures 4.5 which also can be viewed as dipole arrays. This type of antenna can then show good superdirective pattern but however suffer the effect of the resistances on their efficiency. Furthermore, the near-field coupling between the different loads also has to be taken into account in the design.

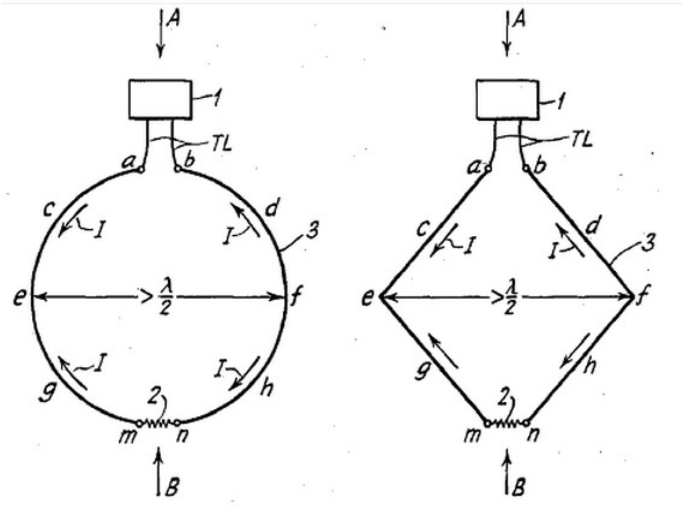

FIGURE 4.4: Loaded loop diagram from Beverage's 1920 patent [61].

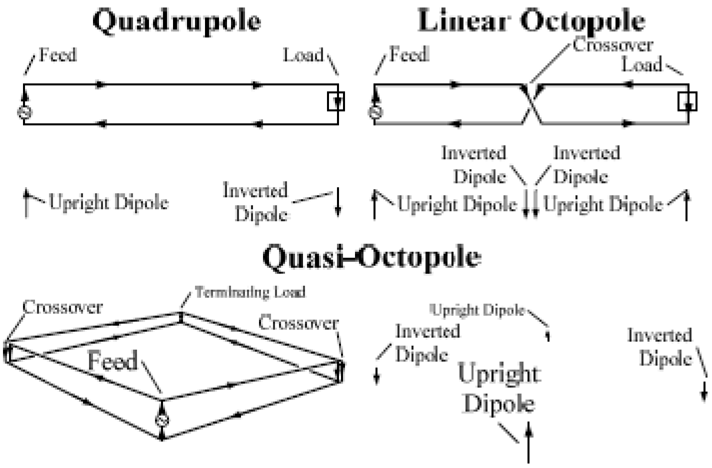

FIGURE 4.5: Loaded multipole antennas from [62]

4.3 Compact end-fire array antennas

End-fire superdirective arrays are made of closely spaced small antennas with independent excitation coefficients. The feasibility of compact arrays of this kind was demonstrated experimentally in [14] with an array of two monopoles with adjusted current feedings on each one, as shown in the diagram of Figure 4.6. The non-uniform feeding is achieved by either properly designed power dividers or by near-field parasitic element arrays. The latter ones use the near-field coupling between the element of the array to generate the rightly phased and amplified currents on each element, through the implementation of impedance loads. Only one element of the array then needs to be feeded with current. This technology is similar to the well known Yagi-Uda antennas [63], only that the unfed elements of the Yagi-Uda antennas are all shorted. The use of specific load impedances allows for precise control over the currents running through each element of the array. Moreover, compact end-fire arrays aim at reducing even more the spacing between elements than classical Yagi-Uda antennas (one tenth of wavelength instead of two or three tenth). They also tend to miniaturize the array element themselves, through techniques that are detailed in section 4.3.4.

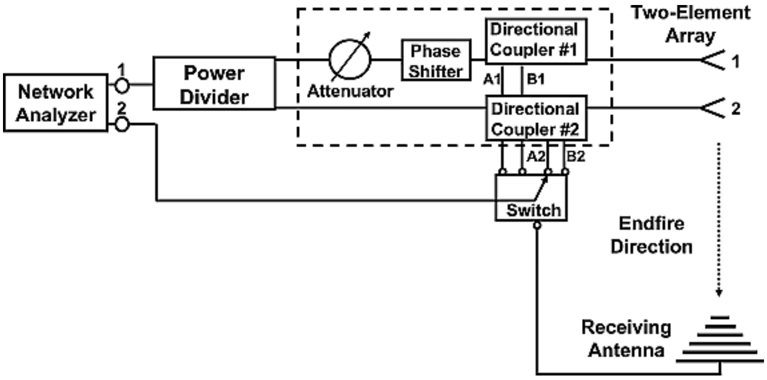

FIGURE 4.6: Diagram of the feeding circuit for a fully-driven two-monopole superdirective end-fire array, from [14].

4.3.1 Parasitic element end-fire arrays

Parasitic element end-fire arrays are a technique to design array antennas with different excitation currents for each element and only one feeding point. This done by taking advantage of the near field coupling occuring between the different elements. If the coupling is known, the induced current in every element can be calculated and adjusted through various methods.

The well known Yagi-Uda antennas use this design technique with arrays based on shorted dipoles [63]. The excitation coefficient optimization is made through the variation of the spacing between each elements and the length of each dipole.

Another method is to apply a specific impedance load on each element to generate the desired current.

4.3.2 Yagi-Uda-like arrays

Some compact end-fire arrays are directly inspired by the Yagi-Uda antenna [16], [64], [15], [17], [18], [65]. This technique is mostly suited for two-dipole arrays as it is shown in [64] that the current induced in a small dipole antenna by a closely placed one with parallel orientation is close to the current that maximize directivity as calculated in 2.2.1 or 3.1.3. This current is of magnitude close to the feeding current and phase shifted of about 180 degree, as described in 3.31. Moreover, in order to optimize the placing of the two dipoles, a study was made in [64] with two different small dipole design and various inter-element spacing.

A study over frequency also showed that two frequency points were found where the directivity was maximized. Both cases were toward an end-fire direction, but in one case, the shorted dipole acted as the director (meaning that the directivity was maximized in its direction) and in the other case it acted as a reflector (so the directivity was maximized toward the fed element). This is simply explained by the phase shift between the two excitation coefficients of the element that changes with frequency and is then closer to the maximization of directivity in one direction or the other.

It was experimentally demonstrated in [15], [16] and [17] that the maximum theoretical directivities and even gain could be achieved with this technique for two-element dipole-based arrays. What's more, this maximum gain of 7 dBi was reached with an array of size as small as $ka = 1$ in [15]. Attemps to reach maximum possible gain (10.3 dBi according to Chapter 3) with the same methods with three dipoles were made by [18] reaching 7.44 dBi of diretivity and 7.12 dBi of gain for $d = 0.02\lambda$ inte-element spacing, so $ka = 1.5$. The sensitivity of three-element arrays is indeed considerably greater than for the two-element case.

4.3.3 Parasitic elements with optimal load impedance

This technique has the advantage of controlling exactly the current through each of the parasitic element through the knowledge of the mutual coupling. This knowledge however necessitates the use of full-wave simulations or measurements made beforehand with the elements loaded with a reference load. The detail of the calculations are reviewed in Chapter 5. Also, one drawback of this method compared to the use of a power divider is that the calculated optimal load impedances may contain negative resistances. Manufacturing such component would increase drastically the complexity of implementation. Negative resistances are thus generally ignored and replaced by null resistances when this kind of array is designed ([22], [23]). An analysis of the optimal load calculation is proposed in Chapter 5. Figures 4.7 and 4.8

show example of measured prototypes of parasitic element arrays with the equivalent of three and four dipoles, respectively. Note that the loop-based arrays of Figure 4.7, from [20] is actually one and a half loop over a ground plane, equivalent to a three-loop array. This particular design is made for a measuring probe and does not aim for a good radiation efficiency (9.2 dBi of directivity for 7.0 dBi of gain), in which case electric dipoles are better choices because of higher radiation resistances [15] .

FIGURE 4.7: Magnetic-loop based end-fire superdirective arrays from [20]

(A)

(B)

FIGURE 4.8: Four-electric-dipole array from [22] (A) and [23] (B)

4.3.4 Single element design

Compact end-fire arrays show issues such as poor radiation efficiency (as seen in Chapter 3) and poor impedance matching, as discussed in [66], [15] and [17]. Both phenomenon can be explained by a decrease of the equivalent radiation resistance of the array (as the input resistance of the array is the sum of the radiation resistance and its loss resistance). Moreover, diminishing the total size of the arrays requires miniaturizing the unitary elements which generally also decreases their initial input resistance. Another problem to the miniaturization of the unitary elements is the increase of their input reactance as shown in [67]. Hence, a first rule to apply when designing the single elements of superdirective arrays is to use self-resonant antennas, as stated in [15].

Furthermore, the problem of small input resistance can also be dealt with through design technique to increase this resistance. Two methods are found in the literature. One is the use of a parasitic inductive element as in [68], [69] and [70]. It was indeed demonstrated that the addition of a parasitic stub ([69]) or a parasitic loop ([70]) in the near-field area of the radiating elements provides an increase in their input resistance and thus improves the impedance matching of parasitically loaded compact end-fire arrays.

Another method is to use folded dipole antennas, as shown in Figure 4.9. It is demonstrated in [71], [72] that folding a dipole with N_f arms multiplies its impedance by N_f^2. Also, this improves the radiation efficiency of the original electric dipole as it becomes [15]

$$\eta_{rad} = \frac{R_{rad,i} N_f^2}{R_{rad,i} N_f^2 + R_{loss} N_f} \tag{4.1}$$

$$\eta_{rad} = \frac{1}{1 + \frac{r_{loss}}{N_f}} \tag{4.2}$$

where $R_{rad,i}$ is the radiation resistance of the dipole without folding and $r_{loss} = \frac{R_{loss}}{R_{rad,i}}$ is the normalized loss resistance of the dipole before folding. The loss resistance of the antenna being proportional to the wires' length, it becomes $R_{loss} N_f$ with N_f folded arms. This method was used in [17], [15] and [18] to successfully design impedance matched supergain arrays, with measured gains as high as, respectively, 7.2, 7 and 5,8 dBi for two-electric dipole arrays. Pictures of the measured prototypes are shown in Figure 4.10.

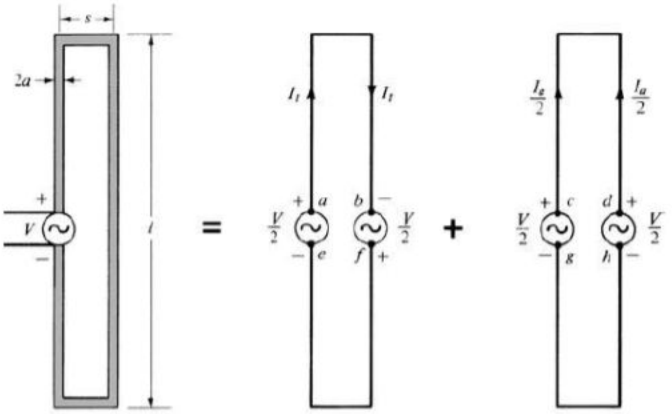

FIGURE 4.9: Folded dipole equivalent schematic diagram with propagating modes occurring simultaneously, according to [35]

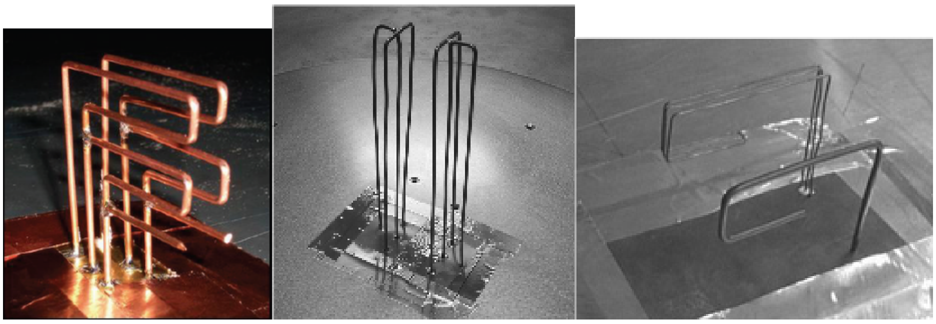

(A) (B) (C)

FIGURE 4.10: Prototypes of two-folded-dipole arrays, from [15](A), [17] (B) and [18] (C)

4.3.5 Bandwidth enhancement techniques

As previously discussed in Chapter 2, the increase of directivity without size increase comes with a quality factor increase thus narrowing the bandwidth of the antenna, considering a constant radiation efficiency ([36], [40]). This is only considering the bandwidth that is linked to the input impedance matching of the antenna. However, the -3dB bandwidth of a parasitic-element-array is also linked to the variations of its impedance loads over frequency. It has been shown that using Non-Foster element for impedance matching but also parasitic element loading improves the bandwidth of parasitic element arrays [73], [74], [49], [75]. This technique was also used to enhance the bandwidth of Huygens source designs [27].

Another method was presented in [76] where the antenna array presented by the same author in [20], were modified by increasing the volume of the loop elements, by stacking several loop in the broadside direction. This increase of volume used by the antenna would logically decrease the quality factor of the array and then increase its bandwidth.

4.4 Conclusions

This review of the state of the art shows that even if the Huygens sources would theoretically bring the best performances to superdirective or supergain arrays, there implementation are currently impractical in arrays. This point is also further explored in Chapter 6 were the design and simulation of a two-Huygens-source array is presented. Hence dipole-based arrays are preferred as their implementation is simple and they have shown good measured performances. Note that electrical-dipole-based arrays are also favored over magnetic dipoles for better radiation efficiency.

Moreover, as far as superdirective or supergain arrays are concerned, the use of parasitic-element or Yagi-like arrays as a feeding technique is often chosen in the literature as it is the most simple design method. The downside of this method

TABLE 4.1: Summary of the state of the art for compact-end-fire-superdirective arrays.

P	$d(\lambda)$	ka	Directivity (dBi)	Gain (dBi)
2	0.1	1 [15]	7.0	7.0
3 (1)	0.02	1.5 [18]	7.44	7.1
3 (2)	0.2	1.96 [77]		9.2
3 (3)	0.2	1.78 [20]	9.2	7.0
4 (1)	0.2	2.46 [23]	11.6	8.3
4 (2)	0.1	1.8 [22]	12.7	-12.1

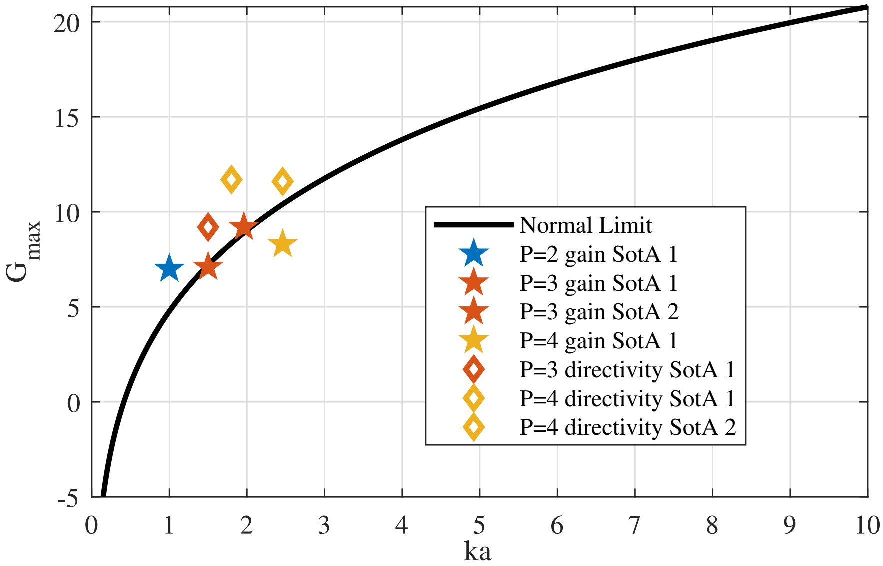

FIGURE 4.11: Plot of the performances reported in table 4.1 and compared to the normal directivity limit [3] as a function of *ka*.

over the fully-driven method with power dividers is that some design configurations would require the use of negative resistances as parasitic loading to get optimal performances. It was however shown that many configurations could be found to get close to maximum expected performances without any negative resistance. The parasitic-element-array method is used in this thesis to show prototypes of superdirective and supergain arrays that are detailed in Chapter 6. Chapter 5 also proposes an analysis of this feeding method and more precisely how the optimal resistance loadings are calculated and minimized.

The state of the art of small superdirective array is here summarized in table 4.1 and displayed in directivity and gain performances as a function of *ka* in Figure 4.11. When measurements were made with a ground plane, 3 dB is substracted to the results and the monopoles are considered as dipoles with twice their length, for *ka* calculation.

As shown in Figure 4.11. The performances reached with more than two-dipole arrays barely reach the normal gain limit, when losses are considered. Chapter 3 however suggested that it could be exceeded with three- or four-dipoles given individual radiation efficiencies of about 98%. This is experimentally demonstrated in Chapter 6 were the use of the gain maximization method presented in section 3.5 is proven to be a reliable method to get supergain performances.

Chapter 5

Parasitic Element Array Analysis

In this chapter, an analysis of the calculation of the optimal impedance loads of parasitic element arrays is proposed. The methods to compute the impedance to apply on a port in order to generate a given current through mutual coupling is first introduced, using the mutual impedances or scattering parameters of the array. Then, using an analytical model for the mutual impedance between two electric dipoles, theoretical values of optimal impedance load could be derived as a function of inter-element spacing for electric-dipole-based arrays.

This simple model is used to demonstrate the influence of some design parameters for the single dipoles, such as their length or height and their number or folded arms. The purpose of the analysis is to find methods that minimize the requirement for resistive loads in the optimized arrays. The study is applied to both case of directivity or gain maximization, considering lossy dipoles.

The model is not accurate enough to take into account the static coupling effects or precise dipole geometry changes, however, general design rules could be extracted to optimize the design of superdirective and supergain parasitic element arrays.

5.1 Optimal load calculation

For the computation of the impedance loads required to generate the adequate current on a given array element, it is necessary to know the mutual impedances or scattering parameters of the equivalent network of the array.

5.1.1 Mutual-impedance-based method

The mutual impedance Z_{21} between antenna 1 and antenna 2 can be defined by the equation [13]

$$V_1 = Z_{21} I_2, I_1 = 0 \tag{5.1}$$

This can be illustrated with the two-port network of Figure 5.1.

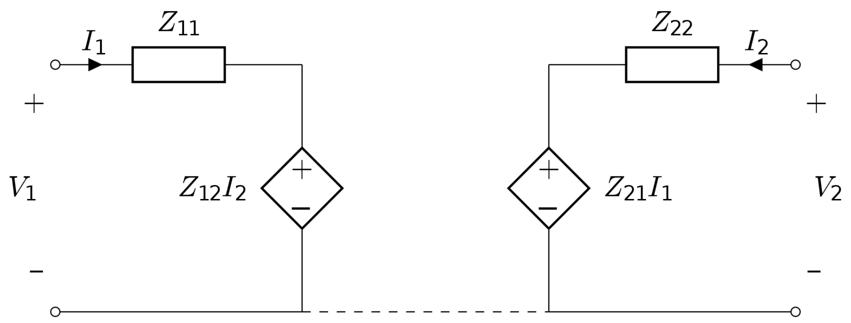

FIGURE 5.1: Equivalent circuit of a two-port network.

Hence, for a P element array, the voltage on the port of the p-th antenna is given by ([13])

$$V_p = \sum_{m=1}^{P} Z_{mp} I_m \tag{5.2}$$

This voltage is also calculated as a function of the load impedance $Z_{L,p}$ connected to the port,

$$V_p = -Z_{L,p} I_p \tag{5.3}$$

Thus, the impedance that provides current I_p is

$$Z_{L,p} = -\frac{\sum_{m=1}^{P} Z_{mp} I_m}{I_p} \tag{5.4}$$

This method is used in [78]. The other method is based on the scattering parameters of the network.

5.1.2 Scattering-parameter-based method

The diagram showing the scattering parameters of a two-antenna network is displayed in Figure 5.2. $\vec{E}_1(\theta,\phi)$ and $\vec{E}_2(\theta,\phi)$ are the electric field radiated by the first and second antenna, respectively. a_1 and a_2 are their excitation coefficients. From Figure 5.2,

$$\begin{aligned} a_1 &= u + \frac{b_1\Gamma_1}{1-\Gamma_1 S_{11}} \\ a_1 - u &= \frac{a_2 S_{12}\Gamma_1}{1-\Gamma_1 S_{11}} \end{aligned} \tag{5.5}$$

where u is the amplitude of the wave feeding the network. As only the ratio $\frac{a_1}{a_2}$ is of importance, a_1 can always be chosen such that $a_1 - u = 0$ so that $\Gamma_1 = 0$. Then a_2 is expressed as

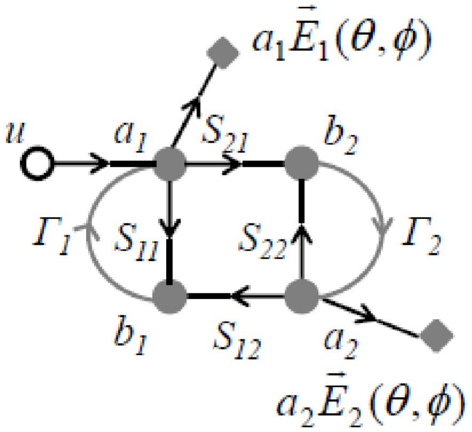

FIGURE 5.2: Scattering parameter diagram of a two-antenna network.

$$a_2 = \frac{a_1 S_{21} \Gamma_2}{1 - \Gamma_2 S_{22}} \tag{5.6}$$

Thus, the reflection coefficient desired at port 2 is given by

$$\Gamma_2 = \frac{a_2}{S_{21}a_1 + S_{22}a_2} \tag{5.7}$$

In the general case of a P-element network, for non fed ports, [22]

$$\Gamma_p = \frac{a_p}{\sum_{i=1}^{P} S_{pi}a_i} \tag{5.8}$$

These impedance calculations describe the fourth step of the optimization procedure of parasitic-element-superdirective arrays, as introduced in Chapter 2. The complete procedure is shown in Figure 5.3.

5.2 Analytical model for a dipole-based array

To provide an analytical analysis of the load impedances required to conceive superdirective end-fire arrays, mutual impedances model for half-wave electric dipoles were used in (5.4). Hence, the value of $Z_{L,p}$ could be computed as a function of spacing, taking the A_{0p} given by (2.49) coefficients instead of the I_p, as they are proportional. The mutual impedance formula for two dipole antennas is taken from [79] and is written:

$$Z_{21} = \frac{j\eta}{4\pi sinkh_1 sinkh_2} \int_{-h}^{h} F(z)dz \tag{5.9}$$

with

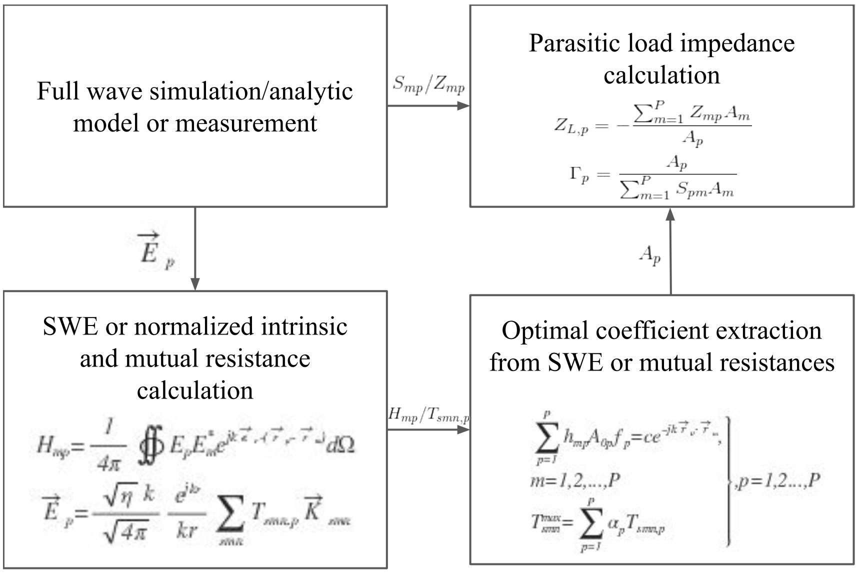

FIGURE 5.3: Complete optimization procedure for parasitic-element array.

$$F(z) = [\frac{e^{-jkR_1}}{R_1} + \frac{e^{-jkR_2}}{R_2} - 2coskh_1\frac{e^{-jkR_0}}{R_0}]sink(h_2 - |z|) \tag{5.10}$$

Here h_1 and h_2 are the half-length of the dipoles 1 and 2 and

$$R_0 = sqrt(d^2 + (z+b)^2) \tag{5.11}$$
$$R_1 = sqrt(d^2 + (z+b-h_1)^2) \tag{5.12}$$
$$R_2 = sqrt(d^2 + (z+b-h_2)^2) \tag{5.13}$$

with d and b the horizontal and vertical spacing between elements as represented in Figure 5.4.

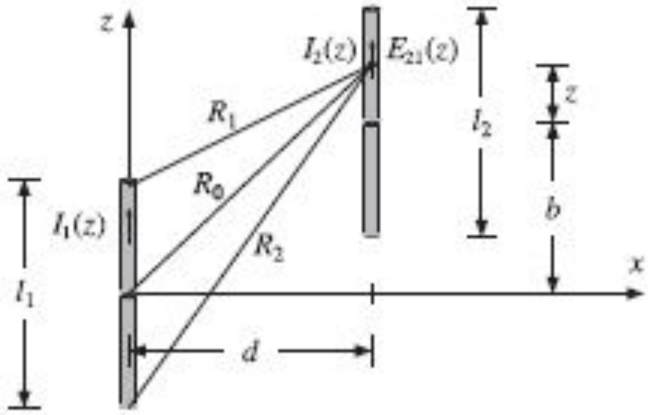

FIGURE 5.4: Representation and two parallel dipoles.

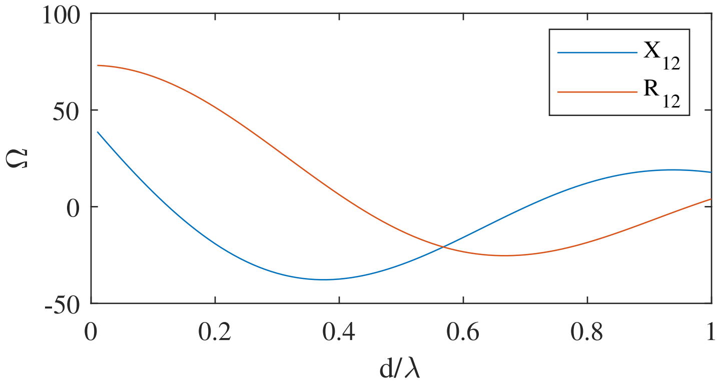

FIGURE 5.6: Real part R_{12} and imaginary part X_{12} of the mutual Impedance of two parallele dipoles of length $l = 0.5\lambda$, as a function of inter-element spacing d.

The real and imaginary parts of the mutual impedance between two halfwave dipoles computed with (5.9) are plotted in Figure 5.6, as a function of element spacing d. For arrays of more than two dipoles, the same mutual impedance calculation is made for each and every pair of dipoles, considering the different spacing between the elements. In this simple model, the presence of the other dipoles is ignored in the mutual impedance calculations. For example, in a three-dipole array, the calculation of Z_{31} does not take into account dipole 2 in the middle. Note that in the following, the placement order of the dipoles is described by Figure 5.5 with the directivity or gain being optimized in the $+\vec{z}$ direction.

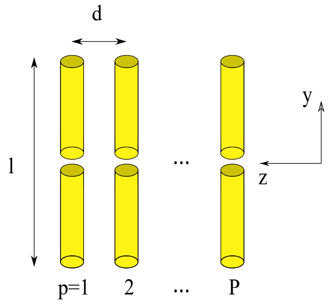

FIGURE 5.5: Diagram of a P-dipole array.

Hence, values of the optimal parasitic loads as a function of spacing can be calculated for dipole elements, using (5.9) and (5.10) and replacing the currents I_m by the A_m excitation coefficients which calculations are presented in Chapter 3. These values are plotted in Figures 5.7 and 5.8 for two- and three-halfwave-dipole arrays optimized successively for directivity and gain, considering that the dipoles have radiation efficiencies equal to $\eta = 98\%$.

One can note that the resistive parasitic load of each element is displayed on this Figures even if one element is fed and not loaded. This is done to provide all possibilities, as the choice on the element to feed can be simply made by eliminating the

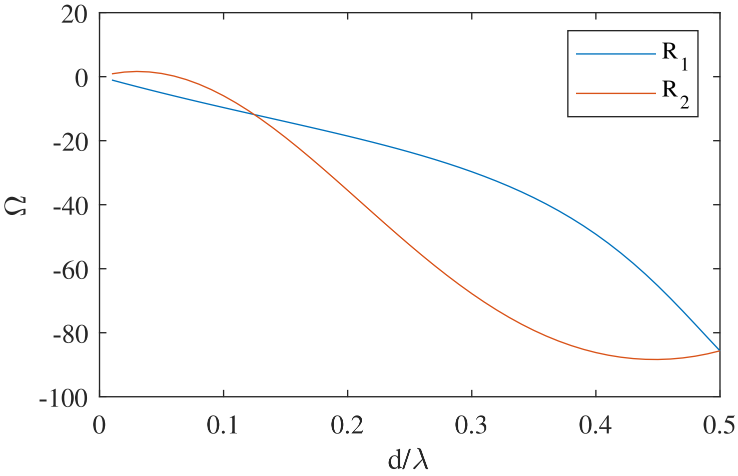

(A)

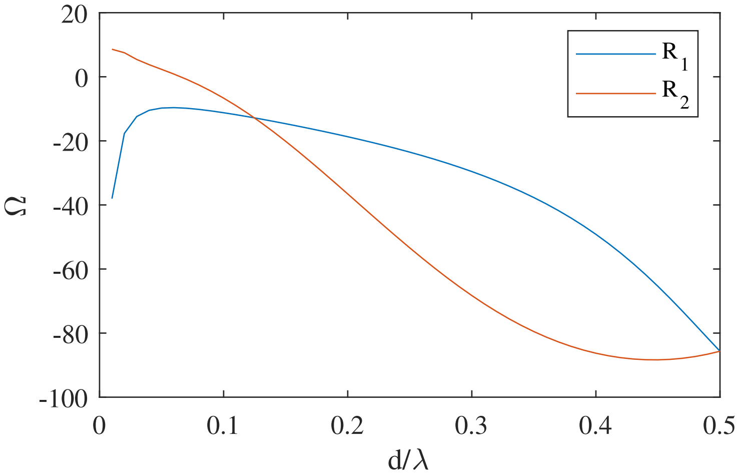

(B)

FIGURE 5.7: Optimal load resistances of a two-halfwave-dipole array optimized for directivity (A) and for gain (B), considering that the dipoles have radiation efficiencies equal to $\eta = 98\%$.

corresponding curve. Indeed, as expressed in (5.4), the value of the load impedances are independent to one another. The resistance curve that seems the less practical, because of a high positive or negative value can be chosen for the element to feed so it can be ignored.

Then, to have the most efficient design, it is preferred to have a null resistive part of the remaining loads.

Note that this analysis is in general not accurate enough to replace the use of a more complex simulation tool to compute the impedances of the network. This model does not take into account the capacitive and inductive couplings that occurs between two dipoles. Hence, the intrinsic impedance of a dipole is not influenced by the presence of another one in its vicinity, in this model, as it would be the case in reality [15]. Moreover, for more than two elements, the mutual impedance linking

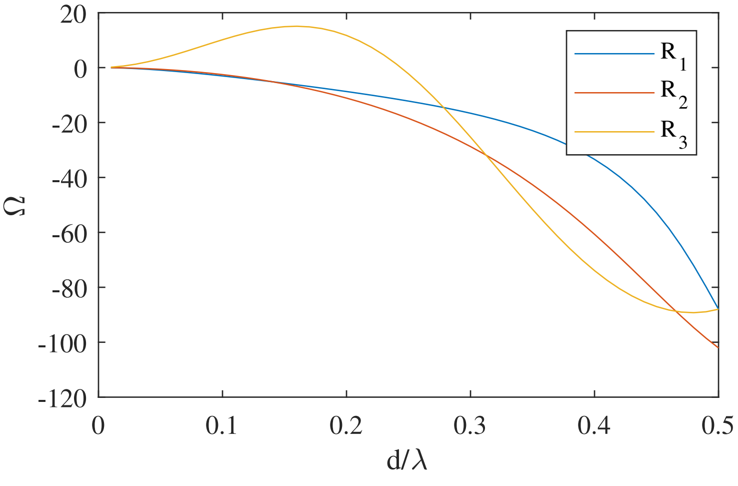

(A)

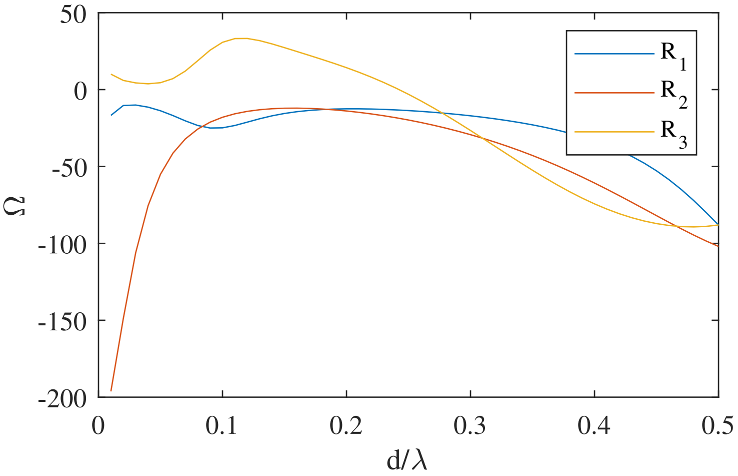

(B)

FIGURE 5.8: Optimal load resistances of a three-halfwave-dipole array optimized for directivity (A) and for gain (B), considering that the dipoles have radiation efficiencies equal to $\eta = 98\%$.

two dipoles is not affected by the presence of another one in between them, in this model.

However, the study of the values provided by these simulations may give a useful insight of the effect of various parameters, such as inter-element spacing and unitary element size, or intrinsic impedance.

Hence examining the curves of Figures 5.7 and 5.8 give an assessment of the right inter-element spacing to use in the design. As shown in the case (A) of these Figures, the shortest possible inter-element spacing is best in order to optimize directivity, for two- and three-dipole arrays. This is clearly not always the case when optimizing gain according to the (B) Figures. However, as explained in Chapter 3, the excitation coefficients calculated for gain optimization also make the performances of the array less sensitive to variations on this coefficients. Furthermore, the link between the variation of parasitic load impedance value and the variation of the corresponding excitation coefficient is to be established. This is done in the next section. The purpose is to determine if the gain optimization is always advantageous over the directivity optimization, even if the load resistances required are higher. The effect of neglecting this resistances will also be examined.

5.3 Impact of the use of resistive loads

The purpose of this section is to quantify the impact of resistive parasitic loads on the array gain. The calculation of gain with the knowledge of the loss resistance of the unitary elements of the array is done with (3.56). Adding a load resistance $R_{L,p}$ to element p then is equivalent to an increase of the loss resistance $r_{loss,p}$. This total normalized loss resistance is expressed as

$$r^{tot}_{loss,p} = r_{loss,p} + \frac{R_{L,p}}{R_{pp}} \tag{5.14}$$

Then, an average loss resistance can also be defined as

$$r_{loss} = \frac{\sum_{p=1}^{P} |a_p|^2 (r_{loss,p} + \frac{R_{L,p}}{R_{pp}})}{\sum_{p=1}^{P} |a_p|^2} \tag{5.15}$$

Then, the gain can be simply expressed by (3.57). The influence of a mere 1% loss resistance is shown on Figure 3.8 for infinitesimal dipole arrays of up to four elements. This would be equivalent to having an average load resistance of 0.5Ω with dipoles of 50Ω input resistance and no intrinsic loss resistance. The need to keep the use of resistive load to a minimum is thus a problem to adress.

5.4 Influence of the single element design

5.4.1 Dipole length

The effect of diminishing the dipole's length can also be seen. Calculating the parasitic loads with a dipole length of $l = 0.3\lambda$ gives the values of Figures 5.9, 5.10 and 5.11.

It can be noticed that both case of optimization (directivity or gain), all parasitic load values are decreased for all value of inter-element spacing. This is due to the fact that the length diminution of the dipoles also decreases the mutual impedances of the array, as shown in Figure 5.12. Then, from (5.4), it is obvious that the decrease of the mutual impedances leads to a decrease of load impedance, for both real and imaginary part.

It is important to note however that in this modelization, decreasing the dipole's length increases its input reactance as it gets further from its resonant length, where

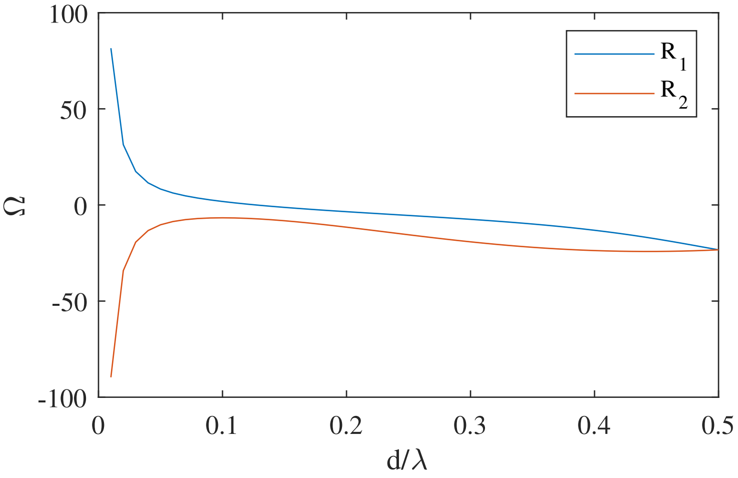

FIGURE 5.9: Optimal load resistances for an array of two dipoles of length 0.3λ and radiation efficiencies of 98 %, for gain optimization.

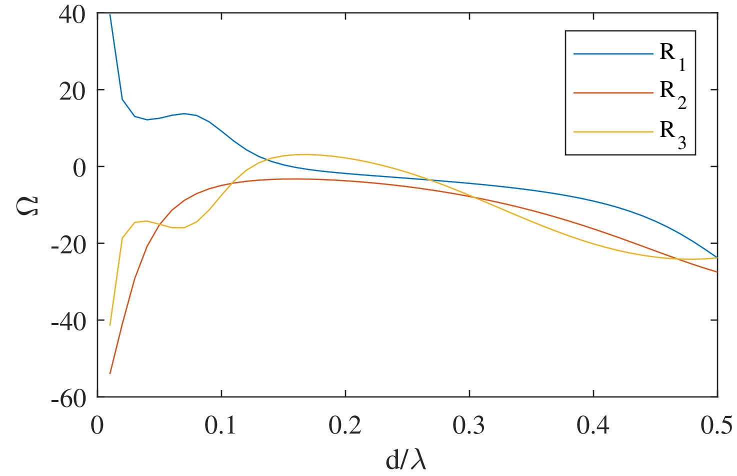

FIGURE 5.10: Optimal load resistances for an array of three dipoles of length 0.3λ and radiation efficiencies of 98 %, for gain optimization.

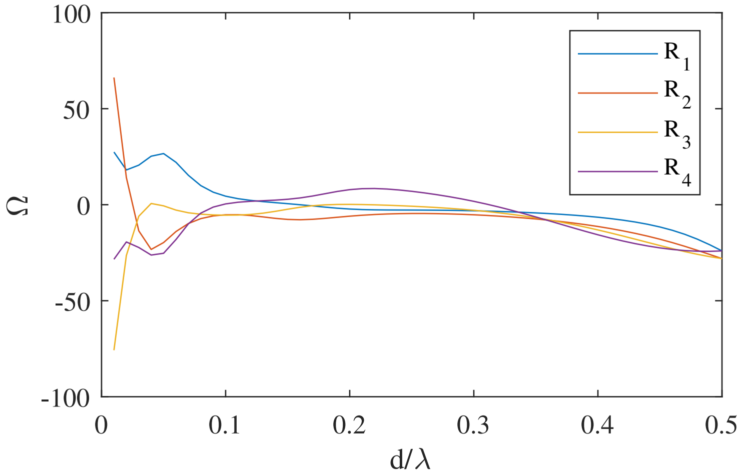

FIGURE 5.11: Optimal load resistances for an array of four dipoles of length 0.3λ and radiation efficiencies of 98 %, for gain optimization.

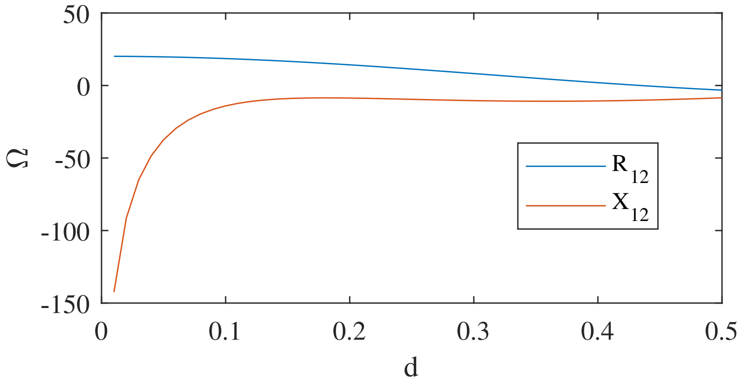

FIGURE 5.12: Mutual resistances and reactances between two electric dipoles of length 0.3λ.

its input reactance is zero. This high intrinsic reactance also influences the mutual reactances, especially when the inter-element spacing is close to zero as the mutual impedance tends to the intrinsic impedance of a single element. This can be seen in Figure 5.13. Taking the real parts and imaginary parts of (5.4) gives

$$R_{L,p} = R_{pp} - \sum_{m=1,m\neq p}^{P} R_{mp}Re(\frac{I_m}{I_p}) + \sum_{m=1}^{P} X_{mp}Im(\frac{I_m}{I_p}) \tag{5.16}$$

$$X_{L,p} = -X_{pp} - \sum_{m=1}^{P} R_{mp}Im(\frac{I_m}{I_p}) - \sum_{m=1,m\neq p}^{P} X_{mp}Re(\frac{I_m}{I_p}) \tag{5.17}$$

Hence, the input reactance X_{pp} appears only in the calculation of the value of the load reactance X_L^p (as $Im(\frac{I_p}{I_p} = 0$ in (5.16)). Using non resonant antennas may then create the need for high load reactance, that would require the use for large capacitors of self-inductance components. It is preferred to avoid that kind of component

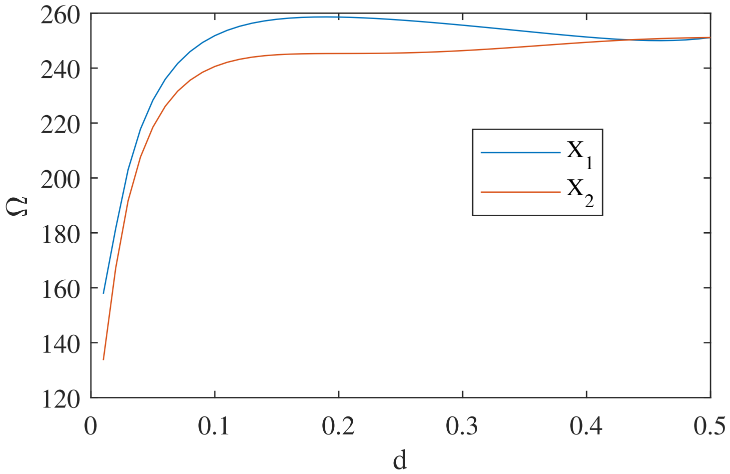

FIGURE 5.13: Optimal load reactances for an array of two electric dipoles of length 0.3λ.

as they also come with large intrinsic resistances, which is why the use of resonant antennas is favored in the design of parasitic-element arrays, as it is explained in [15].

Nevertheless, the miniaturization (keeping the resonant property) of the elements of the array seems to improve the value of optimal parasitic load. Indeed, miniaturized resonant antennas should have a low input resistance and an input reactance close to zero and as seen in Figure 5.12, this would also decrease mutual resistance and reactance which would decrease the absolute value of the resistive and reactive loads according to (5.16) and (5.17). Not to mention the fact that decreasing the unitary elements' sizes also brings down the total antenna size. In any case, miniaturizing the elements does however worsen its radiation efficiency (as shown in [41] and [53]), so there is still a trade-off to consider.

5.4.2 Dipole folding

As mentioned in Chapter 4, the use of folded dipoles increases the input resistance of the simple dipole by multiplying it by N_f^2 where N_f is the number of folded arms [72]. Moreover, according to [80], the mutual impedance between two folded dipoles is also multiplied by N_f^2, at least for the case of a simple fold, $N_f = 2$. Thus, from (5.4), the optimal load is multiplied by the same number which is an issue as large impedance loads are to be avoided because of the high resistances it involves.

A possible compromise to use antenna folding for the increase of input impedance (for impedance matching [15]) but to also keep the increase of load impedance to a minimum is to only fold the fed element, as it is done in [18], for instance. Indeed, according to [80], the mutual impedance between a classical electric dipole and a folded dipole is the same as the one between to simple dipoles but multiplied by 2, for $N_f = 2$ arm folds.

5.5 Sensitivity factor application

The sensitivity factor described in section 3.4 links the expected directivity considering the standard variation applied to the excitation coefficients. This can be applied to the sensitivity to load impedance value given that, from (5.4)

$$Z_{L,p} + Z_{pp} = -\frac{\sum_{m=1,m\neq p}^{P} Z_{mp} I_m}{I_p} \tag{5.18}$$

then, taking the derivative with respect to I_p,

$$\frac{d(Z_{L,p} + Z_{pp})}{dI_p} = -\frac{Z_{L,p} + Z_{pp}}{I_p} \tag{5.19}$$

Thus, knowing that Z_{pp} is a constant,

$$\begin{aligned} \frac{d(Z_{L,p})}{Z_{L,p} + Z_{pp}} &= -\frac{dI_p}{I_p} \\ &= -\frac{dA_p}{A_p} \end{aligned} \tag{5.20}$$

as the excitation coefficients A_p are proportional to the currents I_p. Taking expected value of the squared module,

$$\begin{aligned} \langle |\frac{d(Z_{L,p})}{Z_{L,p} + Z_{pp}}|^2 \rangle &= \epsilon^2 \\ \frac{\epsilon_L^2}{|Z_{L,p} + Z_{pp}|^2} &= \epsilon^2 \end{aligned} \tag{5.21}$$

with ϵ the standard variation of excitation coefficients as defined in Chapter 3 and ϵ_L the standard deviation on the module of the load impedance. Hence, the deviation on coefficient are influenced by the intrinsic impedance of the p-th element. A larger intrinsic impedance Z_{pp} will in general lower the sensitivity of the array to variations of the load impedance $Z_{L,p}$. This implies that if changing the height of the dipole diminishes the optimal load resistances as shown in section 5.4.1, neglecting these resistances will still have the same effect on the excitation coefficients regardless of the dipoles' height. This is because the change of dipole height has the same effect on both the numerator and the denominator of (5.21).

5.6 Input Impedance calculations

The input impedance of the array that can also be measured at the port of the element that is fed can be deduced from the mutual impedances and excitation coefficients of the array. This is done with the equivalent circuit model of the array as represented in Figure 5.1 in the case of two elements. In this case, the voltage at the first port is expressed as

$$V_1 = I_1 Z_{11} + Z_{12} I_2 \tag{5.22}$$

Then, from (5.4),

$$I_2 = -\frac{Z_{21} I_1}{Z_{L,2} + Z_{22}} \tag{5.23}$$

so that

$$V_1 = I_1 [Z_{11} - \frac{Z_{12} Z_{21}}{Z_{L,2} + Z_{22}}] \tag{5.24}$$

Thus, as the input impedance is defined as $Z_{in} I_1 = V_1$ and $Z_{12} = Z_{21}$,

$$Z_{in} = Z_{11} - \frac{Z_{21}^2}{Z_{L,2} + Z_{22}} \tag{5.25}$$

for a two-element array. The input reactance is then

$$X_{in} = X_{11} - \frac{2X_{21}R_{21}(R_{11} + R_{L,2}) - (R_{21}^2 - X_{21}^2)(X_{11} + X_{L,2})}{|Z_{L,2} + Z_{22}|^2} \tag{5.26}$$

The point where the reactance is zero is then different from the resonning point of the single element. It has been however seen in section 5.4.1 that when the unitary elements have null reactances, their mutual reactance is also close to zero when the spacing between element is small. Having resonant unitary elements then should make the array resonate at a close frequency point. This assessment is further investigated in the experimental part of the next chapter.

Their remains the real part of this input impedance that tend to be small compared to the standard 50 Ω when the inter-element spacing is close to zero, as shown by Figures 5.14 and 5.15 for directivity and gain maximization, respectively. As previously seen in section 5.4.2, folding the fed element is a way of bringing back up this input resistance.

For both dipole folded with N_f arms,

$$\begin{aligned} Z_{in,2f} &= N_f^2 Z_{11} - \frac{N_f^2 Z_{21}^2}{N_f^2 (Z_{L,2} + Z_{22})} && (5.27) \\ &= N_f^2 Z_{11} - \frac{Z_{21}^2}{Z_{L,2} + Z_{22}} && (5.28) \end{aligned}$$

For only the fed element folded,

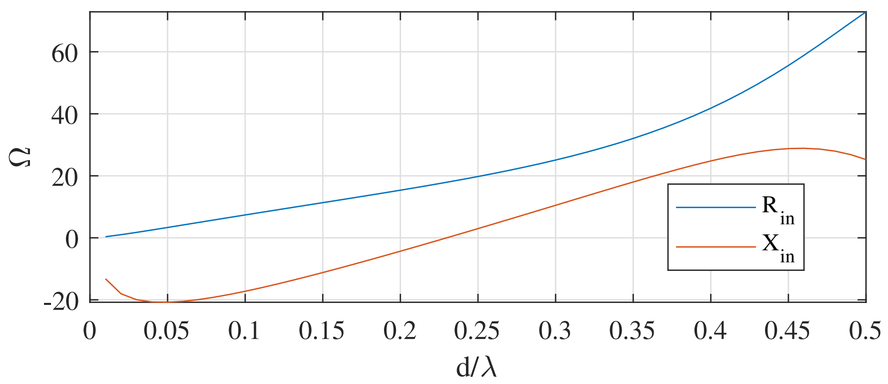

FIGURE 5.14: Real and imaginary part of the input impedance of a two-halfwave-dipole array optimized for directivity.

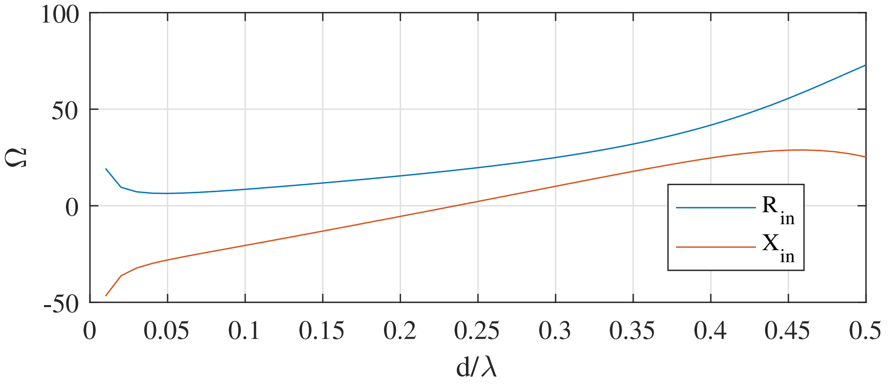

FIGURE 5.15: Real and imaginary part of the input impedance of a two-halfwave-dipole array optimized for gain considering 98% efficient dipoles.

$$Z_{in,1f} = N_f^2 Z_{11} - \frac{N_f Z_{21}^2}{N_f Z_{L,2} + N_f^2 Z_{22}} \tag{5.29}$$

$$= N_f^2 Z_{11} - \frac{Z_{21}^2}{Z_{L,2} + N_f Z_{22}} \tag{5.30}$$

5.7 Conclusions

As a conclusion to this Chapter some key rules for the design of parasitic-element-compact arrays can be extracted.

- First, the use of resistive loads cause the gain of the array to fall drastically as it is equivalent to adding loss resistances to the elements which impact in shown in section 3.3.

- Analytic solutions to avoid the use of load resistances could not be derived as it would require a much more complex modelization. This study can show interesting specific values of inter-element spacing to minimize resistances but the optimization should ultimately be made with the help of full-wave simulations.

- The use of resonant antennas is to be preferred to avoid the need for high load and input reactances as explained in [15] and demonstrated in this Chapter for the case of small dipole arrays.

- For a two-dipole array, the optimal resistance needed on the reflector element is generally close to zero when the spacing is about 0.1λ. The resistances needed on the director and reflector of a three-dipole arrays will however never be both equal to zero in general, though this will vary with the specific geometry of the individual dipoles which are not modeled here.

- Decreasing the size of the elements decreases the required load impedances (in real and imaginary part when using resonant designs,) but increases the sensitivity of the array to load variations by the same factor. This is nevertheless advantageous for implementation as it decreases the values of the required reactive components which will then have lesser intrinsic resistances. The trade-off between low radiation efficiency and low load resistance is to be considered for the maximization of gain.

- Using dipole folding to increase element efficiency and input impedance also increases load impedance by the same factor. The folding of the fed element alone limitates the increase in load impedance while keeping a high input impedance. This is also useful to increase the efficiency of this particular element as the loss resistance brought by the feeding circuit are linked to it.

These conclusions will then be used in the design of dipole array prototypes in Chapter 6.

Chapter 6

End-fire Array Design and Measurements

The purpose of this Chapter is to bring the experimental validation of the analysis previously made. The most important contribution of this work on the field of small superdirective array design is the use of gain optimization taking into account the loss resistances of the array elements. Measurements of prototypes using this specific excitation coefficient calculation are done in order to show that it can provide a significative intrinsic gain improvement over the directivity maximization method. This result is not trivial as the need of parasitic impedance loads with resistive parts can be expected according to Chapter 5. It is thus shown here that neglecting these resistive parts does not affect the array gain too importantly, as the array sensitivity is also lowered by the use of these excitation coefficients.

The problem of designing Huygens-source-based arrays is also investigated in this Chapter. Chapter 3 describes how Huygens-source-based arrays are the arrays that can reach the highest theoretical directivities for given inter-element spacing. The realization of such arrays yet brings difficulties as one single element is made of two-dipoles that need to have properly balanced excitations. Also, as it requires the use of magnetic dipoles, their radiation efficiency is also in general much lower than those of small dipoles [15]. The design of highly directive small antennas with low radiation efficiency remains of interest, as it is still suited for applications that require spatial selectivity. A proposition of a two-Huygens-source array design is thus proposed in this Chapter. This designed was however not made into a prototype for measurements as it showed a high sensitivity to the precision of parasitic impedance loads as well as simulation accuracy. The presented design method may however lead to further experimentation with different designs, in future works.

The chosen working frequency is $850MHz$ as it is close to the frequencies used for RFID systems which are one of the possible applications for superdirective array antennas.

6.1 Dipole-based arrays

It was shown with full-wave simulations of halfwave-dipole-based arrays in section 3.5 that excitation coefficients that maximize gain rather than directivity could be found. The gain improvement seems to be sensitive for three- or four-element arrays. The experimental demonstration of this statement is made in this section with arrays of printed electric dipoles of three and four elements. The measurements for halfwave dipoles and for small bent dipoles will be shown. Also, the design rules for optimizing the parasitic impedance loads are validated through these measurements.

6.1.1 Dipole designs

The design of the single dipole used in the arrays is introduced in this section. The dipole has to be small and show a good radiation efficiency as explained in Chapter 4. To this end, the chosen design is close to the one presented in [15], which is a bent folded dipole. The folding is however limited to the element that is fed only, so the required parasitic load keep a low value, as explained in Chapter 5.

Furthermore, the feeding method used for measurements is based on a specific balun design, that adds some loss resistance. The design of the balun was not done specifically for this application and is not detailed here as it is out of the scope of this work.

In Chapter 3, it was shown that considering single electric dipoles with radiation efficiencies of 99%, three and four-element arrays are expected to yield the best gain performance compared to Harrington's 'normal' limit [3].

The purpose is to realize array antennas with similar average radiation efficiency for its unitary elements. The average calculation is used in this context as the fed element is different from the other as it is considered with the balun feeding device that decreases its total radiation efficiency. Moreover, as suggested in Chapter 5, the fed element is folded with $N_f = 2$ arms for each of the proposed arrays. This is done for input impedance increase as explained in Chapter 5 but also for radiation efficiency improvement, as the effect of the folding is equivalent to dividing the loss resistance of the dipole by N_f and the loss resistance of the balun by N_f^2. Indeed, the radiation efficiency of the set composed of the folded dipole and the balun is expressed as

$$eff_{rad} = \frac{N_f^2 R_{rad}}{N_f^2 R_{rad} + N_f R_{loss,dip} + R_{loss,balun}} \tag{6.1}$$

$$= \frac{R_{rad}}{R_{rad} + \frac{R_{loss,dip}}{N_f} + \frac{R_{loss,balun}}{N_f^2}} \tag{6.2}$$

with R_{rad}, $R_{R_{loss,dip}}$ the radiation and loss resistances of the dipole without folding and $R_{loss,balun}$ the loss resistance of the balun.

Two kinds of arrays are demonstrated in this section. Arrays of bent electric dipoles and arrays of straight halfwave dipoles. Both kinds are made of printed copper on a Rogers 4003 substrate. The length of the dipoles is 0.44λ for the bent one, given a height of $\frac{0.44\lambda}{3}$, $\frac{0.44\lambda}{4}$ for the three-element and four-element-arrays, respectively. The length of the straight dipoles is 0.43λ. All the dipoles are 3mm wide and 0.07mm thick. The thickness of the substrate is 1.524mm. The different dipole used are shown in Figures 6.1 and 6.2. Their radiation efficiencies are 96% and 98% for the folded bent, and straight dipoles, respectively, taking into account the balun losses. The radiation efficiencies of the dipoles with direct feeding without balun are considered equal to 100% by the simulation software.

(A) (B)

FIGURE 6.1: Straight simple dipole (A), and folded dipole with balun (B).

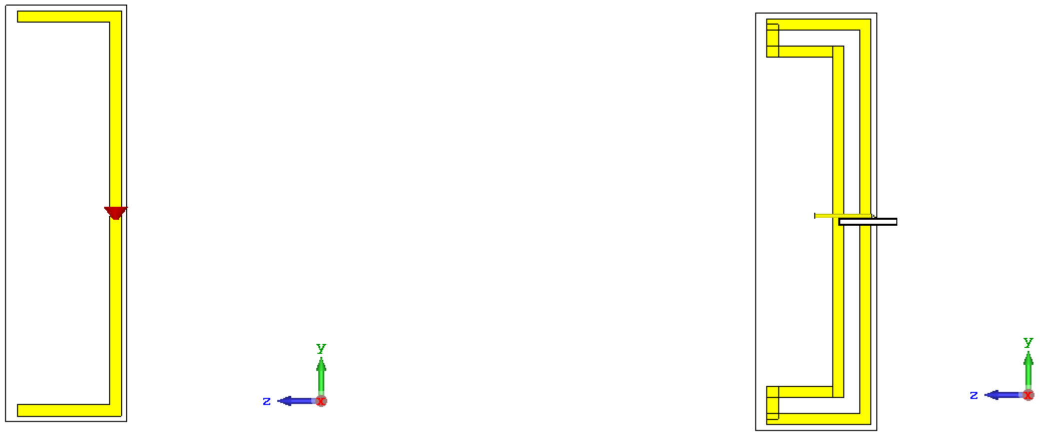

(A) (B)

FIGURE 6.2: Bent simple dipole (A), and bent folded dipole with balun (B).

6.1.2 Optimization of arrays of two, three and four dipoles

The average radiation efficiencies of the dipole-arrays are originally

$$eff_{P,bent} = \frac{0.96 + (P-1)}{P} \tag{6.3}$$

$$eff_{P,straight} = \frac{0.98 + (P-1)}{P} \tag{6.4}$$

For the P-bent-dipole- and P-straight-dipole-arrays, respectively, initially considering equal excitation coefficients for the elements. This provides estimated approximate radiation efficiencies of $eff_{2,bent} = 98\%$, $eff_{3,bent} = 99\%$, $eff_{2,straight} = 99\%$, $eff_{3,straight} = 99\%$ and $eff_{4,straight} = 99\%$.

The optimal excitation coefficients are calculated using the classical method presented in equation (2.49) where $\vec{f}_p(\theta_0, \phi_0)$ used here are the electrical far-field computed through the full-wave simulations. These far-field are computed by successively feeding each dipole in the array while the others are loaded with 50Ω resistances in order to extract the scattering parameters. The radiation efficiency of each antenna eff_p is also computed during this step.

Optimal impedance loads can then be calculated from the excitation coefficients and the computed scattering parameters, according to equation (5.4). For practicality, when a negative resistance was found it was replaced by a null resistance. Also, in the case of gain maximization, positive resistances were also set to zero. These modifications led to change in excitation coefficients that could be found again with (5.4).

The optimized arrays performances could then be computed by combining the the individual electrical far-field results obtained earlier and weighting them by the lastly calculated excitation coefficients.

Gain optimization

Five cases of arrays were chosen as prototypes as they presented the best performances for gain optimization, with the parasitic element implementation used. In that case of optimization, the radiation efficiency computed for each element is used to extract their loss resistances as seen in section 3.5. The prototypes are a two-dipole array with $d = 0.05\lambda$ inter-element spacing, a two-bent-dipole array with $d = 0.1\lambda$ inter-element spacing, a three-dipole array with $d = 0.08\lambda$ inter-element spacing, a three-bent dipole array with $d = 0.12\lambda$ inter-element spacing and a four-dipole array with $d = 0.13\lambda$ inter-element spacing. The computed 3D-far-field patterns for each case is displayed in Figures 6.3, 6.4 and 6.5 for two-, three- and four- dipole arrays, respectively.

The performances and optimal impedance loads used are shown in Tables 6.2, 6.1, 6.3, 6.4 and 6.6, for each array, under the column labeled ’Simu. 1’, as ’Simu.

2′ is explained in section 6.1.3. Note that all the arrays are fed by port 1 so that the components calculated for this port are not used.

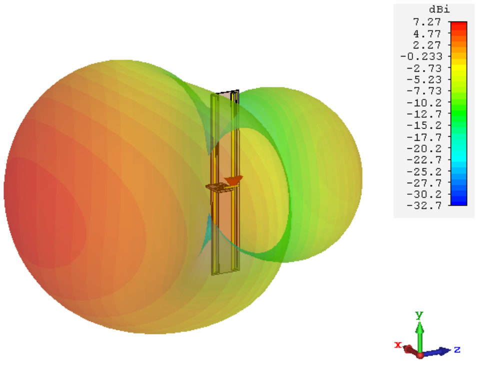

(A) (B)

FIGURE 6.3: 3D-gain pattern of the two-dipole-array with $d = 0.05\lambda$ inter-element spacing (A) and of the two-bent-dipole-array with $d = 0.1\lambda$ inter-element spacing (B) (cf. Tables 6.2 and 6.1).

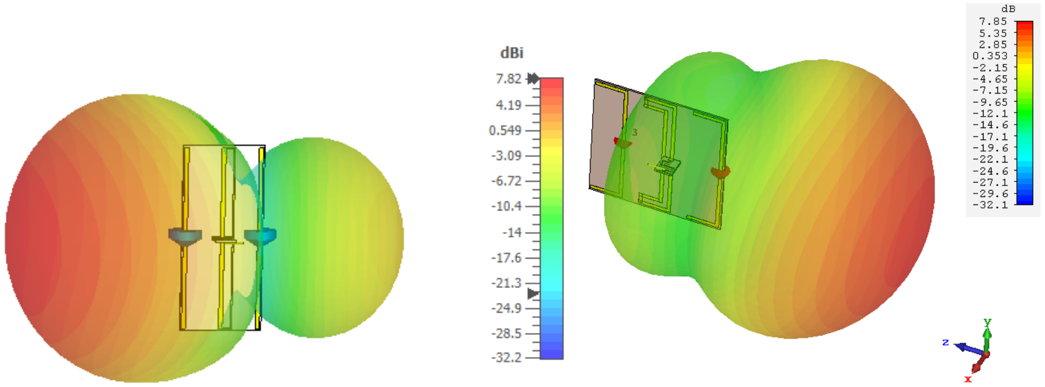

(A) (B)

FIGURE 6.4: 3D-gain pattern of the three-dipole-array with $d = 0.08\lambda$ inter-element spacing (A) and of the three-bent-dipole-array with $d = 0.12\lambda$ inter-element spacing (B), for gain optimization (cf. Tables 6.3 and 6.4).

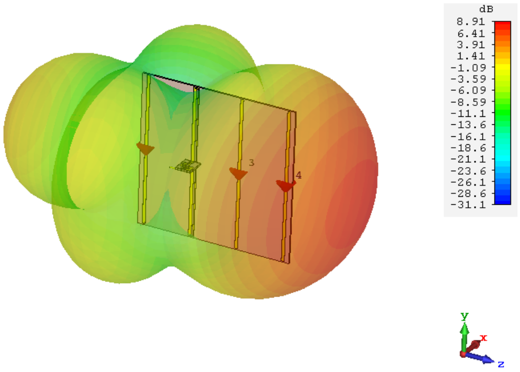

FIGURE 6.5: 3D-gain pattern of the four-dipole-array with $d = 0.13\lambda$ inter-element spacing, for gain optimization.

Directivity optimization

In the case of directivity maximization, the radiation efficiency is not taken into account. This optimization was made on some of the prototypes previously designed for maximum gain. The prototypes used here were chosen as they presented the closest results through simulation to the theoretical maximum directivity. These prototypes are the three-dipole array with $d = 0.08\lambda$ inter-element spacing and the four-dipole array with $d = 0.13\lambda$ inter-element spacing. The 3D-far-field pattern computed is shown in Figure 6.6 and the performances results and impedance loads are displayed in Tables 6.3 and 6.7, under the column labeled 'Simu. 1'. Note that in these cases, positive resistances were used for loading as directivity was prioritized over gain.

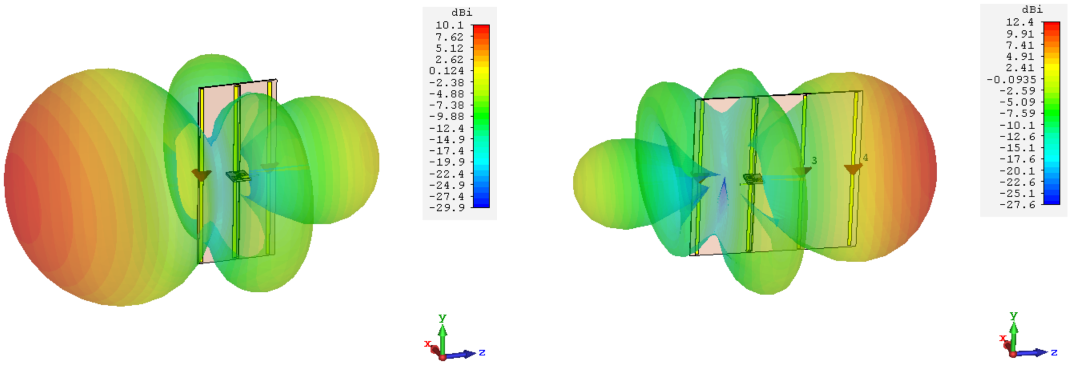

(A) (B)

FIGURE 6.6: 3D-directivity pattern of the three-dipole-array with $d = 0.08\lambda$ inter-element spacing (A) and of the four-dipole-array with $d = 0.13\lambda$ inter-element spacing (B), for directivity optimization (cf. Table 6.7).

6.1.3 Second phase of simulation

In order to confirm the first simulation results obtained through the far-field combination that was made through post-processing, another iteration of simulation is made. In these new simulations, only the first port is excited through the balun and the parasitic dipoles are loaded with lumped elements using the impedance specifications previously calculated (using no resistance in the gain optimization cases and only positive resistances for the directivity optimization cases). Note that these impedance loads are also modified in some cases to match the ones that could actually be implemented for measurements.

The performances found in these simulations and optimal impedance loads used are shown under the column labeled as ′Simu. 2′ in the Tables 6.2, 6.1, 6.3, 6.4, 6.6, 6.5 and 6.7, for all previously simulated cases.

Some differences of maximum directivity and gain can be noted compared to the previous results provided by far-field combination. These differences are due to the change in the simulation process, knowing that the excitation coefficients and corresponding impedance loads were specifically calculated in the first case of simulation. Hence, if the sensitivity of the optimization relatively to the precision of these coefficients is too high, small differences in the simulation process can yield important performance discrepancies.

The results are also presented through the 2D-far-field pattern taken in the $\phi = 0$ and $\phi = 90$ planes and with the curves of directivity and gain found in the $\theta = 0$ direction over frequency. This is shown in Figures 6.11, 6.9, 6.18, 6.14, 6.20 and 6.22.

The simulations results with ideal impedance values are however shown in the cases that show the most differences, in Figures 6.6 and 6.22 for the cases of the maximization of directivity of the three- and four-dipole arrays.

Note that the far-field pattern are plotted at the frequency at which the higher directivity or gain is found for directivity or gain maximization, respectively.

These maximum are indeed not always at the center frequency of 850MHz, as a frequency shift of the maximum directivity and gain also occurs with these new simulations. It was however found that these shifts were dependant on the meshing of the simulation process. This could be illustrated by the different simulation results obtained through several consecutive executions of the frequency based solver, which increases the number of mesh used with each iteration. It is shown in Figure 6.12 for the example of the simulation of the two-straight-dipole array where the maximum directivity is shifted to a higher frequency with the increase of number of mesh in the simulation. Also, it is to be noticed that the discrepancies appear to be more important in the directivity optimization cases as the sensitivity factor is higher in that case than in the gain optimization case, as seen in section 3.4. This can also be more apparent is the case of bent dipoles as the geometry is more complex to simulate. The frequency shift is also logically apparent in the input reflection coefficient curves, as it was seen in chapter 3 that the maximum directivity performance of the array affects its radiation efficiency and thus its impedance matching. This can be seen through the curves of input reflection coefficients over frequency displayed in Figures 6.8, 6.10, 6.17, 6.13, 6.15, 6.21 and 6.19. The measurement results are detailed and compared to these simulations in the next section.

6.1.4 Measurement results

The measurements were made in an anechoic chamber, with a set-up that can be seen in Figures 6.7a and 6.7b, for the two- and three-straight-dipole array prototypes, respectively. The realized gain of the antennas under tests could be extracted with a probe antenna of which the realized gain was known and having previously measured the transmission coefficient between the antenna under test and the probe antenna. The input reflection coefficient was also measured and the intrinsic gain could then be derived from the realized gain. The gain was hence measured on the vertical ($\phi = 90$) and horizontal ($\phi = 0$) cutting planes. The radiated power needed to derive the directivity was extracted by integrating both plane and interpolating the rest of the radiation pattern. This work focuses on intrinsic gain and the realized gain is thus not showed as the antenna impedance matching was not optimized for each case. Nevertheless, the measured and simulated input reflection coefficients are displayed in Figures 6.8, 6.10, 6.17, 6.13, 6.15, 6.21 and 6.19. Moreover, the measured performances of the balun used are shown in Appendix D.

Two-dipole arrays

The measured performances of the two-dipole arrays are shown in Tables 6.2 and 6.1. These results are also displayed in Figures 6.11 and 6.9 with curves of directivity and intrinsic gain over frequency and 2D-gain patterns over the $\phi = 0$ and $\phi = 90$ planes.

The two-bent-dipole array with $d = 0.1\lambda$ inter-element thus shows results very close to the simulations. A small frequency shift of 8MHz is found in measurement, compared to 6MHz predicted by simulation.

The two-dipole array with $d = 0.05\lambda$ has a measured maximum gain with a larger shift in frequency of 28MHz, compared to 6MHz in simulation. The closest inter-element spacing can explain this more important difference with the simulation.

Moreover, the measured gain is about 1dB higher than the theoretical and simulated values. This implies that the radiation losses initially calculated in the simulation model are more important than what was measured. This is not trivial as the directivity extracted from the measurements is lower than simulation results (by O.2dB). A lower directivity could be a good explanation for a higher gain but this neglects the fact that the intrinsic gain was the parameter being maximized in the first place.

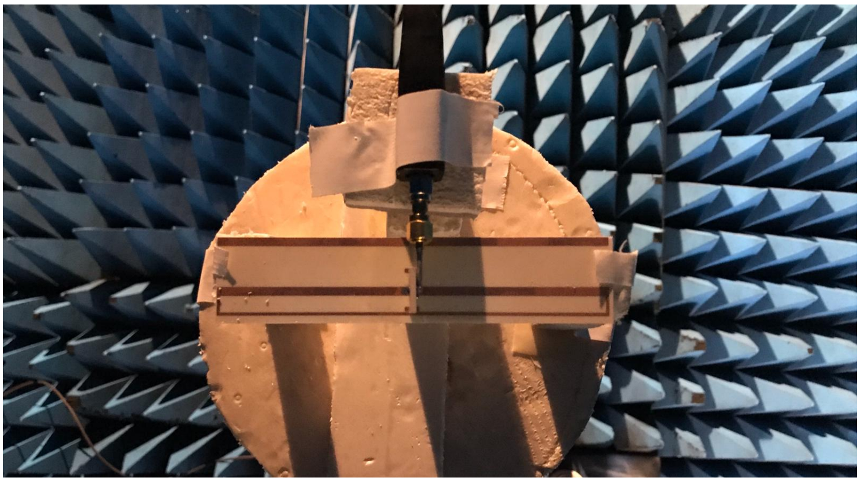

(A) Two-straight dipole array.

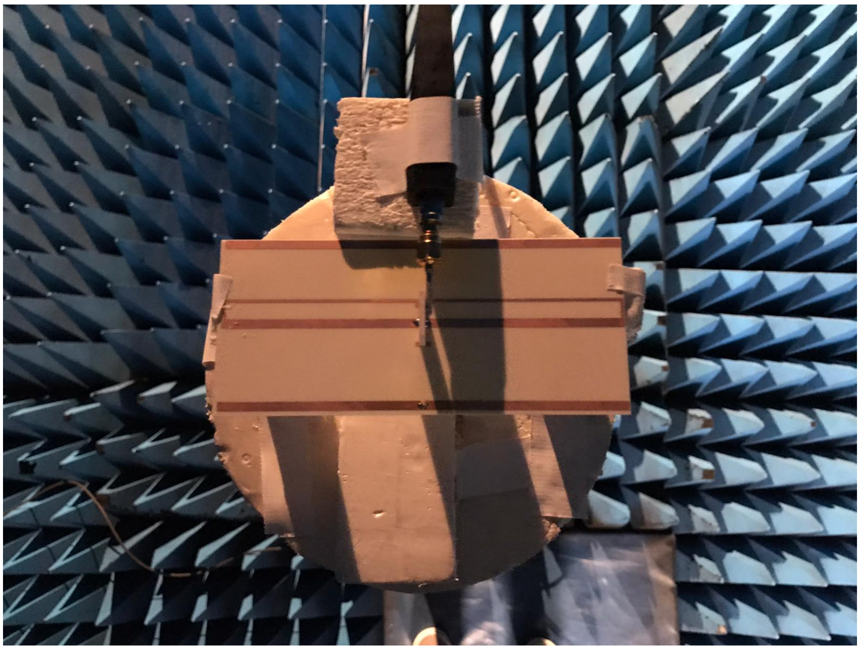

(B) Three-straight dipole array.

FIGURE 6.7: Measurement set-up.

These lower measured losses can thus be explained by either an underestimation of directivity in measurement or an overestimation of losses in simulation. The directivity derived from the measurements can be inaccurate as it was extracted from the gain diagrams on the $\phi = 0$ and $\phi = 90$ planes only and then making an interpolation for the rest of the diagram. This is demonstrated in Figure 6.11 as the measured gain is even higher than the directivity. The intrinsic gain is indeed up to 0.2 dBi over the directivity for frequencies between 820 and 850 MHz, proving an underestimation of the directivity in that case.

The simulated radiation losses can also have been miscalculated and overestimated as it can be seen from the input reflection coefficients in Figure 6.10 that the total efficiency was in general very low which can cause imprecision in radiation efficiency calculations. Moreover the radiation efficiency is also a parameter that varies according to frequency and the maximization was made for a single frequency point chosen at 850MHz whereas the maximum measured gain is sometime shifted in frequency.

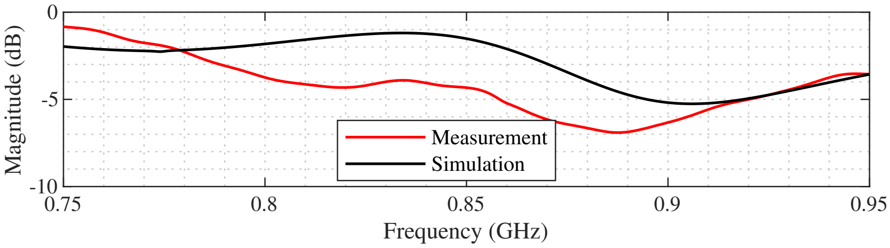

FIGURE 6.8: Input reflection coefficient of the simulated and measured two-bent-dipole array as a function of frequency. The optimization is made on gain.

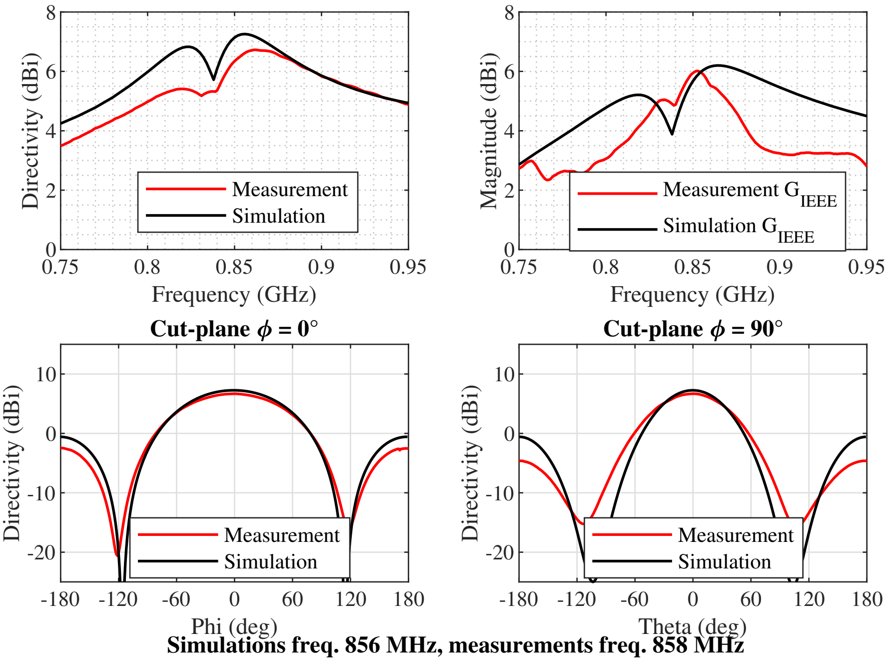

FIGURE 6.9: Directivity and intrinsic gain (G_{IEEE}) of the simulated and measured two-bent-dipole array as a function of frequency. The directivity diagram is also showed in the $\phi = 0$ and $\phi = 90$ planes, comparing measurements and simulations at the frequency that show the highest gain.

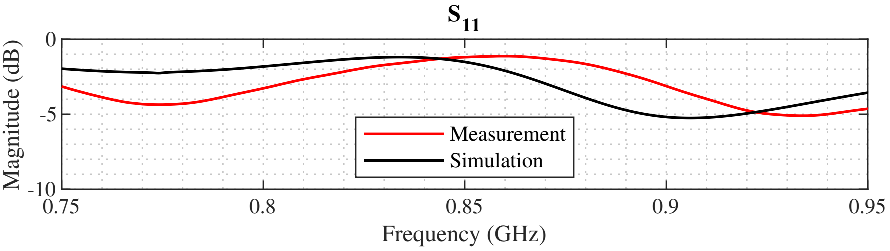

FIGURE 6.10: Input reflection coefficient of the simulated and measured two-dipole array with $d = 0.05$ inter-element spacing, as a function of frequency. The optimization is made on directivity.

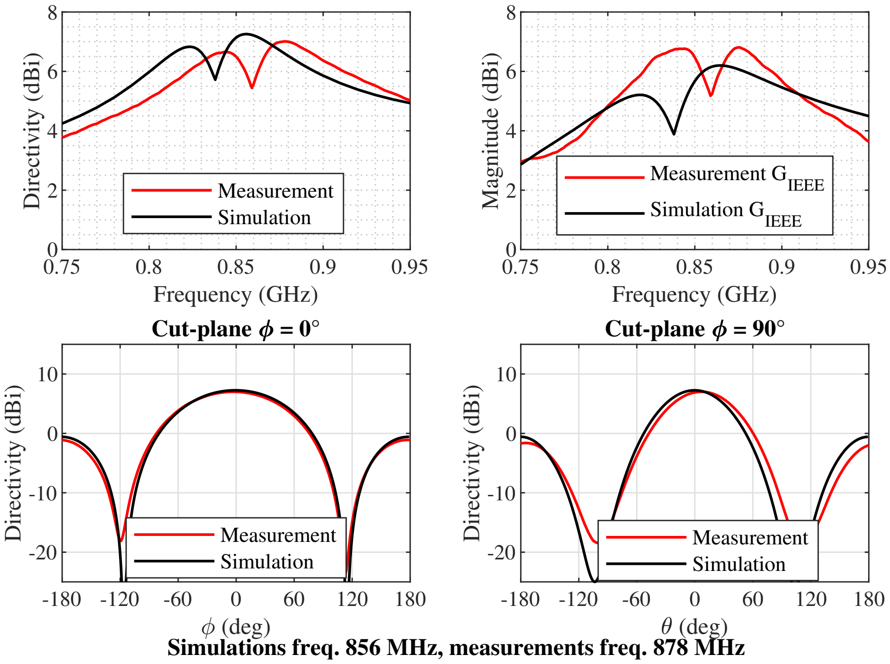

FIGURE 6.11: Directivity and intrinsic gain (G_{IEEE}) of the simulated and measured two-dipole array with $d = 0.05$ inter-element spacing, as a function of frequency. the directivity diagram is also showed in the $\phi = 0$ and $\phi = 90$ planes, comparing measurements and simulations at the frequency that show the highest directivity.

TABLE 6.1: Two-bent-dipole-arrays with $d = 0.1$ inter-element spacing main results from simulations and measurement, for gain maximization. The indicated frequency is the frequency where the maximum gain was found.

	Max. Theo.	Simu. 1	Simu. 2	Meas.
Frequency (MHz)	850	850	856	858
Directivity (dBi)	7.1	6.7	7.2	6.7
Gain (dBi)	6.7	6.3	6.0	6.0
$R_2 (\Omega)$		0	0	0
C_2 (pF)				
L_2 (nH)		1.6	1.5	1.5

TABLE 6.2: Two-dipole-arrays with $d = 0.05$ inter-element spacing main results from simulations and measurement, for gain maximization. The indicated frequency is the frequency where the maximum gain was found.

	Max. Theo.	Simu. 1	Simu. 2	Meas.
Frequency (MHz)	850	850	856	878
Directivity (dBi)	7.0	7.2	7.2	7.0
Gain (dBi)	5.9	5.8	6.0	6.8
$R_2(\Omega)$		0	0	0
C_2 (pF)				
L_2 (nH)		4.1	4.1	4.1

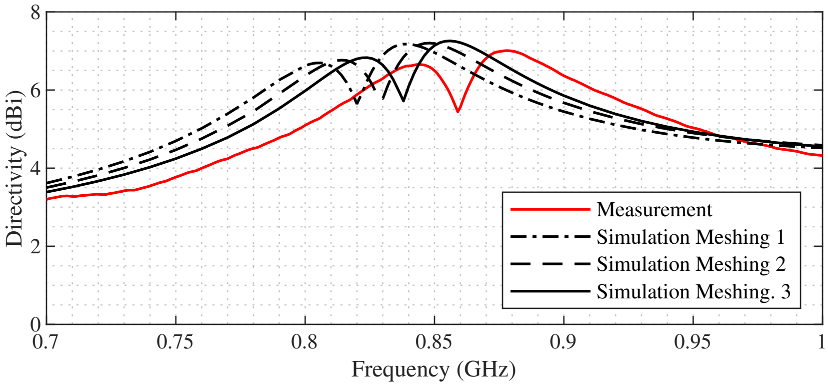

FIGURE 6.12: Simulated directivity as a function of frequency of the two-straight-dipole array through an adaptive frequency based solver, with increasing number of mesh.

Three-dipole arrays

The performance measured for the three-dipole arrays are shown in Tables 6.3, 6.4,6.5 and Figures 6.16, 6.14, 6.18.

Apart from some frequency shifts, the maximum directivities and gains that were measured are consistent with the simulations, in the gain maximization cases. The directivity derived from the measurements is however sensibly lower than the theoretical value and the one provided by the first simulation (8.9 dBi instead of 10.2 dBi). This is in accordance with the fact that the excitation currents used in these cases also provide a higher sensitivity factor, as it was seen in Chapter 3.

This also manifests in a wider -3dB bandwidth simulated and measured in directivity and gain when intrinsic gain is maximized.

In the gain maximization cases, the measured gain is also 0.8dB higher than the simulation results, which can be explained by the same reasons that are detailed in the two-dipole array cases analysis.

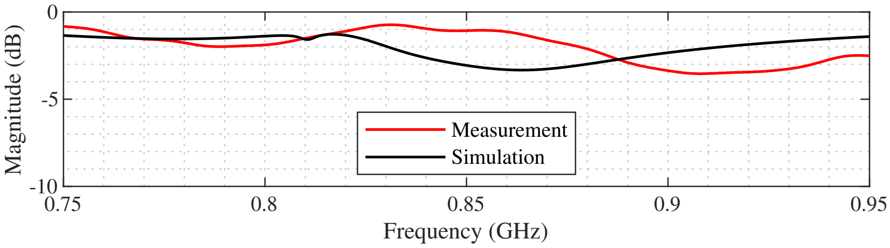

FIGURE 6.13: Input reflection coefficient of the simulated and measured three-bent-dipole array with $d = 0.12$ inter-element spacing, as a function of frequency. The optimization is made on gain.

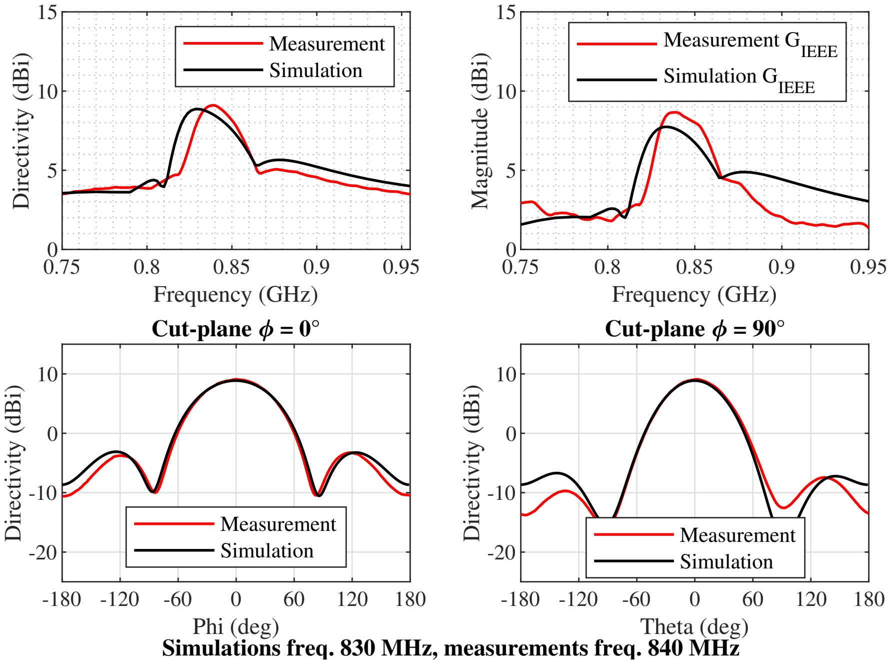

FIGURE 6.14: Directivity and intrinsic gain (G_{IEEE}) of the simulated and measured three-bent-dipole array with $d = 0.12$ inter-element spacing, as a function of frequency. The gain diagram is also showed in the $\phi = 0$ and $\phi = 90$ planes, comparing measurements and simulations at the frequency that show the highest gain.

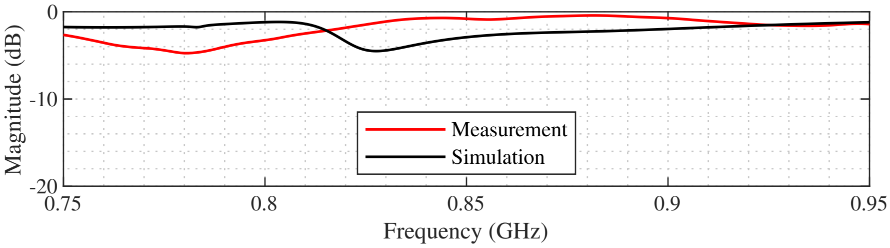

FIGURE 6.15: Input reflection coefficient of the simulated and measured three-dipole with $d = 0.08$ inter-element spacing, array as a function of frequency. The optimization is made on gain.

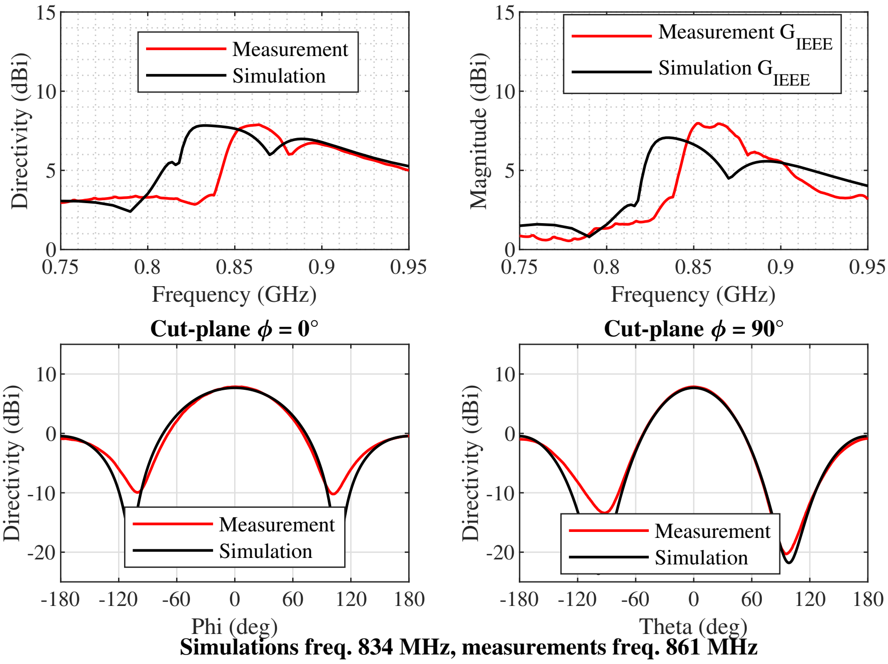

FIGURE 6.16: Directivity and intrinsic gain (G_{IEEE}) of the simulated and measured three-dipole with $d = 0.08$ inter-element spacing, array as a function of frequency. The gain diagram is also showed in the $\phi = 0$ and $\phi = 90$ planes, comparing measurements and simulations at the frequency that show the highest gain.

TABLE 6.3: Three-dipole-arrays with $d = 0.08$ inter-element spacing main results from simulations and measurement, for gain maximization. The indicated frequency is the frequency where the maximum gain was found.

	Max. Theo.	Simu. 1	Simu. 2	Meas.
Frequency (MHz)	850	850	834	861
Directivity (dBi)	7.8	7.8	7.8	7.8
Gain (dBi)	7.3	7.3	7.1	7.7
$R_2(\Omega)$		0	0	0
$R_3(\Omega)$		0	0	0
C_2 (pF)				
C_3 (pF)				
L_2 (nH)		0.4	0.3	0.3
L_3 (nH)		5.0	5.1	5.1

TABLE 6.4: Three-bent-dipole-arrays with $d = 0.12$ inter-element spacing main results from simulations and measurement, for gain maximization. The indicated frequency is the frequency where the maximum gain was found.

	Max. Theo.	Simu. 1	Simu. 2	Meas.
Frequency (MHz)	850	850	830	840
Directivity (dBi)	9.2	9.1	8.9	9.1
Gain (dBi)	8.2	7.5	7.7	8.6
$R_2(\Omega)$		0	0	0
$R_3(\Omega)$		0	0	0
C_2 (pF)		24	22	22
C_3 (pF)		33	33	33
L_2 (nH)				
L_3 (nH)				

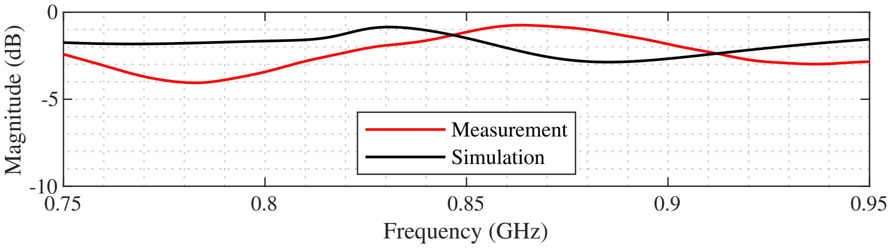

FIGURE 6.17: Input reflection coefficient of the simulated and measured three-dipole array with $d = 0.08$ inter-element spacing, as a function of frequency. The optimization is made on directivity.

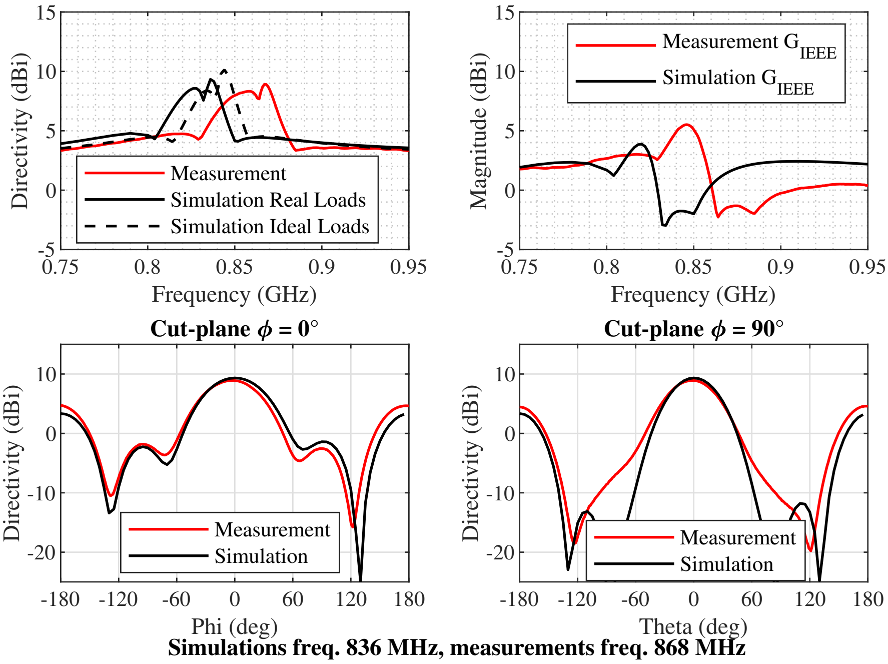

FIGURE 6.18: Directivity and intrinsic gain (G_{IEEE}) of the simulated and measured three-dipole array with $d = 0.08$ inter-element spacing, as a function of frequency. the directivity diagram is also showed in the $\phi = 0$ and $\phi = 90$ planes, comparing measurements and simulations at the frequency that show the highest directivity.

TABLE 6.5: Three-dipole-arrays with $d = 0.08$ inter-element spacing main results from simulations and measurement, for directivity maximization. The indicated frequency is the frequency where the maximum directivity was found.

	Max. Theo.	Simu. 1	Simu. 2	Meas.
Frequency (MHz)	850	850	836	868
Directivity (dBi)	10.3	10.2	9.3	8.9
Gain (dBi)	-0.7	-0.7	-2.3	-1.6
$R_2 (\Omega)$		3.3	3.3	3.3
$R_3 (\Omega)$		0.1	0	0
C_2 (pF)				
C_3 (pF)				
L_2 (nH)		4.7	4.7	4.7
L_3 (nH)		4.2	4.1	4.1

Four-dipole array

The performance measured for the four-dipole arrays are shown in Tables 6.6, 6.7 and Figures 6.5, 6.22. As seen with the three-dipole prototypes, measured performances are more consistent with simulation results in the gain maximization case.

The measured gain is also higher than simulation which can be attributed to the imprecision of intrinsic gain measurement as previously mentioned.

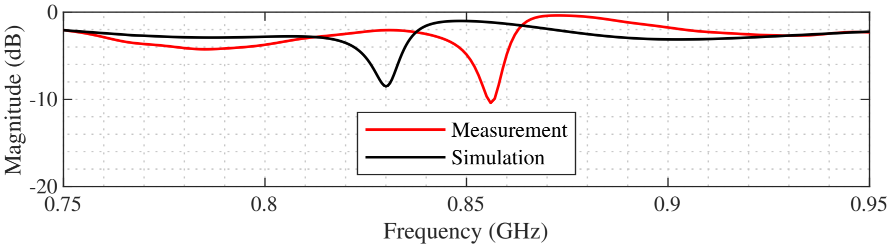

FIGURE 6.19: Input reflection coefficient of the simulated and measured four-straight-dipole array as a function of frequency. The optimization is made on gain.

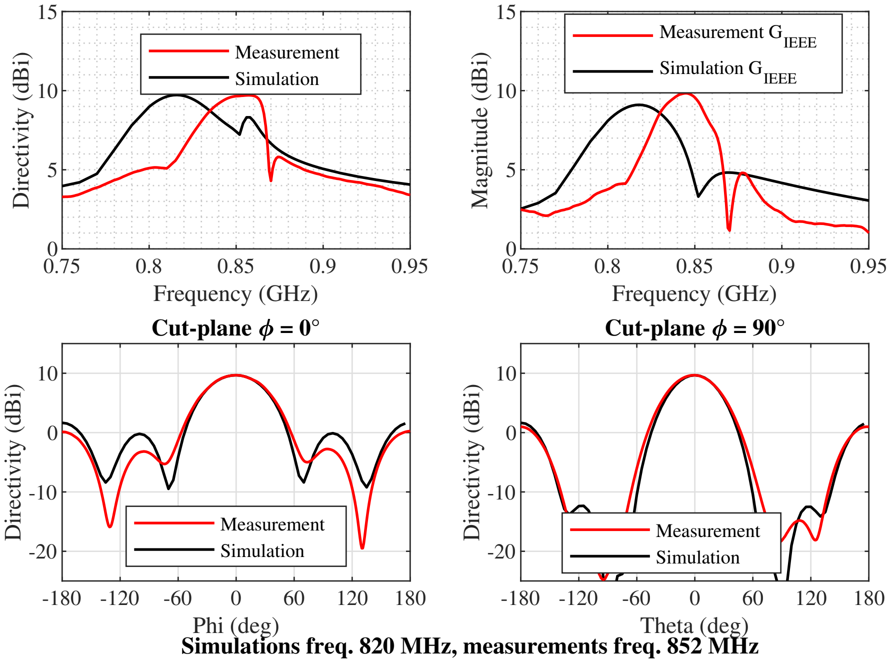

FIGURE 6.20: Directivity and intrinsic gain (G_{IEEE}) of the simulated and measured four-straight-dipole array as a function of frequency. the directivity diagram is also showed in the $\phi = 0$ and $\phi = 90$ planes, comparing measurements and simulations at the frequency that show the highest directivity.

TABLE 6.6: Four-dipole-arrays main results from simulations and measurement, for gain maximization. The indicated frequency is the frequency where the maximum gain was found.

	Max. Theo.	Simu. 1	Simu. 2	Meas.
Frequency (MHz)	850	850	820	852
Directivity (dBi)	10.1	9.7	9.7	9.6
Gain (dBi)	9.5	9.1	9.1	9.3
$R_2 (\Omega)$		0	0	0
$R_3 (\Omega)$		0	0	0
$R_4 (\Omega)$		0	0	0
C_2 (pF)				
C_3 (pF)				
C_4 (pF)				
L_2 (nH)		7.4	7.5	7.5
L_3 (nH)		34	33	33
L_4 (nH)		3.5	3.6	3.6

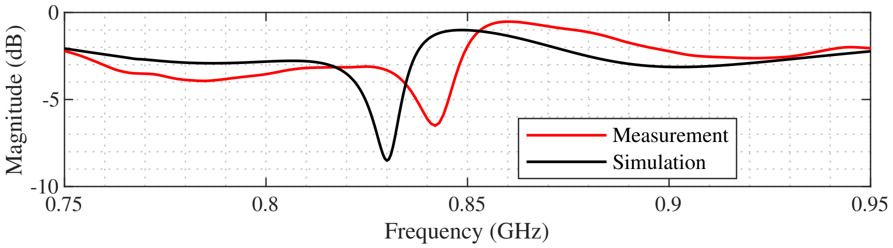

FIGURE 6.21: Input reflection coefficient of the simulated and measured four-straight-dipole array as a function of frequency. The optimization is made on directivity.

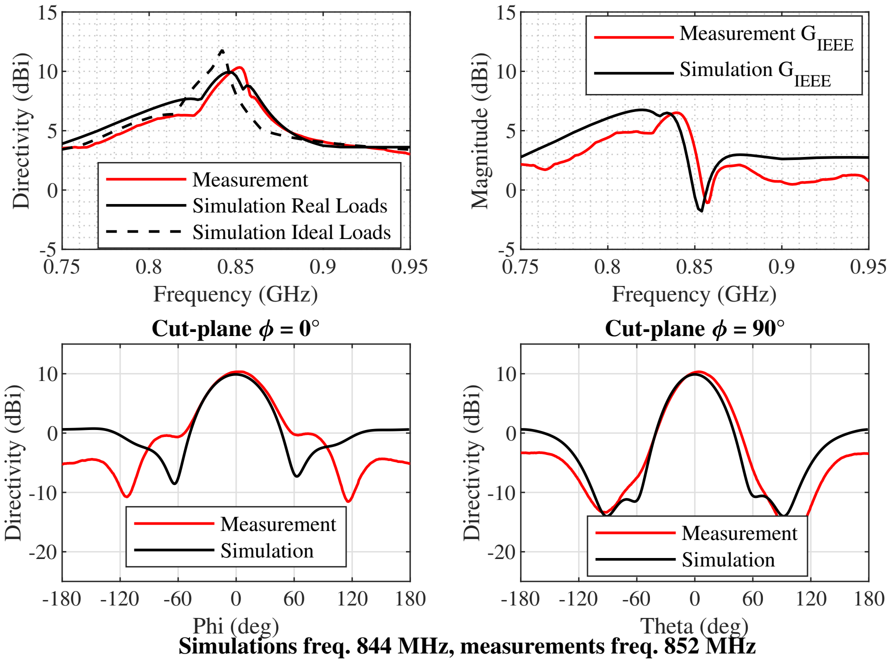

FIGURE 6.22: Directivity and intrinsic gain (G_{IEEE}) of the simulated and measured four-straight-dipole array as a function of frequency. the directivity diagram is also showed in the $\phi = 0$ and $\phi = 90$ planes, comparing measurements and simulations at the frequency that show the highest directivity.

TABLE 6.7: Four-dipole-arrays main results from simulations and measurement, for directivity maximization. The indicated frequency is the frequency where the maximum directivity was found.

	Max. Theo.	Simu. 1	Simu. 2	Meas.
Frequency (MHz)	850	850	844	852
Directivity (dBi)	12.4	12.2	9.9	10.3
Gain (dBi)	-1.7	-1.1	3.8	2.1
$R_2(\Omega)$		0.6	0.51	0.51
$R_3(\Omega)$		0.8	0.75	0.75
$R_4(\Omega)$		2.8	2.5	2.5
C_2 (pF)				
C_3 (pF)				
C_4 (pF)				
L_2 (nH)		6.8	6.8	6.8
L_3 (nH)		1.6	1.5	1.5
L_4 (nH)		6.3	6.2	6.2

6.1.5 Summary

To provide an overview of this experimental part, measured gains and directivities reached are here displayed as dots next to the theoretical curves of gain and directivity as a function of inter-element spacing, in Figures 6.23 and 6.24, for directivity and gain optimization, respectively.

These results are also summarized in Tables 6.9 and 6.8 comparing directivities and gains extracted from theory, full-wave simulation and measurement, for the different cases. It is to be noted that a directivity or gain found from simulation or measurement higher than the theoretical values can be explained by the fact that the theoretical performances were calculated considering infinitesimal dipoles whereas the straight-dipole-based prototypes use halfwave dipoles. This is most noticeable in the case of the two-straight-dipole array with inter-element spacing of $d = 0.05\lambda$ where the higher directivity of halfwave dipoles over infinitesimal ones can make the difference between the theoretical 5.9 dBi and the simulated 6.3 dBi of gain.

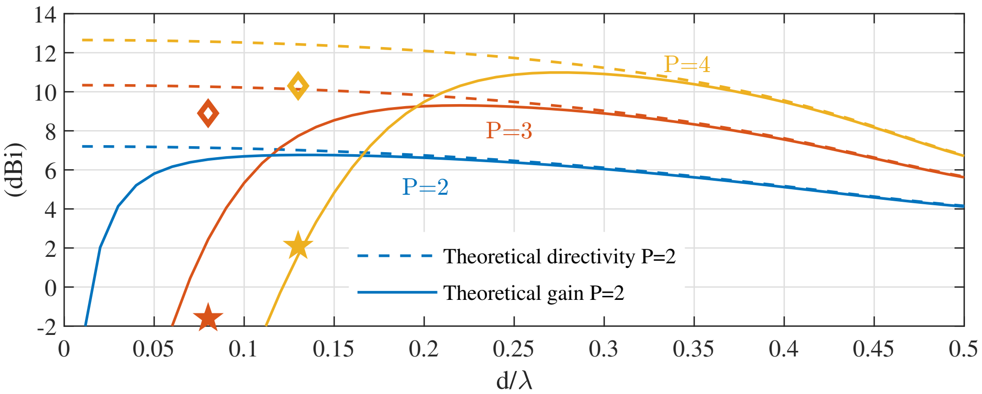

FIGURE 6.23: Measured gains (stars) and directivities (diamonds) compared to theoretical curves for directivity maximization, as a function of spacing d/λ from Chapter 3. The considered unitary radiation efficiencies for the theoretical curves is 99%.

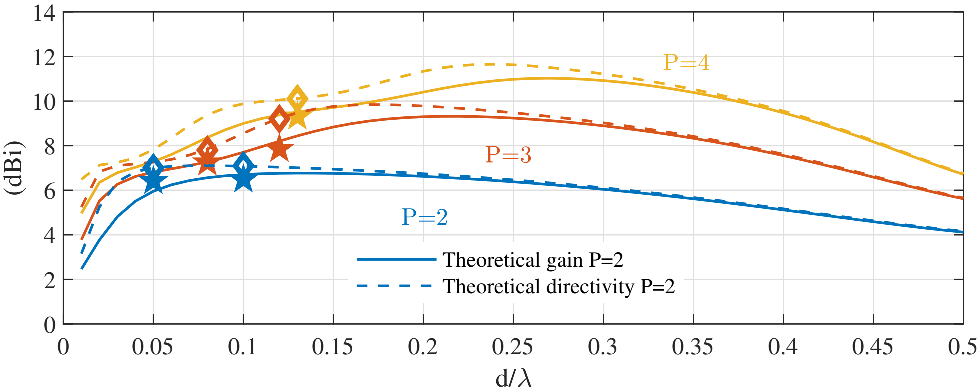

FIGURE 6.24: Measured gains (stars) and directivities (diamonds) compared to theoretical curves for gain maximization, as a function of spacing d/λ from Chapter 3. The considered unitary radiation efficiencies for the theoretical curves is 99%.

TABLE 6.8: Comparison of simulated and measurement directivities and gain to theoretical expected performances with infinitesimal dipoles, for directivity optimization.

	Theo. D	Simu. D	Meas. D	Theo. G	Simu. G	Meas. G
P=3 d=0.08	10.3	10.2	8.9	-0.7	-0.7	-1.6
P=4 d=0.13	12.4	12.2	10.3	-1.7	-1.1	2.1

TABLE 6.9: Comparison of simulated and measurement directivities and gain to theoretical expected performances with infinitesimal dipoles, for gain optimization.

	Theo. D	Simu. D	Meas. D	Theo. G	Simu. G	Meas. G
P=2 d=0.05	7.0	7.2	7.0	5.9	6.3	6.0
P=2 d=0.1	7.1	6.7	6.7	6.7	6.7	6.7
P=3 d=0.08	7.8	7.8	7.8	7.3	7.3	7.7
P=3 d=0.12	9.2	9.1	9.1	8.2	7.5	8.6
P=4 d=0.13	10.1	9.7	9.6	9.5	9.1	9.3

The next section then deals with the design of a two-Huygens-source array, through the use of full-wave simulation, discussing the possible interests over dipole-based arrays.

6.2 Huygens-source-based array

The purpose of this section is to propose a design method of Huygens-source-based arrays with parasitic elements, also providing an estimation of its possible performances. No practical design of such arrays seem to have been presented in the literature yet. Possible designs were presented in [31] for the choice of specific electric and magnetic dipole geometries but as that work showed a complexity judged too high for practical design, no feeding method for the array was proposed.

A practical parasitic-element-array of two Huygens sources is then detailed in this section. The validation is made through full-wave electromagnetic simulation. It is shown that it requires adjusted excitation coefficients for each of the four dipoles making up the array and then necessitates three parasitic loads. The conclusions of [31] are however largely reinforced as the performances expected at best seem lesser than those of electric-dipole-based arrays.

6.2.1 Single Huygens source design

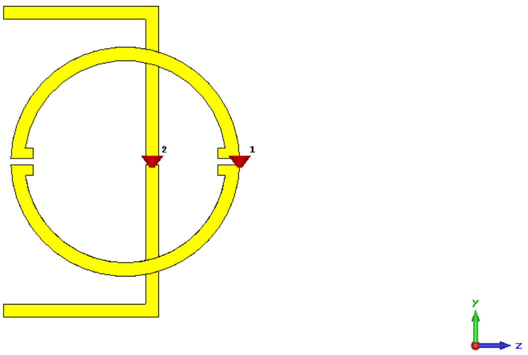

FIGURE 6.25: Huygens source model. The two dipoles are separated by a layer of dielectric substrate.

The Huygens source synthesis method is based on the SWE optimization procedure presented in Chapter 2. The proposed Huygens source design uses two ports, as in [31], and is then considered as a two element array. Hence, this algorithm can be applied to an array made of a magnetic and an electrical dipole to optimize the balance of the Transverse Electric (TE) and Transverse Magnetic (TM) spherical radiating modes.

The geometry of the dipoles is shown in Figure (6.25), it is a planar structure with two metallic layers separated by a dielectric substrate. The electric dipole is identical to the bent dipole of Figure 6.2. The magnetic dipole is made with a metallic loop similar to the one used in [20] to make a superdirective array. The loop then has two gaps where one is used to connect a component as parasitic load and the other act as a natural capacitor. The loop's radius is a half-wavelength long as is the electrical dipole which is bent at the half of its two arms. The driven element is the electrical dipole and it will excite the loop through coupling. Note that the size of the loop is not independently optimize to resonate at the working frequency of 850 MHz as it is made to be excited through near-field electromagnetic coupling. Figures (6.26a)

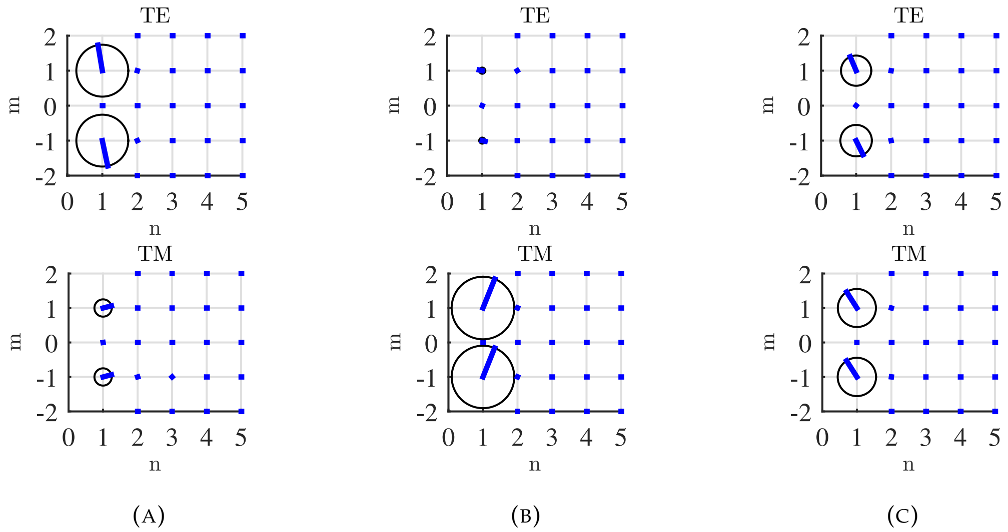

(A) (B) (C)

FIGURE 6.26: SWE of loop excited without parasitic load on electrical dipole (A), electric dipole excited without parasitic load on loop (B) and electric dipole excited with optimized load on loop (C).

and (6.26b) show the SWE of the antenna when only one of the two port is excited, with the other port loaded with 50Ω. These modes matches well the theoretical ones detailed in Chapter 1.

The SWE of the optimized antenna is displayed in Figure (6.26c). The simulated performances of the single source is summarized in Table 6.10 along with the optimal loads required.

The input reflection coefficients of the single source and the optimized two-Huygens-source array can be seen as a function of frequency in Figure 6.27. Only the radiation pattern was optimized in these designs and the matching to 50Ω of the single source would thus require an additionnal matching network. However, as it can be seen in Figure 6.27, the two-Huygens-source array showed a natural good impedance matching around the 850MHz frequency.

Its 3D-gain pattern is shown in Figure 6.29.

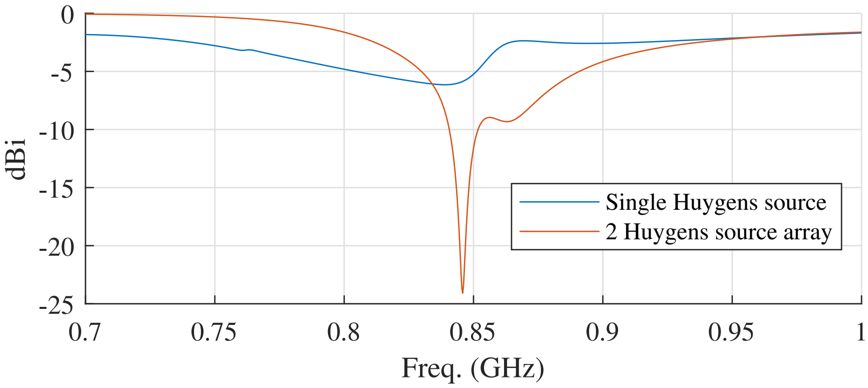

FIGURE 6.27: Input reflection coefficient of the simulated single Huygens source and two-Huygens-source array with parasitic loads, as a function of frequency.

TABLE 6.10: Single Huygens source and two-Huygens-source array main results from simulation for gain optimization.

	Huygens source	2 Huygens sources
Directivity (dBi)	4.29	8.24
Gain (dBi)	4.04	2.51
Realized Gain (dBi)	-6.24	1.98
$R_2(\Omega)$	-11.4	-5.3
$R_3(\Omega)$		2.3
$R_4(\Omega)$		-18.7
C_2 (pF)	0.9	1.0
C_3 (pF)		2.0
C_4 (pF)		5.3

(A)

(B)

FIGURE 6.28: SWE of the two-Huygens-source array, when optimizing only two ports (A), and when optimizing four ports (B).

6.2.2 Two-Huygens-Source array design

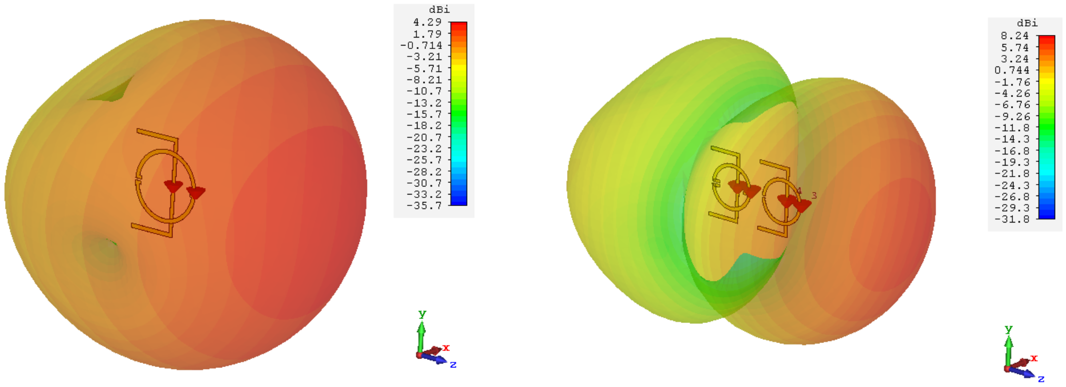

(A)

(B)

FIGURE 6.29: 3D-gain pattern of the single Huygens source (A) and of the two-Huygens-source array (B) for gain optimization (cf. Table 6.10).

As mentioned in Chapter 4, designs of Huygens sources have already been demonstrated. However these kind of Huygens sources are very difficult to put in an optimized array as the balance of the TE and TM modes obtained by the original design is disturbed when put in a closely spaced array. Indeed, when a Huygens source is a parasitic element of the array, it will be excited through coupling which will give a different radiation pattern than when directly excited through its port as in [57]. This is because of the independent couplings that occurs between the different dipoles. The design method presented here can overcome that difficulty with the use of a parasitic load for each dipole and the optimization of the radiated spherical waves. These optimal spherical radiating waves were described in a previous work [81], showing that the optimization is fairly simple in the case of ideal Huygens sources arrays and can be achieved with only one excitation per source. Here the radiation patterns used in the optimization come from the EM-simulation with MWS of CST and take account of the coupling effects which can only be corrected by using one port for each dipole so two ports per Huygens source. The difference between the two-port and four-port optimization is shown in Figure 6.28 through the SWE of the results. The two-port optimization provided a directivity of $6.0dBi$ while the four-port optimization gave $8.65dBi$ of directivity.

The gain calculated for the latter case is $7.76dBi$, so a radiation efficiency of 81%. The global dimensions of the antenna are $0.36\lambda_0 \times 0.25\lambda_0 \times 0.003\lambda_0$ which gives a ka of about 1.4 ($k = \frac{2\pi}{\lambda_0}$ and $a = 0.22\lambda_0$ is the radius of the minimum shere circumscribing the antenna), making it a supergain antenna according to Harrington's limit [3]. The performances reached with parasitic loading is given in Table 6.10 and the 3D-gain pattern is shown in Figure 6.29. These performances were obtained using the non-negative resistances indicated in Table 6.10 and neglecting the negative resistances. Also note that port 1 is fed so that R_1 and C_1 are unused.

The design method hereby described suggests the possibility to realize superdirective Huygens-source-based arrays that reach directivities close to the theoretical maximum. The design constraint brought by the required use of magnetic loops does however make the design far more complex than the simple electric-dipole-based arrays. Indeed, arrays of P Huygens sources require $2P - 1$ parasitic elements instead of $P - 1$. Moreover, the use of magnetic loops pulls down the radiation efficiency of the array which makes supergain much more difficult to achieve. The practical implementation of these designs was hence not attempted in this work, as the simulated performances did not seem interesting enough compared to dipole-based arrays, in this state. The design should thus be further improved, by exploring different dipole geometries, for example. However, at this point, the choice of priority of this work was then put on the optimization of dipole-based arrays, and gain optimization in particular.

6.3 Conclusions

In this chapter, it was shown that the use of the intrinsic gain maximization method for making supergain parasitic element compact arrays seems reliable as the expected gains could be reached. These optimizations also show a wider -3dB bandwidth in gain that the one obtained from the more classical directivity optimization. The use of a folded dipole was here made to maximize radiation efficiency on the fed dipole which was connected to the balun that also brings conduction and dielectric losses but the use of a single arm is however not sufficient in general to provide the array with a good impedance matching to 50 Ω. This design method can be further improved in future prototypes.

Then, the simulated design of a two-Huygens-source array prototype made in this chapter brought another argument to the impracticability of this kind of array. Indeed, the required loading of each of the three parasitic dipoles leads to a design that is complex and sensitive to variation for few performance improvement over classical electrical-dipole-based arrays. This design however merely represents a single attempt and can certainly be improved.

Conclusion

This thesis presents contributions to explore further the feasibility limits of superdirective and supergain arrays. This was done through the theoretical analysis of compact linear end-fire arrays of electrical dipole or Huygens sources, as well as experimental testing of electrical-dipole-based arrays.

The theoretical analysis based on SWE and array factor theory provided directivity and gain limits for these types of array. These limits can be used to anticipate the feasibility of compact end-fire superdirective and supergain arrays for given sizes and unitary element radiation efficiencies. For example, it can be seen that with efficiencies as good as 99% and dipole height of 0.3λ, the use of end-fire supergain arrays is advantageous over the 'normal' expected directivity (as defined by Harrington [3]) only using three or less elements. The use of superdirective end-fire antenna arrays is thus only relevant in some cases of limited antenna size and then is also limited in maximum gain and directivity, considering loss and precision limitations. The calculations that provide these boundaries for given loss resistances and excitation coefficients precision are given in Chapter 3. Also, the comparison to a general limit of maximum gain taken from SWE theory [41] was made, showing that end-fire arrays would reach that limit only in cases of extremely small total antenna size ($ka < 0.5$). Hence the combination of broadside and end-fire arrays is to be considered to approach the general maximum gain limit.

Another proposition made in the theoretical analysis part is the determination of the spherical wave distribution of dipole-based and Huygens-source-based superdirective and supergain arrays. This provides a physical interpretation to the directivity (and gain) limit of $P^2 + 2P$ for P-Huygens-source arrays and adds the upper limit for P-dipole arrays of $P^2 + P - 1/2$.

The second part of the thesis focuses on the practical considerations for the design of compact end-fire arrays. One conclusion in this regard, largely based on the study of the state of the art, is the fact that electrical dipoles are the best unitary element so far to use for supergain, as magnetic dipoles are less efficient for small sizes and Huygens-sources-based arrays require too much complexity to adjust the excitation of each dipole of the array. This last statement was further reinforced through the design and analysis of a two-Huygens-source arrays, using full-wave electromagnetic simulations, as presented in Chapter 6.

The study of practical implementation of compact end-fire arrays then focused on parasitic-element arrays, the analysis of which provided the following design rules regarding the electrical dipoles used. First, the small dipoles should be self-resonant for global input reactance and parasitic load reactance minimization. Then, the radiation resistance of the dipole should be increased using parasitic inductive element or preferably electric dipole folding for radiation efficiency enhancement. Also note that folding only the fed element avoids the increase of the required parasitic load impedance. Using folding or miniaturization techniques does however increase the quality factor of the radiating elements, which increases the sensitivity of the array optimization to feeding frequency. This can be a problem as this optimization relies on full-wave simulation with limited precision.

Moreover, the use of parasitic element arrays with impedance loads often requires resistive parts that can only be minimized through iterative optimization using several full-wave simulations. The same kind of optimization should also be done to improve the global input impedance of the array.

In any case, the use of the optimization technique that takes into account loss resistances or variance on excitation coefficients is useful to provide performances that are less sensitive to errors on the excitation coefficients. This was proven through the design and measurements of two- to four-dipole arrays that reach intrinsic gains higher that what was found in the state of the art for such close inter-element spacing, cf. Chapter 6.

The analysis on parasitic-element-array design presented in Chapter 5 is a first step that may be extended. The use of a model for resonant small dipoles would improve the analysis. This could, for example, allow for the study of the influence of individual variations in dipole length. The examination of the impact of unequal inter-element spacing can also be added. The purpose of the extension of this part would be to more easily optimize the design of parasitic-element arrays as regard to impedance load requirements and the minimization of resistances. The ultimate goal would be to directly optimize a Yagi-Uda-like array with small dipoles and performances equivalent to the one obtained with parasitic-element arrays that use various impedance loading. Moreover extending the analysis to the use of magnetic loops as array unitary elements could allow for a closer examination of Huygens-source-based arrays. The Huygens-source-based array design presented in Chapter 6 could not be optimized to avoid the use of parasitic resistive loads. The use of an analytical model could help to have a better understanding of how the design of this type of array may be improved.

The design of superdirective antenna is mostly useful for applications that require spatial selectivity with limited antenna size, such as RFID readers. In this context, some other research prospect can be considered, such as the optimization of arrays for given opening angles with maximum side lobe levels. Array antennas with excitation coefficients that use these constraints, such as in Schelkunoff's work [7] should then be considered. The use of beam-steering as proposed in [82] and [83] is also an interesting feature for spatial selectivity applications, as is the improvement of frequency bandwidth capabilities ([76], [74], [73], [75]).

Appendix A

End-fire Arrays SWE

A.1 Order of Legendre's polynomials in the wave functions

According to [84], the Legendre's polynomials can be expressed as:

$$P_n(x) = 2^n \sum_{k=0}^{n} x^k C_{k,n} C'_{\frac{n+k-1}{2},n} \tag{A.1}$$

where $C_{k,n}$ denotes the binomial coefficient (with k and n integers) and $C'_{q,k}$ is the binomial coefficient defined for any rational number q, by the multiplicative formula:

$$C'_{q,k} = \prod_{i=1}^{k} \frac{q+1-i}{i} \tag{A.2}$$

Then the associated Legendre's polynomial for order $m = 1$ can be written as:

$$P_n^1(x) = -\sqrt{1-x^2}\frac{d}{dx}P_n(x) \tag{A.3}$$

Then, taking $x = cos\theta$ it easily comes that

$$\frac{P_n^1(cos\theta)}{sin\theta} = \sum_{k=1}^{n} b'_{k,n} cos^{k-1}\theta \tag{A.4}$$

with

$$b'_{k,n} = -2^n k C_{k,n} C'_{\frac{n+k-1}{2},n} \tag{A.5}$$

and

$$\frac{dP_n^1(cos\theta)}{d\theta} = \sum_{k=1}^{n+1} b_{k,n} cos^{k-1}\theta \tag{A.6}$$

with

$$b_{k,n} = b'_{k-1,n}(k-1) - b'_{k+1,n}k \tag{A.7}$$

Then,

$$\frac{dP_n^1(cos\theta)}{d\theta} + \frac{P_n^1(cos\theta)}{sin\theta} = \sum_{k=0}^{n} a_{k,n} cos^k\theta \tag{A.8}$$

with

$$a_{k,n} = b'_{k,n} + b_{k,n}. \tag{A.9}$$

Moreover, one can also notice from [34] that:

$$\frac{d\overline{P}_n^1(cos\theta)}{d\theta}|_{\theta=\pi} = (-1)^n \frac{n(n+1)}{2} \tag{A.10}$$

and

$$\frac{\overline{P}_n^1(cos\theta)}{sin\theta}|_{\theta=\pi} = (-1)^{n+1} \frac{n(n+1)}{2} \tag{A.11}$$

So that

$$(\frac{d\overline{P}_n^1(cos\theta)}{d\theta} + \frac{\overline{P}_n^1(cos\theta)}{sin\theta})|_{\theta=\pi} = 0 \tag{A.12}$$

Thus, there exists $c_{k,n}$ coefficients such that

$$\frac{dP_n^1(cos\theta)}{d\theta} + \frac{P_n^1(cos\theta)}{sin\theta} = (1+cos\theta)\sum_{k=1}^{n} c_{k,n} cos^{k-1}\theta \tag{A.13}$$

These coefficients can be found using the remarkable identity:

$$x^k = r^k + (x-r)(x^{k-1} + rx^{k-2} + ... + (-1)^{k-1}) \tag{A.14}$$

with r real and $k > 0$. So, taking $r = -1$,

$$\begin{aligned}\sum_{k=0}^{n} a_{k,n}x^k = &\sum_{k=1}^{n} a_{k,n}(1+x)(x^{k-1} - x^{k-2} + ... + (-1)^{k-1}) \\ &+ \sum_{k=0}^{n}(-1)^k a_{k,n}\end{aligned} \tag{A.15}$$

Next it can be noticed that

$$\sum_{k=0}^{n}(-1)^k a_{k,n} = 0 \tag{A.16}$$

as the fact that the polynomial can be factorized by $1+x$ is already known from (A.12). Finally, the terms can be rearranged as in (A.13) with

$$c_{k,n} = \sum_{i=k}^{n}(-1)^{i-k} a_{i,n}. \tag{A.17}$$

A.2 Dipole arrays Spherical Wave Expansion

Let us examine separately the TE and TM modes of the far-field described by (3.10). First (1.19) gives for the TE part:

$$\vec{K}_{11n} - \vec{K}_{1,-1,n} = \sqrt{\frac{2}{n(n+1)}}(-j)^{n+1}2(\frac{\overline{P}_n^1(cos\theta)}{sin\theta}sin\phi\vec{e}_\theta + \frac{d\overline{P}_n^1(cos\theta)}{d\theta}cos\phi\vec{e}_\phi) \tag{A.18}$$

with (cf. Appendix A.1)

$$\frac{d\overline{P}_n^1(cos\theta)}{d\theta} = \sum_{k=1}^{n+1} b_{k,n} cos^{k-1}\theta \tag{A.19}$$

$$\frac{\overline{P}_n^1(cos\theta)}{sin\theta} = \sum_{k=1}^{n} b'_{k,n} cos^{k-1}\theta \tag{A.20}$$

thus,

$$\vec{K}_{11n} - \vec{K}_{1,-1,n} =$$

$$2\sqrt{\frac{2}{n(n+1)}}(-j)^{n+1}\sum_{k=1}^{n} cos^{k-1}\theta[b'_{k,n}sin\phi\vec{e}_\theta + b_{k,n}cos\phi\vec{e}_\phi] + b_{n+1,n}cos^n\theta cos\phi\vec{e}_\phi \tag{A.21}$$

Similarly, with (1.20), for the TM part:

$$\begin{aligned}\vec{K}_{21n} + \vec{K}_{2,-1,n} &= \sqrt{\frac{2}{n(n+1)}}(-j)^{n+1}2(\frac{d\overline{P}_n^1(cos\theta)}{d\theta}sin\phi\vec{e}_\theta + \frac{\overline{P}_n^1(cos\theta)}{sin\theta}cos\phi\vec{e}_\phi) \\ &= 2\sqrt{\frac{2}{n(n+1)}}(-j)^{n+1}\sum_{k=1}^{n} cos^{k-1}\theta[b_{k,n}sin\phi\vec{e}_\theta + b'_{k,n}cos\phi\vec{e}_\phi] + b'_{n+1,n}cos^n\theta sin\phi\vec{e}_\theta\end{aligned} \tag{A.22}$$

Thus, there exists complex coefficients T_n^{TM}, T_n^{TE} such that

$$\vec{f}_d(\theta,\phi)\sum_{k=1}^{P} B_k cos^{k-1} = \sum_{n=1}^{P-1} T_n^{TE}(\vec{K}_{11n} - \vec{K}_{1,-1,n}) + \sum_{n=1}^{P} T_n^{TM}(\vec{K}_{21n} + \vec{K}_{2,-1,n}) \tag{A.23}$$

Appendix B

Proof Complement to the Optimization Method of Directivity or Gain

Let us prove that the extended eigenvalue problem of equation (2.47) has only one non zero eigenvalue. This is an extended eigenvalue problem as matrix **H** is not always diagonal. This can be rearranges as a classical eigenvalue problem as

$$\begin{aligned} \mathbf{Ca} &= \lambda_0 \mathbf{Ha} \\ \Leftrightarrow \mathbf{H}^{\mathbf{-1}}\mathbf{Ca} &= \lambda_0 \mathbf{a} \end{aligned} \tag{B.1}$$

Note that **H** is known to be invertible as it is used to calculate the optimization solution in (2.48).

The number of non zero eigenvalues of (B.1) is then equal to the rank of matrix $\mathbf{H}^{\mathbf{-1}}\mathbf{C}$. Moreover, as **H** is invertible, the rank of the product $\mathbf{H}^{\mathbf{-1}}\mathbf{C}$ is equal to the rank of **C** [85]. The matrix **C** is defined by $(\mathbf{C}_{mp}) = e^{jk\vec{e}_r\cdot(\vec{r}_p-\vec{r}_m)}$. Taking that the first element of the array is at the center of the coordinate system and that the array is aligned along the $\vec{z}$ vector with an inter-element spacing of d , **C** can be written as

$$\mathbf{C} = \begin{bmatrix} 1 & e^{-jkd\vec{z}\cdot\vec{e}_r} & \cdots & e^{-j(P-1)kd\vec{z}\cdot\vec{e}_r} \\ e^{-jkd\vec{z}\cdot\vec{e}_r} & 1 & \cdots & e^{-j(P-2)kd\vec{z}\cdot\vec{e}_r} \\ \vdots & \vdots & \ddots & \vdots \\ e^{-j(P-1)kd\vec{z}\cdot\vec{e}_r} & e^{-j(P-2)kd\vec{z}\cdot\vec{e}_r} & \cdots & 1 \end{bmatrix}, \tag{B.2}$$

Hence, the $(m+1)$-th line of **C**, $\mathbf{C}_m$ can be calculated as a function of its first line $\mathbf{C}_1$ as $\mathbf{C}_{m+1} = e^{-jkd\vec{z}\cdot\vec{e}_r}\mathbf{C}_1$. Therefore, the rank of **C** is equal to 1 and (2.47) has only one non null eigenvalue.

Appendix C

Optimized Excitation Coefficients

The excitation coefficients calculated for optimizing two-, three- and four-dipole arrays are shown as a function of inter-element spacing (*d*) in this section. Figure C.1 shows the coefficients for directivity maximization whereas Figure C.2 shows the coefficients given for gain optimization, given single dipole with 97% radiation efficiencies. One can note that the amplitude of the coefficient seem to tend to infinity when the inter-element spacing tends to zero in the directivity optimization case. This is consistent with the expressions found for excitation coefficients in Chapter 3. In practice, this phenomenon is encountered in the high precision requirements as further detailed in Chapter 3. This also is consistent with the lower amplitude values of the coefficient provided for gain optimization.

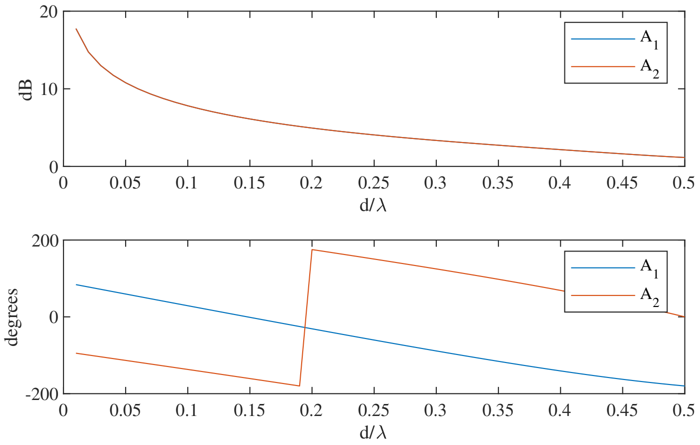

(A) Two-dipole array.

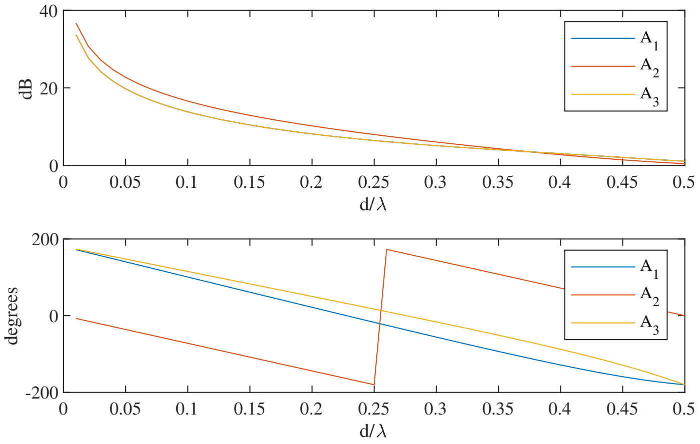

(B) Three-dipole array.

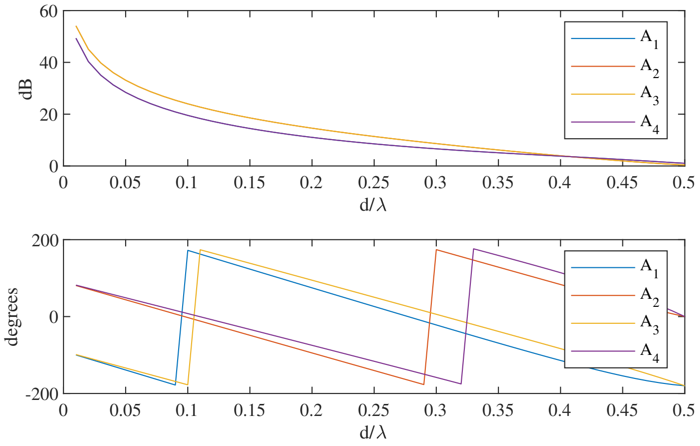

(C) Four-dipole array.

FIGURE C.1: Amplitude and phases of two-, three- and four-dipole based arrays optimized for maximum directivity.

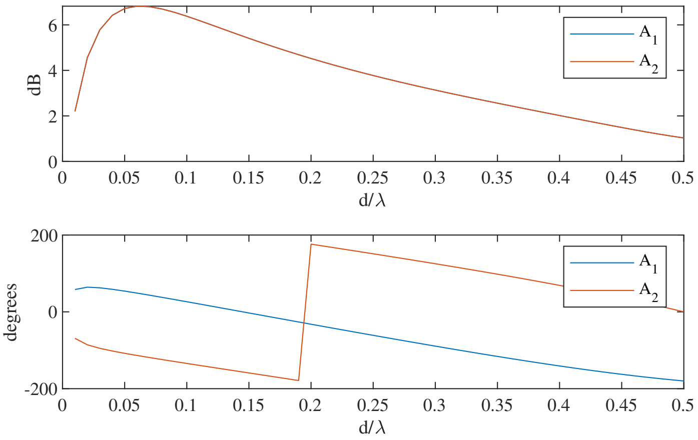

(A) Two-dipole array.

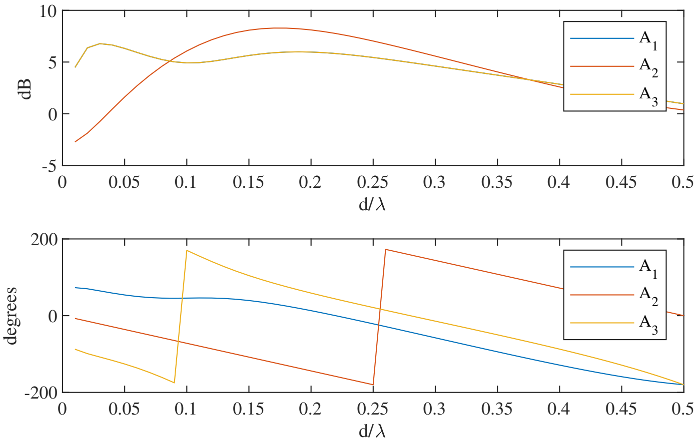

(B) Three-dipole array.

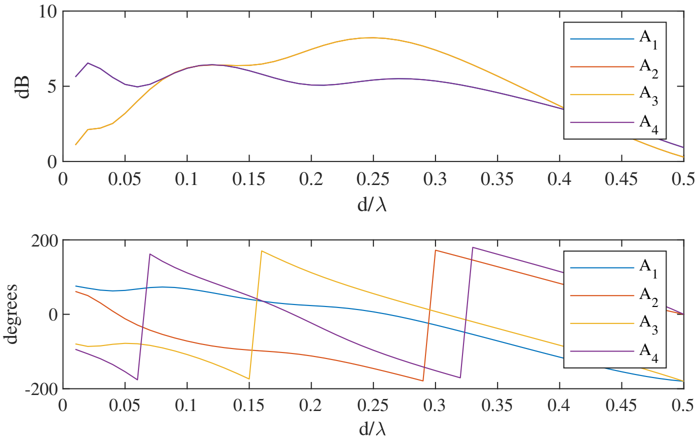

(C) Four-dipole array.

FIGURE C.2: Amplitude and phases of two-, three- and four-dipole based arrays optimized for maximum gain.

Appendix D

Balun Measured Characteristics.

The use of a balun is necessary with the superdirective antennas array in order to perfectly excite the pure TM modes of the source dipole. The balun used for the feeding of the antenna prototypes of Chapter 6 was developped by Lotfi Batel for the design of a compact super directive ESPAR antenna system [83]. The design is thus not detailed here as it is not yet made public. Its performances are however presented through the measurement of its scattering parameters in Figure D.2 and the relative phase of its outputs in Figure D.3. Note that the input port is port 3 in these Figures.

For frequencies between 800 and 900 MHz, Figure D.2 shows a matching under -7 dB of reflection coefficient and a balance in power between the two outputs that stay between -3.3 dB to -4 dB compared to input power. A relatively constant phase shift of 179 to 183 degrees is also observed between 0.5 and 1.5 GHz from Figure D.3. The set-up of the characterisation measurement used is displayed in Figure D.1.

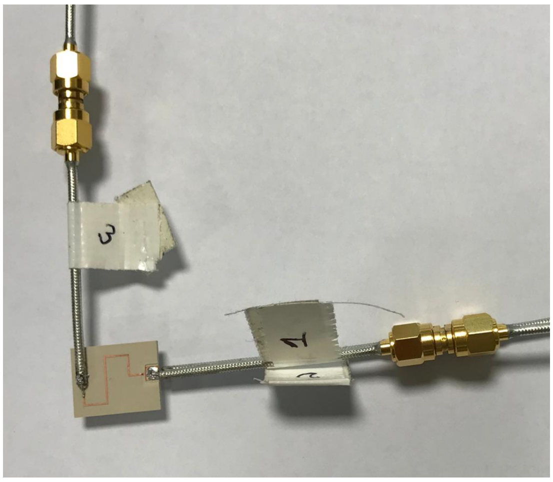

FIGURE D.1: Balun characterisation bench.

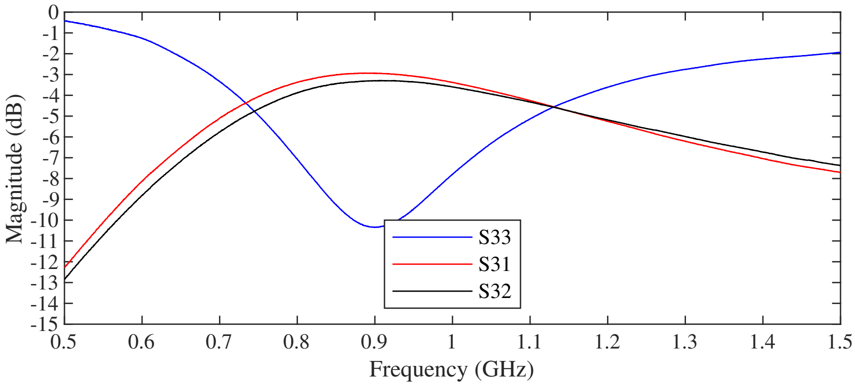

FIGURE D.2: Measured scattering parameters of the balun, over frequency.

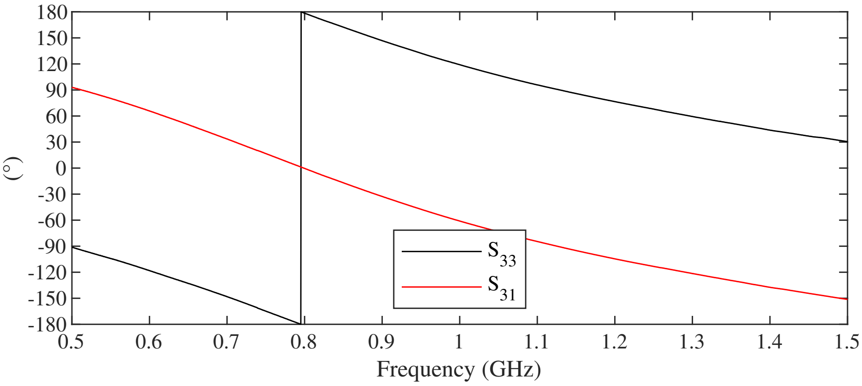

(A) Phase

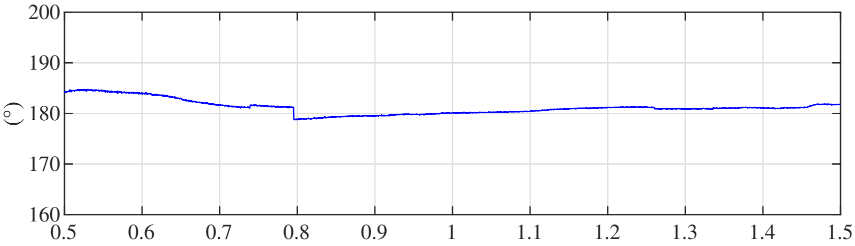

(B) Phase difference between the two outputs of the balun.

FIGURE D.3: Measured relative phase of the outputs of the balun.

Publications

International conferences

- A. Debard, A. Clemente, C. Delaveaud, C. Djoma, P. Potier and P. Pouliguen, “Analysis of superdirective Huygens source based end-fire arrays," 2017 11th European Conference on Antennas and Propagation (EUCAP), Paris, 2017, pp. 2983-2987, doi: 10.23919/EuCAP.2017.7928354.
- A. Debard, A. Clemente, C. Delaveaud, C. Djoma, P. Potier and P. Pouliguen, “Analytical evaluation of superdirective array sensitivity factor," 2017 IEEE International Symposium on Antennas and Propagation & USNC/URSI National Radio Science Meeting, San Diego, CA, 2017, pp. 361-362, doi: 10.1109/APUSNCURSINRSM.2017.8072223.
- A. Debard, A. Clemente, C. Delaveaud, C. Djoma, P. Potier, and P. Pouliguen, “Design and optimization of a two-element Huygens source based superdirective array”, (EuCAP), London, 2018, doi: 10.1049/cp.2018.0485.
- A. Debard, A. Clemente, C. Delaveaud, P. Potier and P. Pouliguen, “Limitations and Optimization of Supergain End-Fire Arrays," 2019 13th European Conference on Antennas and Propagation (EuCAP), Krakow, Poland, 2019, pp. 1-4.
- A. Debard, A. Clemente and C. Delaveaud,“Assessment and Accurate Evaluation of Antenna Superdirectivity Limits with Spherical Wave Expansion," 2019 International Conference on Electromagnetics in Advanced Applications (ICEAA), Granada, Spain, 2019, pp. 0654-0657, doi: 10.1109/ICEAA.2019.8879248.
- A. Debard, A. Clemente and C. Delaveaud, “Three-Element End-Fire Linear Arrays (Super) Directivity and Gain Optimization," 2020 14th European Conference on Antennas and Propagation (EuCAP), Copenhagen, Denmark, 2020, pp. 1-4, doi: 10.23919/EuCAP48036.2020.9135981.

National conference

- A. Debard, A. Clemente, C. Delaveaud, C. Djoma, P. Potier, et P. Pouliguen, “Analyse de réseaux d’antennes superdirectifs à base de dipôles et de sources de Huygens”, 20ème Journéés Nationales Micro-Ondes (JNM), Saint-Malo, 2017.

Bibliography

[1] R. C. Hansen, *Electrically Small Antennas - Electrically Small, Superdirective, and Superconducting Antennas - Wiley Online Library*. John Wiley & Sons, Inc, Jun. 12, 2006, ISBN: 978-0-471-78255-1. [Online]. Available: https://onlinelibrary.wiley.com/doi/10.1002/0470041048.ch1 (visited on 07/24/2019).

[2] H. A. Wheeler, “The radiansphere around a small antenna,” *Proceedings of the IRE*, vol. 47, no. 8, pp. 1325–1331, Aug. 1959, ISSN: 0096-8390. DOI: 10.1109/JRPROC.1959.287198.

[3] R. Harrington, “On the gain and beamwidth of directional antennas,” *IRE Transactions on Antennas and Propagation*, vol. 6, no. 3, pp. 219–225, Jul. 1958, ISSN: 0096-1973. DOI: 10.1109/TAP.1958.1144605.

[4] R. L. Fante, “Maximum possible gain for an arbitrary ideal antenna with specified quality factor,” *IEEE Transactions on Antennas and Propagation*, vol. 40, no. 12, pp. 1586–1588, Dec. 1992, ISSN: 0018-926X. DOI: 10.1109/8.204754.

[5] W. Geyi, “Physical limitations of antenna,” *IEEE Transactions on Antennas and Propagation*, vol. 51, no. 8, pp. 2116–2123, Aug. 2003, ISSN: 0018-926X. DOI: 10.1109/TAP.2003.814754.

[6] M. Uzsoki and L. Solymar, “Theory of superdirective linear arrays,” *Acta Physica Hungarica, vol. 6, no. 2*, pp. 185–205, 1956.

[7] S. A. Schelkunoff, “A mathematical theory of linear arrays,” *The Bell System Technical Journal*, vol. 22, no. 1, pp. 80–107, Jan. 1943, ISSN: 0005-8580. DOI: 10.1002/j.1538-7305.1943.tb01306.x.

[8] C. L. Dolph, “A current distribution for broadside arrays which optimizes the relationship between beam width and side-lobe level,” *Proceedings of the IRE*, vol. 34, no. 6, pp. 335–348, Jun. 1946, ISSN: 0096-8390. DOI: 10.1109/JRPROC.1946.225956.

[9] A. I. Uzkov, “An approach to the problem of optimum directive antennae design,” *Comptes Rendus (Doklady) de l'Académie des Sciences de l'URSS*, pp. 35–38, 1946.

[10] N. Yaru, “A note on super-gain antenna arrays,” *Proceedings of the IRE*, vol. 39, no. 9, pp. 1081–1085, Sep. 1951, ISSN: 0096-8390. DOI: 10.1109/JRPROC.1951.273753.

[11] A. Bloch, R. G. Medhurst, and S. D. Pool, "A new approach to the design of super-directive aerial arrays," *Journal of the Institution of Electrical Engineers*, vol. 1953, no. 10, pp. 324–326, Oct. 1953. DOI: `10.1049/jiee-2.1953.0204`.

[12] E. N. Gilbert and S. P. Morgan, "Optimum design of directive antenna arrays subject to random variations," *The Bell System Technical Journal*, vol. 34, no. 3, pp. 637–663, May 1955, ISSN: 0005-8580. DOI: `10.1002/j.1538-7305.1955.tb01488.x`.

[13] H. Bach and J. Hansen, "Uniformly spaced arrays," in *Antenna Theory, Part I*, R.E. Collin and F. J. Zucker, New York: McGraw-Hill, 1969.

[14] E. E. Altshuler, T. H. O'Donnell, A. D. Yaghjian, and S. R. Best, "A monopole superdirective array," *IEEE Transactions on Antennas and Propagation*, vol. 53, no. 8, pp. 2653–2661, Aug. 2005, ISSN: 0018-926X. DOI: `10.1109/TAP.2005.851810`.

[15] A. D. Yaghjian, T. H. O'Donnell, E. E. Altshuler, and S. R. Best, "Electrically small supergain end-fire arrays," *Radio Sci.*, vol. 43, no. 3, RS3002, Jun. 2008, ISSN: 1944-799X. DOI: `10.1029/2007RS003747`. [Online]. Available: `http://onlinelibrary.wiley.com/doi/10.1029/2007RS003747/abstract` (visited on 07/21/2016).

[16] T. H. O'Donnell and A. D. Yaghjian, "Electrically small superdirective arrays using parasitic elements," in *2006 IEEE Antennas and Propagation Society International Symposium*, Jul. 2006, pp. 3111–3114. DOI: `10.1109/APS.2006.1711268`.

[17] S. R. Best, E. E. Altshuler, A. D. Yaghjian, J. M. McGinthy, and T. H. O'Donnell, "An impedance-matched 2-element superdirective array," *IEEE Antennas and Wireless Propagation Letters*, vol. 7, pp. 302–305, 2008, ISSN: 1536-1225. DOI: `10.1109/LAWP.2008.921372`.

[18] S. Lim and H. Ling, "Design of electrically small, pattern reconfigurable yagi antenna," *Electronics Letters*, vol. 43, no. 24, pp. 1326–1327, Nov. 2007, ISSN: 0013-5194. DOI: `10.1049/el:2007239`.

[19] A. Noguchi and H. Arai, "3-element super-directive endfire array with decoupling network," in *2014 International Symposium on Antennas and Propagation (ISAP)*, Dec. 2014, pp. 455–456. DOI: `10.1109/ISANP.2014.7026723`.

[20] O. S. Kim, S. Pivnenko, and O. Breinbjerg, "Superdirective magnetic dipole array as a first-order probe for spherical near-field antenna measurements," *IEEE Transactions on Antennas and Propagation*, vol. 60, no. 10, pp. 4670–4676, Oct. 2012, ISSN: 0018-926X. DOI: `10.1109/TAP.2012.2207363`.

[21] A. Clemente, M. Pigeon, L. Rudant, and C. Delaveaud, "Super directive compact antenna design using spherical wave expansion," in *2014 IEEE Antennas and Propagation Society International Symposium (APSURSI)*, Jul. 2014, pp. 571–572. DOI: `10.1109/APS.2014.6904616`.

[22] A. Clemente, M. Pigeon, L. Rudant, and C. Delaveaud, "Design of a super directive four-element compact antenna array using spherical wave expansion," *IEEE Transactions on Antennas and Propagation*, pp. 4715–4721, 2015.

[23] M. Hammoud, A. Haskou, A. Sharaiha, and S. Collardey, "Small end-fire superdirective folded meandered monopole antenna array," *Microw. Opt. Technol. Lett.*, vol. 58, no. 9, pp. 2122–2124, Sep. 2016, ISSN: 1098-2760. DOI: `10.1002/mop.29995`. [Online]. Available: `http://onlinelibrary.wiley.com/doi/10.1002/mop.29995/abstract` (visited on 07/21/2016).

[24] A. Haskou, A. Sharaiha, and S. Collardey, "Theoretical and practical limits of superdirective antenna arrays," *Comptes Rendus Physique*, Energy and radiosciences, vol. 18, no. 2, pp. 118–124, Feb. 2017, ISSN: 1631-0705. DOI: `10.1016/j.crhy.2016.11.003`. [Online]. Available: `http://www.sciencedirect.com/science/article/pii/S1631070516301566` (visited on 08/09/2018).

[25] A. Haskou, A. Sharaiha, and S. Collardey, "Decoupling approach of superdirective antenna arrays," in *2017 11th European Conference on Antennas and Propagation (EUCAP)*, Mar. 2017, pp. 2519–2521. DOI: `10.23919/EuCAP.2017.7928788`.

[26] A. D. Yaghjian, "Increasing the supergain of electrically small antennas using metamaterials," 2010.

[27] R. W. Ziolkowski, "Using huygens multipole arrays to realize unidirectional needle-like radiation," *Physical Review X*, vol. 7, no. 3, p. 031 017, Jul. 26, 2017. DOI: `10.1103/PhysRevX.7.031017`. [Online]. Available: `https://link.aps.org/doi/10.1103/PhysRevX.7.031017` (visited on 03/11/2019).

[28] P. Jin and R. W. Ziolkowski, "Metamaterial-inspired, electrically small huygens sources," *IEEE Antennas and Wireless Propagation Letters*, vol. 9, pp. 501–505, 2010, ISSN: 1536-1225. DOI: `10.1109/LAWP.2010.2051311`.

[29] P. Alitalo, A. O. Karilainen, T. Niemi, C. R. Simovski, and S. A. Tretyakov, "Design and realisation of an electrically small huygens source for circular polarisation," *Antennas Propagation IET Microwaves*, vol. 5, no. 7, pp. 783–789, May 2011, ISSN: 1751-8725. DOI: `10.1049/iet-map.2010.0524`.

[30] L. Ge and K. M. Luk, "A magneto-electric dipole antenna with low-profile and simple structure," *IEEE Antennas and Wireless Propagation Letters*, vol. 12, pp. 140–142, 2013, ISSN: 1536-1225. DOI: `10.1109/LAWP.2013.2244054`.

[31] S. R. Best, "Progress in the design and realization of an electrically small huygens source," in *2010 International Workshop on Antenna Technology (iWAT)*, Mar. 2010, pp. 1–4. DOI: `10.1109/IWAT.2010.5464866`.

[32] J. A. Stratton, *Electromagnetic Theory*, McGraw-Hill. Mar. 1, 2007, 644 pp.

[33] F. Jensen, "Electromagnetic near-field-far-field correlations," Ph.D. dissertation, 1970.

[34] J. E. Hansen, *Spherical Near-Field Antenna Measurements*, Institution of Engineering and Technology. London, UK: J. E. Hansen, 2008.

[35] C. A. Balanis, *Antenna theory: analysis and design*, Third. Wiley Interscience, 2005.

[36] L. Chu, "Physical limitations of omni-directional antennas," *Journal of Applied Physics 19*, pp. 1163–1167, 1948.

[37] R. Collin and S. Rothschild, "Evaluation of antenna q," *IEEE Transactions on Antennas and Propagation*, vol. 12, no. 1, pp. 23–27, Jan. 1964, ISSN: 0018-926X. DOI: 10.1109/TAP.1964.1138151.

[38] R. Fante, "Quality factor of general ideal antennas," *IEEE Transactions on Antennas and Propagation*, vol. 17, no. 2, pp. 151–155, Mar. 1969, ISSN: 0018-926X. DOI: 10.1109/TAP.1969.1139411.

[39] M. Pigeon, A. Clemente, C. Delaveaud, and L. Rudant, "Analysis of harrington limit for electrically small antenna directivity," in *The 8th European Conference on Antennas and Propagation (EuCAP 2014)*, Apr. 2014, pp. 2921–2925. DOI: 10.1109/EuCAP.2014.6902438.

[40] A. D. Yaghjian and S. R. Best, "Impedance, bandwidth, and q of antennas," *IEEE Transactions on Antennas and Propagation*, vol. 53, no. 4, pp. 1298–1324, Apr. 2005, ISSN: 0018-926X. DOI: 10.1109/TAP.2005.844443.

[41] R. F. Harrington, *Effect of antenna size on gain, bandwidth, and efficiency*. National Bureau of Standards, 1960. [Online]. Available: http://archive.org/details/jresv64Dn1p1.

[42] A. D. Yaghjian, "Increasing the supergain of electrically small antennas using metamaterials," in *2009 3rd European Conference on Antennas and Propagation*, Mar. 2009, pp. 858–860.

[43] R. Harrington and J. Mautz, "Theory of characteristic modes for conducting bodies," *IEEE Transactions on Antennas and Propagation*, vol. 19, no. 5, pp. 622–628, Sep. 1971, ISSN: 0018-926X. DOI: 10.1109/TAP.1971.1139999.

[44] ——, "Computation of characteristic modes for conducting bodies," *IEEE Transactions on Antennas and Propagation*, vol. 19, no. 5, pp. 629–639, Sep. 1971, ISSN: 0018-926X. DOI: 10.1109/TAP.1971.1139990.

[45] B. K. Lau, D. Manteuffel, H. Arai, and S. V. Hum, "Guest editorial theory and applications of characteristic modes," *IEEE Transactions on Antennas and Propagation*, vol. 64, no. 7, pp. 2590–2594, Jul. 2016, ISSN: 0018-926X. DOI: 10.1109/TAP.2016.2579668.

[46] M. Capek, M. Gustafsson, and K. Schab, "Minimization of antenna quality factor," *IEEE Transactions on Antennas and Propagation*, vol. 65, no. 8, pp. 4115–4123, Aug. 2017, ISSN: 0018-926X. DOI: 10.1109/TAP.2017.2717478.

[47] M. Gustafsson, M. Capek, and K. Schab, "Trade-off between antenna efficiency and q-factor," *IEEE Transactions on Antennas and Propagation*, vol. 67, no. 4, pp. 2482–2493, Apr. 2019, ISSN: 0018-926X, 1558-2221. DOI: `10.1109/TAP.2019.2891448`. arXiv: `1802.01476`. [Online]. Available: `http://arxiv.org/abs/1802.01476` (visited on 08/09/2019).

[48] H. Jaafar, S. Collardey, D. Lemur, A. Haskou, and A. Sharaiha, "Characteristic modes optimisation approach to design a wideband electrically small antenna," in *2017 11th European Conference on Antennas and Propagation (EUCAP)*, Mar. 2017, pp. 2184–2186. DOI: `10.23919/EuCAP.2017.7928443`.

[49] H. Jaafar, S. Collardey, and A. Sharaiha, "Optimized manipulation of the network characteristic modes for wideband small antenna matching," *IEEE Transactions on Antennas and Propagation*, vol. 65, no. 11, pp. 5757–5767, Nov. 2017, ISSN: 0018-926X. DOI: `10.1109/TAP.2017.2754408`.

[50] ——, "Characteristic modes approach to design compact superdirective array with enhanced bandwidth," *IEEE Transactions on Antennas and Propagation*, vol. 66, no. 12, pp. 6986–6996, Dec. 2018, ISSN: 0018-926X. DOI: `10.1109/TAP.2018.2874691`.

[51] H. Jaafar, A. Sharaiha, and S. Collardey, "A broadside efficient superdirective compact array with internally loaded wideband unit elements," in *2018 International Workshop on Antenna Technology (iWAT)*, Mar. 2018, pp. 1–4. DOI: `10.1109/IWAT.2018.8379218`.

[52] S. Mikki, S. Clauzier, and Y. Antar, "A correlation theory of antenna directivity with applications to superdirective arrays," *IEEE Antennas and Wireless Propagation Letters*, vol. 18, no. 5, pp. 811–815, May 2019, ISSN: 1536-1225. DOI: `10.1109/LAWP.2019.2897047`.

[53] A. Arbabi and S. Safavi-Naeini, "Maximum gain of a lossy antenna," *IEEE Transactions on Antennas and Propagation*, vol. 60, no. 1, pp. 2–7, Jan. 2012, ISSN: 0018-926X. DOI: `10.1109/TAP.2011.2167934`.

[54] P. Hazdra, J. Kracek, and T. Lonsky, "On the end-fire (super) directivity of an array of two elementary dipoles," *arXiv:1804.05876 [physics]*, Apr. 16, 2018. arXiv: `1804.05876`. [Online]. Available: `http://arxiv.org/abs/1804.05876` (visited on 05/26/2019).

[55] R. Harrington, "On the gain and beamwidth of directional antennas," *IRE Transactions on Antennas and Propagation*, vol. 6, no. 3, pp. 219–225, Jul. 1958, ISSN: 0096-1973. DOI: `10.1109/TAP.1958.1144605`.

[56] M. Pigeon, C. Delaveaud, L. Rudant, and K. Belmkaddem, "Miniature directive antennas," *International Journal of Microwave and Wireless Technologies*, vol. 6, no. 1, pp. 45–50, Feb. 2014, ISSN: 1759-0787, 1759-0795. DOI: `10.1017/S1759078713001098`. [Online]. Available: `https://www.cambridge.org/core/`

journals/international-journal-of-microwave-and-wireless-technologies/article/miniature-directive-antennas/D522B157994B9835E16E6C8BA03DE0D4 (visited on 03/11/2020).

[57] R. W. Ziolkowski, P. Jin, and C. C. Lin, "Metamaterial-inspired engineering of antennas," *Proceedings of the IEEE*, vol. 99, no. 10, pp. 1720–1731, Oct. 2011, ISSN: 0018-9219. DOI: 10.1109/JPROC.2010.2091610.

[58] W. Lin and R. W. Ziolkowski, "Electrically small, low-profile, huygens circularly polarized antenna," *IEEE Transactions on Antennas and Propagation*, vol. 66, no. 2, pp. 636–643, Feb. 2018, ISSN: 0018-926X. DOI: 10.1109/TAP.2017.2784432.

[59] P. Alitalo, A. O. Karilainen, T. Niemi, C. R. Simovski, and S. A. Tretyakov, "A linearly polarized huygens source formed by two omega particles," in *Proceedings of the 5th European Conference on Antennas and Propagation (EUCAP)*, Apr. 2011, pp. 2302–2305.

[60] M. C. Tang, B. Zhou, and R. W. Ziolkowski, "Low-profile, electrically small, huygens source antenna with pattern-reconfigurability that covers the entire azimuthal plane," *IEEE Transactions on Antennas and Propagation*, vol. 65, no. 3, pp. 1063–1072, Mar. 2017, ISSN: 0018-926X. DOI: 10.1109/TAP.2016.2647712.

[61] H. H. Beverage, "Radio receiving system," pat. 1,381,089.

[62] H. G. Schantz and R. E. DePierre, "Directive, electrically-small UWB antenna system and method," U.S. Patent 20130027249 A1, Jan. 2013. [Online]. Available: http://www.google.com/patents/US20130027249.

[63] H. Yagi, "Beam transmission of ultra short waves," *Proceedings of the Institute of Radio Engineers*, vol. 16, no. 6, pp. 715–740, Jun. 1928, ISSN: 0731-5996. DOI: 10.1109/JRPROC.1928.221464.

[64] T. H. O'Donnell, A. D. Yaghjian, and E. E. Altshuler, "Frequency optimization of parasitic superdirective two element arrays," in *2007 IEEE Antennas and Propagation Society International Symposium*, Jun. 2007, pp. 3932–3935. DOI: 10.1109/APS.2007.4396400.

[65] S. Lim and H. Ling, "Design of thin, efficient, electrically small antenna using multiple foldings," *Electronics Letters*, vol. 42, no. 16, pp. 895–896, Aug. 2006, ISSN: 0013-5194. DOI: 10.1049/el:20061792.

[66] S. R. Best, "A novel element and feed configuration for a dipole very closely spaced to a PEC ground plane," in *IEEE Antennas and Propagation Society Symposium, 2004.*, vol. 3, Jun. 2004, 2907–2910 Vol.3. DOI: 10.1109/APS.2004.1331986.

[67] E. NEWMAN and M. SCHROTE, "A wide-band electrically small superdirective array," *Antennas and Propagation, IEEE Transactions on*, vol. 30, pp. 1172–1176, Dec. 1, 1982. DOI: 10.1109/TAP.1982.1142971.

[68] S. Lim, H. Choo, R. L. Rogers, and H. Ling, “Electrically small antenna for maximising transmission into HF ground waves,” *Electronics Letters*, vol. 40, no. 22, pp. 1388–1389, Oct. 2004, ISSN: 0013-5194. DOI: 10.1049/el:20045888.

[69] R. Li, G. Wei, and D. McNamara, “A method for matching parasitic unidirectional electrically small array,” *Progress In Electromagnetics Research Letters*, vol. 76, p. 6, 2018.

[70] S. R. Best, “A discussion on the quality factor of impedance matched electrically small wire antennas,” *IEEE Transactions on Antennas and Propagation*, vol. 53, no. 1, pp. 502–508, Jan. 2005, ISSN: 0018-926X. DOI: 10.1109/TAP.2004.837107.

[71] J. A. Dobbins and R. L. Rogers, “Folded conical helix antenna,” *IEEE Transactions on Antennas and Propagation*, vol. 49, no. 12, pp. 1777–1781, Dec. 2001, ISSN: 0018-926X. DOI: 10.1109/8.982460.

[72] S. R. Best, “The performance properties of electrically small resonant multiple-arm folded wire antennas,” *IEEE Antennas and Propagation Magazine*, vol. 47, no. 4, pp. 13–27, Aug. 2005, ISSN: 1045-9243. DOI: 10.1109/MAP.2005.1589871.

[73] R. W. Ziolkowski, N. Zhu, and M. Tang, “Non-foster enhancements of electrically small antennas,” in *2012 International Symposium on Antennas and Propagation (ISAP)*, Oct. 2012, pp. 22–25.

[74] L. Batel, L. Rudant, J. Pintos, A. Clemente, C. Delaveaud, and K. Mahdjoubi, “High directive compact antenna with non-foster elements,” in *2015 International Workshop on Antenna Technology (iWAT)*, Mar. 2015, pp. 381–384. DOI: 10.1109/IWAT.2015.7365294.

[75] L. Batel, J. Pintos, and L. Rudant, “Superdirective and broadband compact antenna array using non-foster elements,” in *2019 International Workshop on Antenna Technology (iWAT)*, Mar. 2019, pp. 17–20. DOI: 10.1109/IWAT.2019.8730643.

[76] O. S. Kim, “Extending the bandwidth of a superdirective first-order probe for spherical near-field antenna measurements,” in *2015 International Symposium on Antennas and Propagation (ISAP)*, Nov. 2015, pp. 1–3.

[77] P. P. Viezbicke, “Yagi antenna design,” p. 36,

[78] A. Haskou, A. Sharaiha, S. Collardey, M. Pigeon, and K. Mahdjoubi, “A design methodology for electrically small superdirective antenna arrays,” in *2014 Loughborough Antennas and Propagation Conference (LAPC)*, Nov. 2014, pp. 405–409. DOI: 10.1109/LAPC.2014.6996410.

[79] S. J. Orfanidis, “Coupled antennas,” in *Electromagnetic Waves and Antennas*, Sophocles J. Orfanidis, ECE Department Rutgers University, Piscataway, 2016. [Online]. Available: www.ece.rutgers.edu/~orfanidi/ewa.

[80] A. R. Clark and A. P. C. Fourie, "Mutual impedance and the folded dipole," in *1994 Second International Conference on Computation in Electromagnetics*, Apr. 1994, pp. 347–350. DOI: `10.1049/cp:19940088`.

[81] A. Debard, A. Clemente, C. Delaveaud, C. Djoma, P. Potier, and P. Pouliguen, "Analysis of superdirective huygens source based end-fire arrays," in *2017 11th European Conference on Antennas and Propagation (EUCAP)*, Mar. 2017, pp. 2983–2987. DOI: `10.23919/EuCAP.2017.7928354`.

[82] A. S. Kaddour, S. Bories, A. Bellion, and C. Delaveaud, "Low profile dual-polarized wideband antenna," in *2016 International Symposium on Antennas and Propagation (ISAP)*, Oct. 2016, pp. 86–87.

[83] L. Batel, A. Clemente, and C. Delaveaud, "Superdirective and compact electronically-beam-switchable antenna for smart communication objects," in *2019 13th European Conference on Antennas and Propagation (EuCAP)*, ISSN: null, Mar. 2019, pp. 1–4.

[84] M. Abramowitz and I. A. Stegun, *Handbook of mathematical functions*.

[85] M. Leonid, *An introduction to linear algebra*, Dover Publications. 1955, ISBN: 978-0-486-66434-7.